Spectroscopy of Sr_2 for Metrology, Quantum Chemistry, and Tests of Fundamental Physics

Brandon Iritani

Submitted in partial fulfillment of the
requirements for the degree of
Doctor of Philosophy
under the Executive Committee
of the Graduate School of Arts and Sciences

COLUMBIA UNIVERSITY

2026

Abstract

Spectroscopy of Sr_2 for Metrology, Quantum Chemistry, and Tests of Fundamental Physics

Brandon Iritani

The interaction between light and matter provides a window into the intricate structure of atoms and molecules. From the first observation of the Balmer series in hydrogen, to modern atomic clocks, spectroscopy has been at the forefront of atomic, molecular, and optical (AMO) physics. As the field of AMO progresses towards increasingly complex systems, a natural next step from atoms is diatomic molecules, which have a rich internal structure that makes them attractive for applications in quantum simulation, quantum information and precision measurement. Here, optical lattice clock technology is combined with molecular physics through precision spectroscopy of Sr_2 molecules. As a benchmark, the systematic uncertainty of a clock transition spanning the ground-state potential of $^{88}Sr_2$ is evaluated to 4.6×10^{-14}, and the absolute frequency of the transition is measured to ~ 5 Hz uncertainty. In pursuit of reduced systematic uncertainty, a novel method for evaluating the notoriously difficult blackbody radiation (BBR) shift is presented, by comparing a near-infrared (IR) polarizability measurement to *ab initio* theory. A promising direction for the molecular clock is an isotope shift measurement to constrain non-Newtonian Yukawa-type internuclear interactions. To this end, stable samples of $^{86}Sr_2$ are produced, and precision spectroscopy is performed on its long-range halo state. The binding energies of all 63 vibrational states in the ground-state potential of $^{86}Sr_2$ are measured, and a completely *ab initio* calculation of the ground-state potential is tested against these measurements. These results lay the groundwork for refining quantum chemistry methods, as

well as combining them with experimental techniques in the search for new physics.

Table of Contents

List of Figures

List of Tables

Acknowledgments

I would like to first thank my advisor, Tanya Zelevinsky. Her deep knowledge of the Sr_2 molecule is admirable and has been a vital resource for me. She creates an environment where lab members have the freedom to explore new ideas that genuinely interest them. I feel lucky to have had the opportunity to work in her lab and to research topics that endlessly interest and excite me.

By far the highlight of my PhD has been the people I have had the opportunity to work alongside. Kon Leung was a valuable mentor, and I shared many laughs and exciting moments in the lab with him. He is one of the most impressive physicists I have worked with, with a seemingly instant ability to solve any experimental issue. He combines technical skill with a deep understanding of the underlying physics.

Emily Tiberi was always a joy to work with. I value our friendship and the eagerness she brought to the lab. She is one of the nicest person I have ever met, as well as the most Canadian. Mateusz Borkowski brought extensive AMO knowledge to our lab, along with endless dad jokes. I greatly value his expertise and his ability to explain new concepts to me. I will never forget his love of boxes.

Debayan Mitra was one of the best managers of people I have known, and I learned a great deal from watching him. He brought a personable attitude alongside a vast knowledge and strong work ethic. Though I never worked with him directly, he was always willing to lend a helping hand. Qi Sun was a great friend throughout my PhD. I admire his endless curiosity for physics and his capacity for asking questions in talks. He is a wonderful person, despite his inferior basketball abilities. Jinyu Dai, like Qi, was a great friend to me. He may be the greatest Coldplay

karaoke singer alive, but what truly brought us together was our shared love of beer. From my point of view, Jinyu knows everything and has a bright future as a scientist.

During my third year, Perry Zhou temporarily joined our experiment before sadly leaving for Chicago to join the CENTREX experiment. Perry is a funny, easygoing person who was a pleasure to work with. I look back fondly on our time at DAMOP watching South Park in the hotel room.

The following year, I was joined by Wenwei Xu. I will miss her endless experimental questions, which inevitably ended with me questioning myself. She has a great sense of humor and an impressive love for the arts, and I admire her appreciation of European culture. I have to give a huge thank you to Jingjing Huang. Her technical expertise and experimental tenacity are unmatched, and she rescued me at a time when I was struggling immensely. Her example as a postdoc is one I hope to follow. Gisung Sim has been a pleasure to work with these last couple of years. He brings a logical and curious approach to the experiment, and his love for whiskey has rubbed off on me.

I have to give a big shout out to the people around Pupin who made this work possible. One of my first projects was to install a satellite antenna, and I have fond memories of climbing onto the roof with Bob McGinnis and Clara Wilson. Bob was always ready to lend a hand at any time. He is a talented baker, and I spent many hours in his office hearing war stories. Clara is an incredible machinist, always willing to make us new pieces at a moment's notice, and the physics department already misses her greatly. The office staff was invaluable in organizing purchases and lab finances, especially Tina Phounsavath, Jennifer Chiu, and Peggy Huang. Tina even joined us for drinks and karaoke. Being greeted by Mary every morning was a great start to the day.

I spent countless Sundays watching football with Dan, Jason, and John. Their company was vital to my success, and our annual December Giants game got me through each year. This year, Jason and I even got to celebrate a Seahawks Super Bowl win. Trying new restaurants with Jason and Han was a highlight of my time in New York. I also want to thank the whole community of people at JDI. I always looked forward to the morning workouts with Matt and Vanessa, where

we did more talking than lifting. Matt's pessimistic attitude inevitably brightened every day. The CU barbell club was a welcoming community, especially Jack, a gifted coach who managed to make me strong!

I feel very lucky to have such a tight bond with my family, which is undeniably what got me this far. My dad's excitement for scientific research was passed down to me and ignited my own passion. My mom, as anyone who knows her would agree, is the most selfless person I know. Their unconditional support motivates me to persevere through any setback. Tad's dedication to his passions and his one-of-a-kind don't-give-a-f*ck attitude are traits I aspire to. Rachel has become a brilliant scientist and, against all odds, a functioning adult. They are two of my closest friends in the world, and I feel blessed to have them as my siblings.

Lastly, I have to thank Nicole. I think we have made the most of our time in New York. As I look back on my years here, the highlights were the days we spent exploring the city together. She is, without question, my best friend in the world. One paragraph is not enough to express all she has done for me, her support made everything here possible. The best part of every day is coming home to see Nicole and Charlie. We have had many adventures exploring the world together, and I hope we have many more.

Dedication

This thesis is dedicated to my family and my fiancée, Nicole.

Chapter 1: Introduction and background

1.1 Atomic clocks

"Never measure anything but frequency!" was the advice of Arthur Schawlow, a co-inventor of the laser. Clocks rely on continuous monitoring of a periodic event. Early frequency standards were based on the Earth's orbit or rotation [1]. For shorter time scales, clocks were based on mechanical resonators [2, 3]. Frequency is the most precisely measurable quantity in nature, and the most precise frequency references are atomic clocks. The first "atomic" clock was actually based on a radiofrequency (RF) transition in ammonia, a molecule, with a precision of $\sim 10^{-7}$ [4]. Since then, the field has grown dramatically, with current atomic clock precision surpassing that by over 10 orders of magnitude [5].

1.1.1 Background

Atomic clocks are based on precision spectroscopy of electronic states, initially, driving transitions between hyperfine levels in microwave frequency range, and more recently, probing optical transitions between atomic orbitals. Atoms are ideal clock candidates because, to the best of our knowledge, all atoms of a single species are identical, and they exhibit well-defined quantum transitions at precisely measurable frequencies. The same concept extends to molecules, where the additional relative motion of the nuclei, vibrations and rotations, provides further spectroscopic structure to probe. The key advance that made atomic clocks possible was the molecular beam magnetic resonance method developed by I.I. Rabi at Columbia, which is considered the first radiofrequency spectroscopy technique [6]. Norman Ramsey's separated oscillatory fields method enabled narrower measured linewidths and is still used in most modern atomic clocks [7]. For decades microwave clocks were the dominant form of atomic clock [8], until the development of

optical lattice clocks. The development that dramatically reshaped the landscape of atomic clocks was the invention of the optical frequency comb, which transfers stability in the radiofrequency range into the optical domain [9–18]. In optical lattice clocks, neutral atoms are trapped in an optical lattice operated at a 'magic' wavelength, where the differential lightshift between clock states vanishes, eliminating the leading-order lattice Stark shift and inhomogeneous broadening [19–25]. Optical lattice clocks have quantized motional states, and operate in the resolved-sideband, Lamb-Dicke regime, where the Lamb-Dicke parameter ($\eta = kx_0/\sqrt{2}$) compares the spatial extent of the ground motional state to the wavelength of the probe laser [5]. This suppresses motional shifts and Doppler broadening.

The shot-noise-limited fractional frequency instability is given by:

$$\sigma_y(\tau) \sim \frac{1}{Q\sqrt{N\tau}} \tag{1.1}$$

where τ is averaging time, N is atom number, and $Q = f_{clock}/\delta f$. This guides the choice of good clock candidates. We want large transition frequencies, and narrow transition linewidths.

1.1.2 Importance

Atomic clocks have many crucial applications. They currently provide the time standard for international atomic time (TAI). This is based on a network of predominantly cesium microwave clocks [26]. Atomic clocks have crucial applications in navigation, including the global navigation satellite systems (GNSS) [27–30], and they underpin infrastructure such as financial markets and power grids. They are precise enough to resolve the gravitational redshift across a millimeter-scale sample [31]. This gravitational sensitivity enables applications such as centimeter-scale geodesy, gravimetry, and gravity gradiometry [32]. Atomic clocks are also promising platforms for fundamental physics searches, including gravitational wave and dark matter detection [33–39]. Initially motivated by the desire to reduce density-dependent shifts, optical clocks are now used to study many-body physics, as their transition frequencies can be extremely sensitive to interparticle interactions [40–50]. Additionally, the standard quantum limit sets a noise floor that scales as $\frac{1}{\sqrt{N}}$.

Spin-squeezing techniques are being developed to push atomic clocks below the standard quantum limit [51–53]. They are also well-suited to measuring the time variation of fundamental constants, such as the fine-structure constant [39, 54–59]. There are also superradiant lasers based on emission from optical clock transitions [60–64]. Experimental efforts are also underway to develop clocks based on higher transition frequencies, such as the thorium nuclear transition [65–71].

1.2 Why use molecules?

Molecules, with their rich internal structure, offer distinctive advantages for precision measurement and quantum simulation. Molecules can be produced by two general approaches: direct laser cooling, often combined with a cryogenic buffer-gas beam source [72–80], or assembly from laser-cooled atomic samples. Atoms can be associated into molecules via magnetic Feshbach association [81–83], photoassociation [84–89], or trap merging and manipulation [90–98]. In addition to electronic structure, diatomic molecules have quantized rotational and vibrational levels, which enable precise characterization of the internuclear interaction. Additionally, molecules can have strong electric dipole moments [99–101], which provide opportunities for studying interparticle interactions [102–106]. Bose-Einstein condensation of dipolar molecules has been observed [107]. Polar diatomic molecules have an advantage over atoms for electric dipole moment searches: they can host a strong effective internal electric field when one of the constituent atoms is heavy and has strong s-p orbital hybridization [108]. Polar diatomic molecules have numerous applications in quantum simulation [109, 110] and quantum computation [111–114]. Polyatomic molecules possess even more intricate energy level structure, including additional bending and stretching vibrational modes, making them strong candidates for quantum chemistry and computation [115–118]. One notable advantage is the presence of near-degenerate states of opposite parity called parity doublets, which enhance sensitivity to dark matter searches [119] and symmetry-violation searches [120–124].

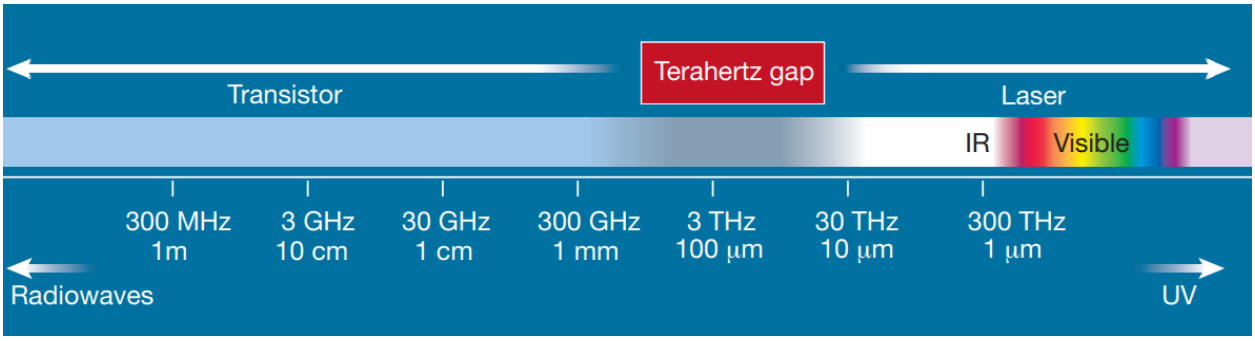

Figure 1.1: Optical atomic clocks operate at transition frequencies in the visible range (> 400 THz), while microwave atomic clocks operate in the microwave range (< 300 GHz). Vibrational molecular clock frequencies bridge this gap in the 1 – 30 THz range [126].

1.3 Sr_2

Our molecular clock operates by measuring molecular vibrational frequencies rather than electronic orbital frequencies. While the ticking mechanism for atomic clocks depends on the electromagnetic interaction between the nucleus and the electrons, the ticking rate for the molecular clock depends on the interaction between the two nuclei in the molecule. This provides opportunities to probe new physics and new frequency regimes. Firstly, typical vibrational transition frequencies occur in the so-called terahertz (THz) frequency gap between microwave and optical atomic clocks, where few frequency standards exist [Fig.1.1]. THz radiation is used to optimize materials for solar cells, used for airport security scanners, and in astronomy and communications applications [125]. It is also promising for biological and medical imaging, due to predicted resonances in biomolecules occurring in this range and the low tissue damage by such low energy photons.

Precise measurements of vibrational energies can also help inform and refine current understanding of interatomic quantum chemistry. An ongoing fruitful collaboration with the group of Robert Moszynski in the Quantum Chemistry Laboratory at the University of Warsaw has produced a greatly improved understanding of the structure of Sr_2. This includes extensive characterization of polarizability [127], transition strengths [128], photofragmentation [129–131], and characterization of molecular potential calculations. This collaboration relies on the marriage of Sr_2 clock

spectroscopy and state-of-the-art *ab initio* calculations. Sr_2 is a particularly attractive candidate for these tests, owing to its narrow spectroscopic lines and the lack of hyperfine structure in its bosonic isotopes. Insensitivity to external magnetic fields is a major advantage for clock evaluation, as it largely eliminates the Zeeman shift systematic that plagues Sr atomic clocks. Additionally, Sr_2 does not couple strongly to blackbody radiation (BBR), which reduces both the BBR shift as a clock systematic and the BBR-induced scattering that would otherwise limit the clock-state lifetime. In fact, we estimate BBR-limited lifetimes of $> 10^5$ years [132].

While we can compare to theoretical calculations to confirm our understanding of interatomic interactions, we can also constrain hypothetical new interactions. Reconciling general relativity with the Standard Model of particle physics remains an open problem in fundamental physics. Gravity is the only fundamental force without a proven quantum theory, and its relative weakness to other forces remains unexplained. Additional gravity-related phenomena, such as dark matter and dark energy, also remain poorly understood. To address these problems, various theories predict deviations from the Newtonian inverse square law, or introduce a new Yukawa-type fifth force [133–139]. They are parametrized in the following form:

$$V_5(R) = -\alpha \frac{G m_1 m_2}{R} e^{-R/\lambda}, \tag{1.2}$$

where α is the strength of the hypothetical force relative to Newtonian gravity, and λ is the characteristic length scale of the force. The best constraints at large distance are from astronomical observations [138, 140, 141]; torsion balances and microcantilevers are sensitive at micrometer distances [142–145]. The best constraints at nano- and picometer distances come from neutron scattering experiments [137, 146–148].

We hope to compare quantum chemistry calculations with molecular spectroscopy to constrain these forces. Similar approaches have been carried out with other molecules [149–151]. If we can characterize all known internuclear interactions, we can compare to experimental measurements. Any discrepancies between the two values could indicate the presence of new forces, or a missing component in the theoretical calculation. While it is difficult to calculate the full molecular ground-

state potential to experimental Hz-level accuracy with *ab initio* methods, we plan to simplify the calculation by measuring isotope shifts. Measuring the isotope shift of vibrational levels lets us compare experiment to *ab initio* calculations while reducing the theoretical load. Only the isotope-dependent terms of the Hamiltonian, the mass-dependent and nuclear-size-dependent terms, must be computed. Given our demonstrated clock precision of 5 Hz, we can project constraints on a hypothetical mass-dependent Yukawa force for a molecular isotope shift measurement between $^{88}Sr_2$ and $^{86}Sr_2$ (Fig.1.2).

$^{86}Sr_2$ garners particular interest due to the existence of its weakly bound long-range halo state. Its unusually large spatial extent makes it an intriguing candidate for exploring long-range QED effects such as the interatomic Casimir-Polder interaction.

1.4 Outline

1.4.1 Background

I highlight the aspects of level structure of atomic Sr that make it a favorable candidate for laser cooling methods as well as molecule production via photoassociation. I also describe the intricate molecular structure of Sr_2, which we explore through comparison to quantum chemistry calculations and exploit to make a better molecular clock.

1.4.2 Clock evaluation and BBR shift

I report on our metrological work with $^{88}Sr_2$, where we measure a $\approx$32 THz vibrational transition to $< 4.6 \times 10^{-14}$ systematic uncertainty. I also explore a new method for evaluating the blackbody radiation shift systematic by comparing ac polarizabilities at infrared wavelengths to *ab initio* calculations. With this method we evaluate the BBR shift for our clock transitions at the 10^{-16} level.

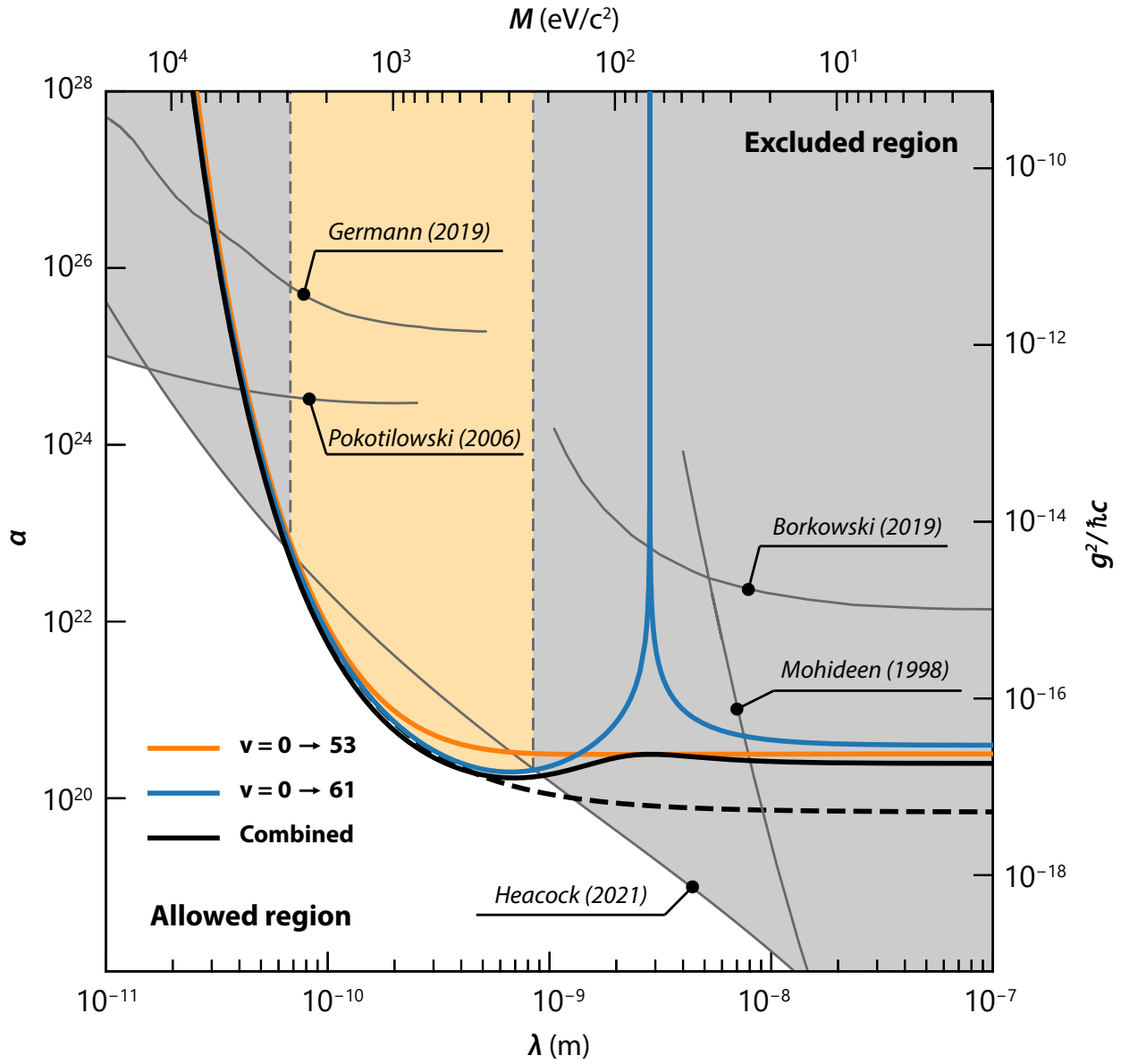

Figure 1.2: Projected constraints (95% CI) on α from an isotopic shift measurement of the $v = 0 \rightarrow 61$ (blue) and $v = 0 \rightarrow 53$ (orange) transitions in $^{88}Sr_2$ and $^{86}Sr_2$, as a function of λ. The combined constraint is shown in black. Previous limits (gray) are set by neutron scattering [148, 152] and Casimir force measurements [153]. Other molecule-based methods (Yb_2 [151] and HD^+ [150]) are also shown. For completeness, we also show the constraints in terms of particle mass M and squared coupling strength g^2. Even for current molecular clock accuracy [154], our method projects an order-of-magnitude improvement over leading laboratory constraints [148] for Yukawa forces due to new particles in the keV range. The dashed line represents an analytical approximation to the $^{86}Sr_2$-$^{88}Sr_2$ constraint.

1.4.3 Weakly bound $^{86}Sr_2$ molecules

I describe our procedure for interleaved loading of $^{86}Sr_2$ and $^{88}Sr_2$ atomic magneto-optical traps for a molecular isotope shift measurement. I also report on the investigation of photoassociation pathways with Autler-Townes spectroscopy of atomic samples. After producing $^{86}Sr_2$ molecules, we perform precise spectroscopy of the weakly bound states to explore the long-range portion of the molecular potential.

1.4.4 Evaluation of Sr_2 *ab initio* calculations

I report on the progress of *ab initio* quantum chemistry calculations, and their comparison to experimental results. I describe the procedure for the direct comparison of the analytic fit to experimental results. I explore the long-range behavior of the $^{86}Sr_2$ potential in order to investigate Casimir-Polder retardation effects.

Chapter 2: Sr_2 structure and sample preparation

Our molecule production method relies on laser cooling Sr atoms, trapping them in a 1D optical lattice, and then exploiting favorable wavefunction overlap to produce weakly bound molecules in the electronic ground-state via one-photon photoassociation. In contrast to directly laser cooling molecules, it is more straightforward to laser cool atoms to high phase-space densities. The level structure of alkaline-earth atoms makes them optimal for laser cooling to low temperatures without any additional sub-Doppler cooling methods. Bosonic Sr_2 in its ground electronic state has zero total angular momentum in $J = 0$ states, and therefore no magnetic moment. This makes it insensitive to external fields, reducing systematic shifts of clock transitions. It also possesses an excited-state structure that is advantageous for producing molecules via one-photon photoassociation, for creating magic wavelengths with adequate detuning from excited states, and for providing an intermediate state for the Raman clock transition.

2.1 Properties

2.1.1 Atomic structure

Strontium possesses two ideal cooling transitions that we exploit to create ultracold samples (Fig. 2.1). The requirement for a good laser cooling transition is that it cycles photons efficiently, meaning it decays predominantly from the excited state to the ground state with minimal loss to other states. The first transition that we use is the 461 nm $^1S_0 \leftrightarrow {}^1P_1$ singlet transition, which has a linewidth of $2\pi \times 32$ MHz. After heating a solid strontium sample in an oven to generate a hot atomic beam, we use this singlet transition for the Zeeman slowing. In this process, the Zeeman shift of the transition is tuned by a spatially varying magnetic field profile to match the spatially varying Doppler shift of the atoms coming out of the oven. Our experiment uses a unique perma-

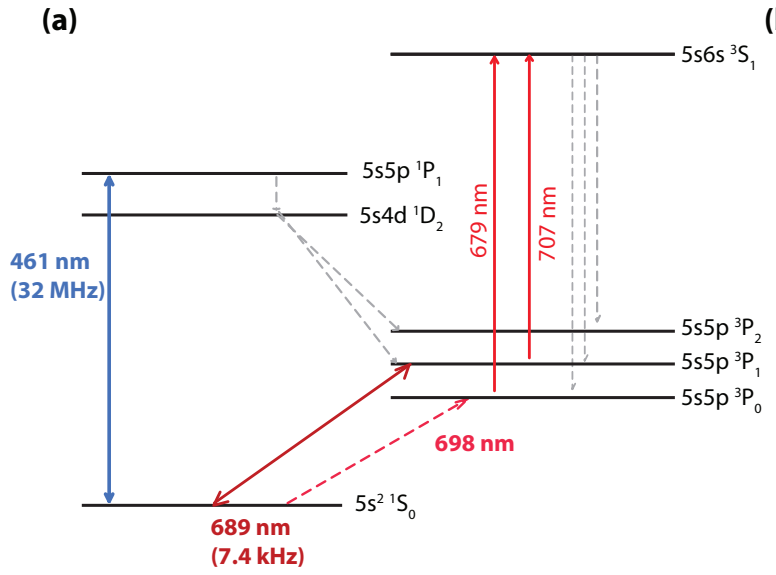

(b)

Isotope	Natural abundance	Nuclear spin
^{84}Sr	0.0056	0
^{86}Sr	0.0986	0
^{87}Sr	0.0700	**9/2**
^{88}Sr	0.8258	0

Figure 2.1: (a) Atomic level structure with relevant cooling and repump transitions. The 461 nm transition is for the first-stage MOT, 689 nm is for the second-stage MOT, and 679 nm and 707 nm are the repump lasers. The atomic clock transition at 698 nm is included for reference. (b) Relative abundance and nuclear spin of the stable isotopes of strontium.

nent magnet Zeeman slower configuration, where an array of magnets are attached to servo motors, and the horizontal position of which was optimized, resulting in a counter-intuitive magnetic field profile [155]. We use the same transition for the magneto-optical trap (MOT), which combines a quadrupole magnetic field profile produced by anti-Helmholtz coils with counter-propagating beams in three dimensions to trap and Doppler-cool the atoms simultaneously. During cycling on the singlet transition, there is loss to the ^{3}P states. $^3P_0$ is the state used for the Sr atomic clock transition, and both $^3P_0$ and $^3P_2$ are long-lived. As such, population accumulates in these states, and must be re-pumped out in order to re-enter the cycling transition. We do so by exciting the population in the 5s5p ^{3}P states to the 5s6s $^3S_1$ state. Any accumulated population in the $^3P_1$ state decays back down to the $^1S_0$ state on the millisecond timescale. The first MOT stage cools the atoms down to $\sim 800\mu K$.

The next MOT stage is on the $2\pi\times$7.4 kHz $^1S_0 \leftrightarrow {}^3P_1$ electric-dipole forbidden intercombination transition, which is weakly allowed due to spin-orbit coupling [86]. In order to efficiently transfer from the first stage MOT, we use frequency modulation to initially broaden the trapped velocity

classes [156]. We then sweep the broadened width, center frequency, and laser intensity down to a narrow-line MOT over 100 ms, and continue cooling in this configuration for $\sim$ 40 ms. This second-stage MOT cools the atoms down to $\sim 2\,\mu K$. The intercombination-line MOT that alkaline-earth species possess allows us to reach ultracold temperatures in $<$ 500 ms, whereas reaching the same temperature with alkali atoms requires evaporative cooling, which can take $\sim$30 s. This reduction in cycle time is especially crucial for atomic clocks where repetition rate directly affects precision [Eq. 1.1]. After this second MOT stage, the atoms are loaded into the optical lattice.

2.1.2 Molecular structure

The full Hamiltonian for a diatomic molecule is as follows:

$$\hat{H} = \hat{H}_e + \hat{H}_v + \hat{H}_R, \tag{2.1}$$

where $\hat{H}_e$, $\hat{H}_v$, and $\hat{H}_R$ correspond to the electronic, vibrational, and rotational contributions, respectively. The rotational Hamiltonian can be written in terms of the total rotational angular momentum $\hat{R}$ as:

$$\hat{H}_R = B\hat{R}^2 = B(\hat{J} - \hat{L} - \hat{S})^2, \tag{2.2}$$

where B is the rotational constant $B = \frac{\hbar^2}{2\mu R^2}$, where R is the bond length, and μ is the reduced mass. $\hat{L}$ and $\hat{S}$ are the total electronic orbital and spin angular momenta, and $\hat{J}$ is the total rotational plus electronic angular momentum. For diatomic molecules with strong spin-orbit coupling, total electronic and spin angular momenta of the molecule are not conserved. Therefore, the projections Λ and Σ of orbital and spin angular momentum onto the internuclear axis are not good quantum numbers. Instead, the sum $\Omega = \Lambda + \Sigma$ is a good quantum number.

The relevant potentials in Sr_2 are represented by multiple different Hund's cases that arise due to different angular momentum coupling. For Hund's case (c), it is assumed that the spin-orbit coupling between $\hat{L}$ and $\hat{S}$ is stronger than the coupling of either to the internuclear axis. In this

case, there is a total electronic angular momentum operator $\hat{J}_a$ that is only weakly coupled to the molecular rotation. The notation of Hund's case (c) is as follows:

$$|\Omega|^{+/-}_{g/u}, \tag{2.3}$$

where $+/-$ is the reflection symmetry of the electronic wavefunction about a plane containing the internuclear axis (only for $\Omega = 0$ states). "g/u" stands for gerade/ungerade meaning even/odd. This refers to the symmetry of the inversion of the electronic wavefunction through the center point of symmetry.

For Hund's case (a), the orbital angular momentum $\hat{L}$ is strongly coupled to the internuclear axis, while the electronic spin $\hat{S}$ is strongly coupled to $\hat{L}$ [157]. In this case, we use the notation:

$$^{2S+1}|\Lambda|^{+/-}_{g/u} \tag{2.4}$$

Λ is the projection of the electronic orbital angular momentum $\hat{L}$ onto the internuclear axis, S is the electronic spin angular momentum.

2.1.3 Electronic ground state

The electronic ground-state potential belongs to Hund's case (a). It asymptotes to the $^1S_0 + ^1S_0$ dissociation threshold, and has the symbol $X^1\Sigma^+_g$. In this case $\Omega = 0$ since there is no contribution from orbital or spin angular momentum of the electrons. Since the atoms are in the same electronic state, the reflection and inversion symmetries must both be even ("+" and "gerade"). Despite being a good candidate for Hund's case (a) notation, it is sometimes described with Hund's case (c) notation, in which it has the notation $X0^+_g$.

2.1.4 Electronic excited states

For bosonic homonuclear dimers, J must be even for 0^+_g states, and odd for 0^+_u. Exchanging the identical bosonic nuclei corresponds to a parity transformation on the molecular rotational wave-

function and inversion of the electronic wavefunction. For $\Omega = 0$, the rotational wavefunctions are spherical harmonics with parity eigenvalues $(-1)^J$. Inversion of the electronic wavefunction gives a factor of (+1) for gerade and (-1) for ungerade states. The overall product must be (+1) since the atoms are bosons, so J must be even in 0_g^+ and odd in 0_u^+ [158].

We use several excited-state potentials that are most relevant for the clock operation, best described by Hund's case (c). The $(1)0_u^+$ and $(1)1_u$ potentials asymptote to the $^1S_0 + ^3P_1$ threshold. These potentials arise from spin-orbit mixing of the underlying potentials, producing avoided crossings. The deeply bound rovibrational states of $(1)1_u$ that lie below the $(1)0_u^+$ potential predominantly derive from the $a^3\Sigma_u^+$ potential.

The $(1)0_u^+$ potential is the lower product of the avoided crossing between the $A^1\Sigma_u^+$ and $c^3\Pi_u$ potentials [Fig.2.2]. Its deeply bound states are largely from the $A^1\Sigma_u^+$ potential (which asymptotes to $^1S_0 + ^1D_2$), and they therefore have singlet-singlet transitions. The weakly bound states of $(1)0_u^+$ are largely from the $c^3\Pi_u$ potential and have narrower linewidths.

2.2 Sample preparation

As mentioned previously, we heat a solid sample of strontium up to $\sim$ 500 ℃, and produce a hot atomic beam. We perform Zeeman slowing on the $^1S_0 \leftrightarrow ^1P_1$ transition. After the two-stage MOT, we transfer directly into a 1D horizontal optical lattice. This is formed by a retro-reflected infrared laser.

2.2.1 Photoassociation

Photoassociation (PA) involves exciting two colliding atoms into a bound molecular state. Weakly bound vibrational states in the excited-state potentials near the $^1S_0 \leftrightarrow ^3P_1$ atomic transition have linewidths that are roughly twice that of the atomic intercombination line. This creates an array of narrow weakly bound states near the atomic threshold [86], which are favorable PA pathways compared to alkali atoms. The PA rate depends on density [85], and the thermal distribution of atoms leads to smearing of the PA lineshape [159]. After exciting to a weakly bound excited

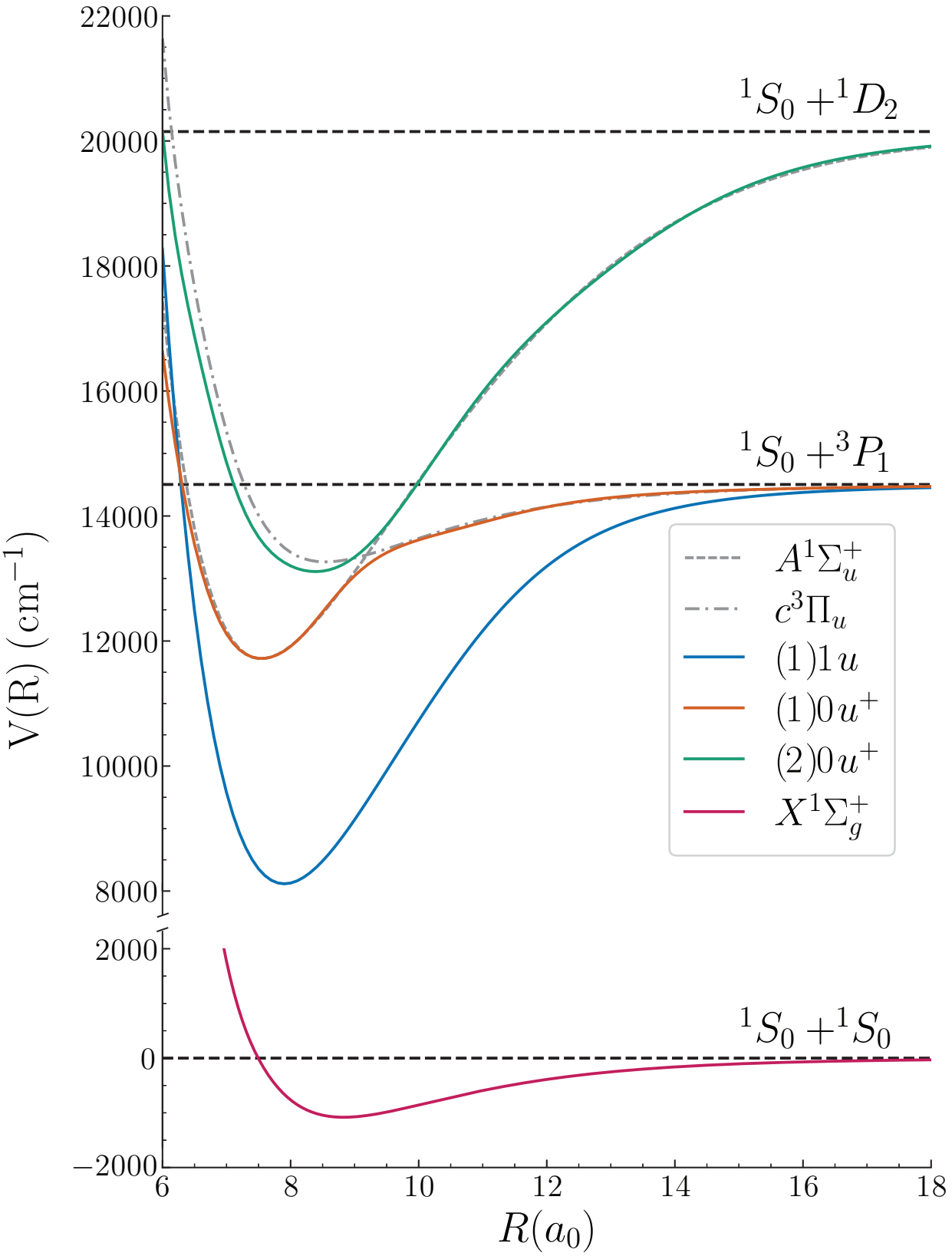

Figure 2.2: Summary of the relevant molecular potentials for Sr_2 clock operation. The excited-state potentials used for clock operation, $(1)0_u^+$ and $(1)1_u$, both asymptote to the $^1S_0$+$^3P_1$ threshold and are the product of spin-orbit coupling. The $(1)0_u^+$ potential is the product of the avoided crossing between the $A^1\Sigma_u^+$ and $c^3\Pi_u$ potentials. The deeply bound states of the $(1)1_u$ potential are from the $a^3\Sigma_u^+$ potential.

molecular state, the molecules decay to an array of states in the ground-state potential. According to Fermi's golden rule, the decay branching ratios depend on the transition strength between the excited state and ground states. The overlap of the vibrational wavefunction, called the Franck-Condon factor, determines the vibrational branching ratio, whereas the rotational factor determines the decay to different rotational states. Depending on our desired initial state in the ground-state potential, we can select the excited state with the greatest corresponding transition strength.

2.2.2 Photodissociation

Photodissociation involves exciting a molecule in the ground-state potential either to the $^1S_0$+$^3P_1$ atomic threshold or to a weakly bound state in the excited-state potential, which then decays to the ground-state threshold. Our detection scheme requires photodissociating molecules first, then absorption imaging atoms, which we do at the end of every cycle. Photodissociation is state-selective, making it a powerful tool for exploring quantum chemistry. The angular distribution of fragments (resolved axially) after time-of-flight can be used to diagnose the initial quantum state [129, 130, 156, 160]. When we dissociate the $J = 0$ rotational state, the nearby $J = 2$ state is also dissociated. The difference in binding energy is converted to kinetic energy which we observe as an outer ring on imaging [Fig. 2.3].

2.3 Clock transition

Our molecular clock transition is a two-photon Raman transition between vibrational states in the ground-state potential of Sr_2. $^{88}Sr_2$ and $^{86}Sr_2$ both have 63 $J = 0$ vibrational states in the ground-state potential, meaning we have a wide array of clock states to choose from. For the $^{88}Sr_2$ clock evaluation, we chose one spanning the entire potential, between $v = 63 \leftrightarrow v = 0$. Since the bosonic isotopes of Sr have no nuclear spin, the $J = 0$ rotational states in the ground-state potential have no magnetic moment. This is advantageous for clock operation, since this means that we are first-order insensitive to magnetic field. The fundamental lifetime of the clock states is only limited by scattering due to blackbody radiation (BBR), with a lifetime of $> 10^5$ years [161], meaning our

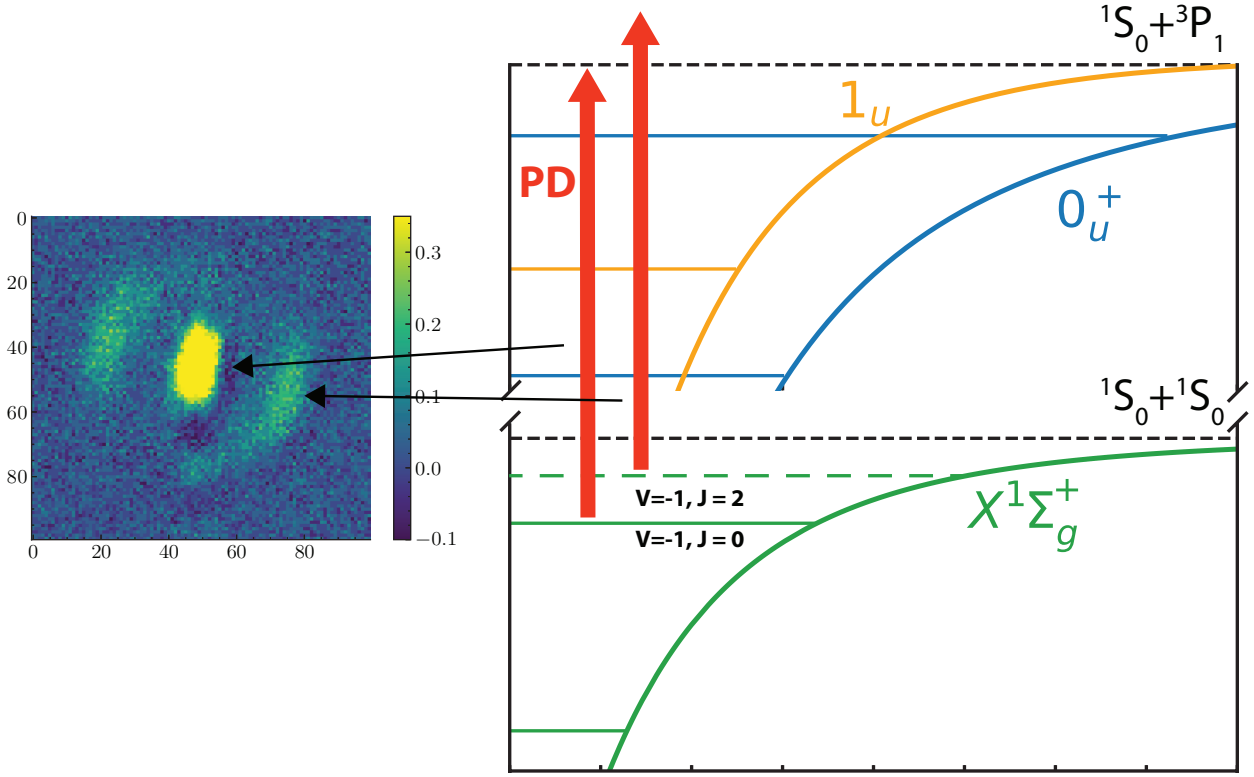

Figure 2.3: Diagram of one example of photodissociation, where the $J = 0$ least-bound vibrational state is excited to the threshold. The $J = 2$ state is also excited above the threshold, and the additional energy is converted to kinetic energy, forming an outer $J = 2$ ring around the inner $J = 0$ ring.

Q-factor will always be limited by technical factors. Currently, our lifetime is limited by two-body collisional loss [162] and scattering loss due to the lattice.

2.3.1 Magic wavelength

The groundbreaking insight that enabled atomic optical lattice clocks is the magic wavelength lattice. This technique relies on engineering the lattice such that the two clock states see the same trap potential. In a non-magic lattice, thermal sampling of the spatially varying beam profile leads to broadened clock transitions. A magic wavelength lattice creates narrow clock linewidths and eliminates the leading-order lattice Stark shift. For our molecular clock transition, we create a magic wavelength condition by tuning the lattice near an excited-state transition to a polarizability crossing. Although the polarizability is typically monotonic with vibrational state, tuning the lattice wavelength near a transition creates a dispersive feature in the polarizability, and generates a polarizability crossing [Fig.2.4(b)]. We seek out the excited-state transition with the largest transition strength, so that we can maximize detuning and limit loss from scattering. For $^{88}Sr_2$, the transition strengths were measured between deeply bound states in the X potential and those of the $1u$ potential [163].

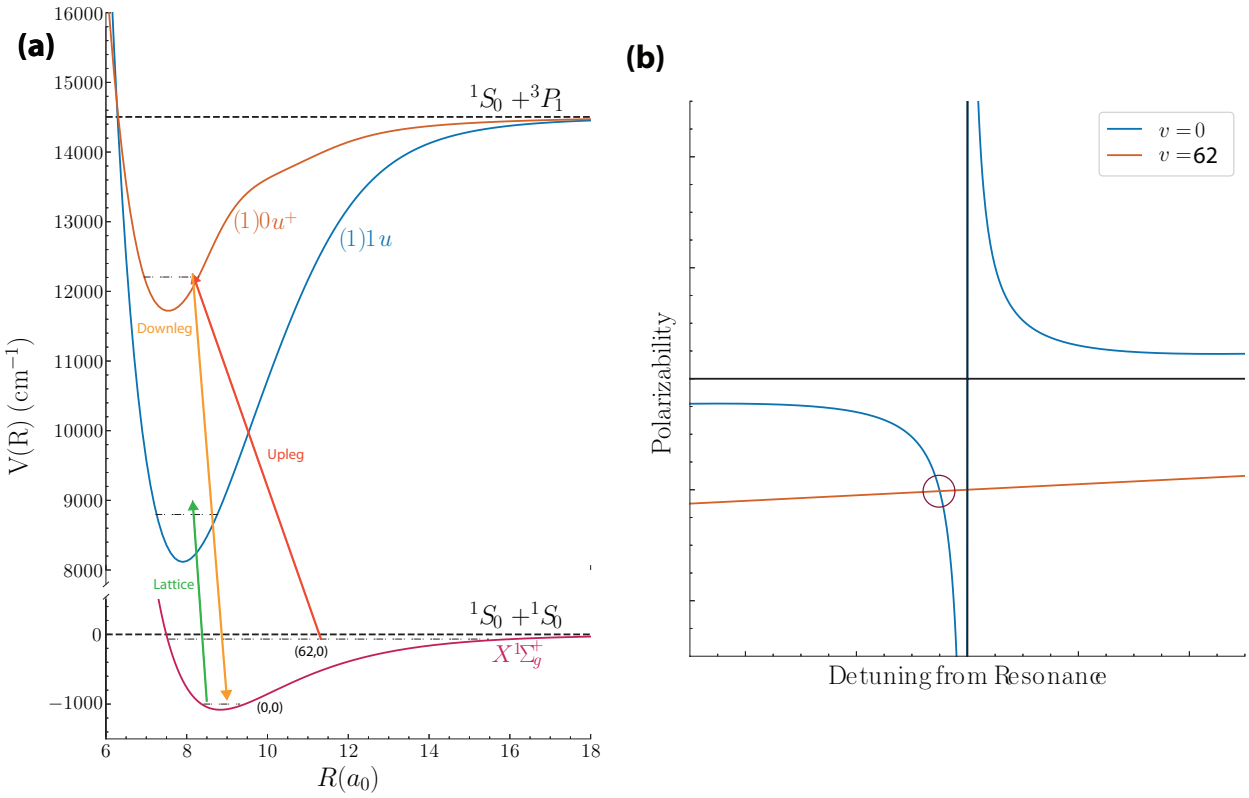

Figure 2.4: (a) Clock laser diagram, including the lattice coupled to 1u state. (b) Polarizability crossing to create the magic wavelength condition.

Chapter 3: Clock evaluation and blackbody radiation shift

3.1 Molecular clock

We measured a transition spanning the $X^1\Sigma_g^+$ ground-state potential from the $v = 62$, $J = 0$ state to the $v = 0$, $J = 0$ in $^{88}Sr_2$. We choose the rotationless states so that our clock transition is insensitive to magnetic field. Our transition was measured to be 31 825 183 207 592.8(5.1) Hz, with a fractional systematic uncertainty of 4.6×10^{-14}. This is a record for molecular spectroscopy and an important milestone. Our absolute frequency metrology is limited by the precision of our local timebase, a commercial rubidium clock. Several limitations remain that can be addressed in future iterations of the clock. Our coherence time is limited on the time scale of $\sim$ 100 ms by lattice-scattering and molecular two-body collisions. During the lattice lightshift systematic evaluation, we observed hyperpolarizability, which is the quadratic dependence of lightshift on trap intensity. We referenced our clock measurement via Global Positioning System (GPS) to the NIST time standard. We evaluated all systematics, with the lattice and probe lightshift being the dominant ones. Our results establish a benchmark for future improvements in molecular clock metrology, and enable future measurements such as molecular isotope shifts.

3.1.1 Collisions and coherence time limits

Our natural clock Q-factor is effectively infinite, so our clock precision is limited by technical factors, since we estimate that we have BBR-limited lifetimes of $> 10^5$ years [161]. The precision to which we can know our transition frequency is limited by accessible linewidths. These linewidths are Fourier limited by our probe coherence time. This, in turn, is limited by the lifetimes of the clock states. To create our magic wavelength condition, we rely on tuning the polarizability of our deeply bound $v = 0$ clock state near a $1u$ transition. This polarizability crossing allows us

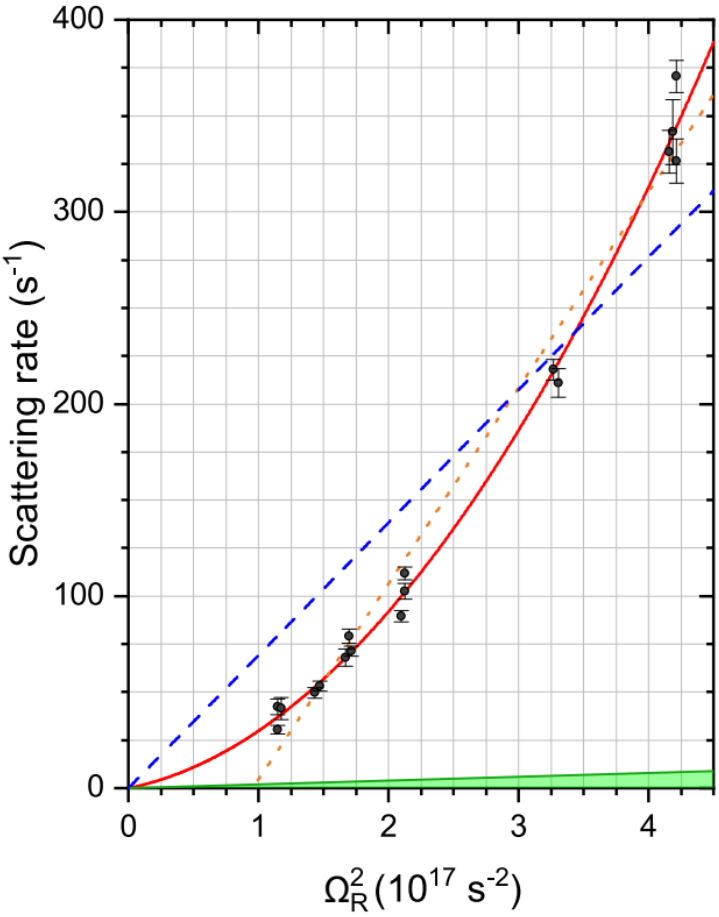

Figure 3.1: Scattering rate vs. intensity for a magic wavelength lattice[158]. The blue dashed line is a linear fit to the data, with the intercept fixed at the origin, and the orange dashed line is a linear fit with the intercept as a free parameter. The red line is a quadratic fit.

to reach narrow linewidths while reducing the lattice lightshift. The downside of this configuration is that our operational magic detuning is 4.494(1) GHz [158], and we drive some off-resonant scattering to the excited $1u$ state, which causes molecular loss. Interestingly, if one-photon scattering were the only loss mechanism, we would expect lifetimes exceeding 1 s. Instead, we observe lifetimes on the order of tens of milliseconds [164]. Additionally, we observe a quadratic dependence of scattering rate on intensity [Fig. 3.1], which is consistent with two-photon scattering. Two-photon dissociation is therefore a plausible loss mechanism.

In a non-magic lattice, our lifetime is limited by collisional loss. In a magic wavelength lattice, our lifetime is limited to 100 ms [Fig. 3.2]. This limits our accessible linewidths to roughly 10

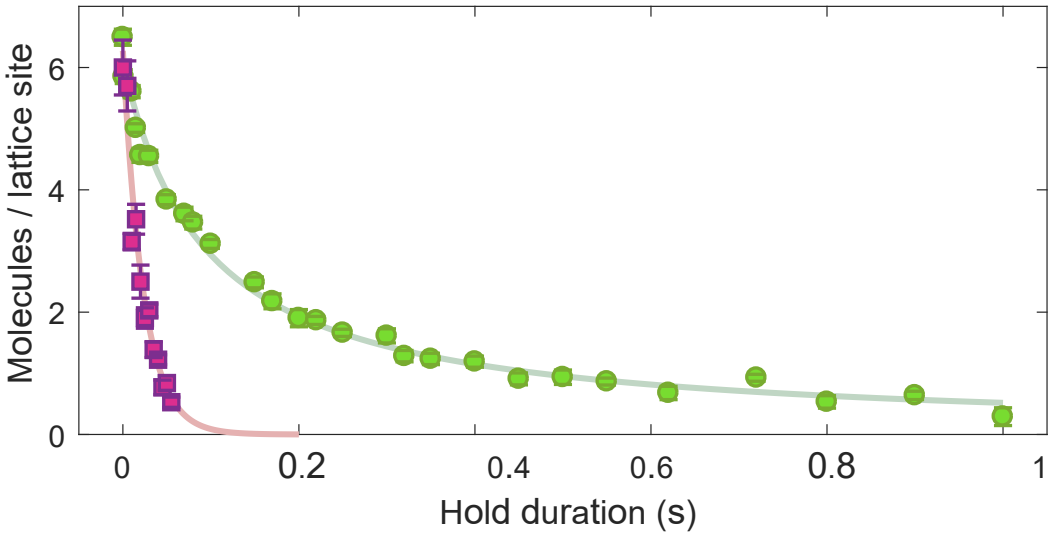

Figure 3.2: The molecular lifetime is dramatically shortened in a magic wavelength lattice (purple squares) as compared to a non-magic lattice (green circles)[161].

Hz. This corresponds to a Q-factor of $\frac{\delta f}{f} \sim 3 \times 10^{-13}$. In future iterations of the clock, we hope to address both lifetime limitations.

To further study collisional loss, we measured the lifetimes of each clock state individually in a non-magic lattice [162]. In order to do this, we performed stimulated Raman adiabatic passage (STIRAP) to efficiently and coherently transfer our molecular population into the $v = 0$ absolute ground state. STIRAP is a two-photon coherent population transfer technique that uses a counter-intuitive pulse sequence to adiabatically move population between states in a Raman configuration [165]. It has been used successfully to transfer bialkali atoms into their absolute ground state [166–176]. We would expect to have no collisional loss of the absolute ground state, since there are no bound states with lower absolute energy. Despite this, we measured the lifetimes of both of our clock states [Fig. 3.3], and observed collisional loss near the universal loss rate [177]. The universal loss rate is the maximum two-body inelastic collision rate for pairs of particles interacting through a van der Waals potential. To address this, we perform clock spectroscopy with approximately one molecule per lattice site.

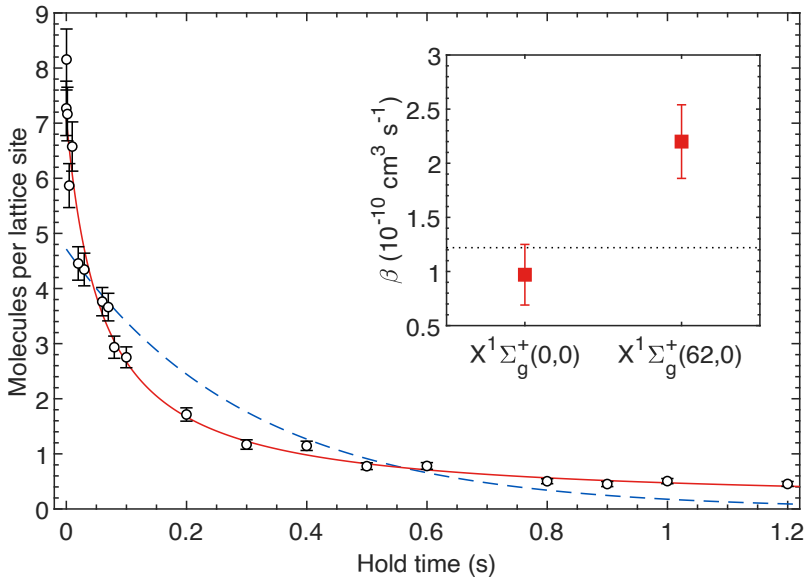

Figure 3.3: Collisional losses of molecules in the absolute ground state $X(0,0)$. The blue dashed curve is a fit to exponential loss, corresponding to one-photon scattering loss. The red curve is a fit to the rate equation $\dot{N} = -kN^{\gamma}$, indicative of two-body loss. The inset shows the two-body loss rates for the $X(0,0)$ and $X(62,0)$ vibrational states.

3.1.2 Metrology

Our clock metrology relies on the use of an optical frequency comb as our reference. The optical frequency comb was the breakthrough that enabled optical lattice clocks[12, 178–182]. Frequency combs transfer stability from the radiofrequency domain to the optical domain. They are based on pulsed femtosecond lasers. In our case, the output is amplified by an erbium doped fiber amplifier and broadened by a photonic crystal fiber to cover a wide frequency range. The parameters for the comb are the carrier envelope offset (CEO), which is the offset of the first comb tooth from 0 frequency, and the repetition rate (RR), which is the frequency spacing of the comb teeth [Fig.3.4].

$$\omega_n = n \times \omega_r + \omega_0 \tag{3.1}$$

The carrier-envelope offset arises from the phase slip between the carrier and envelope that accumulates from pulse-to-pulse. The clock lasers are locked to the comb, and so these parameters

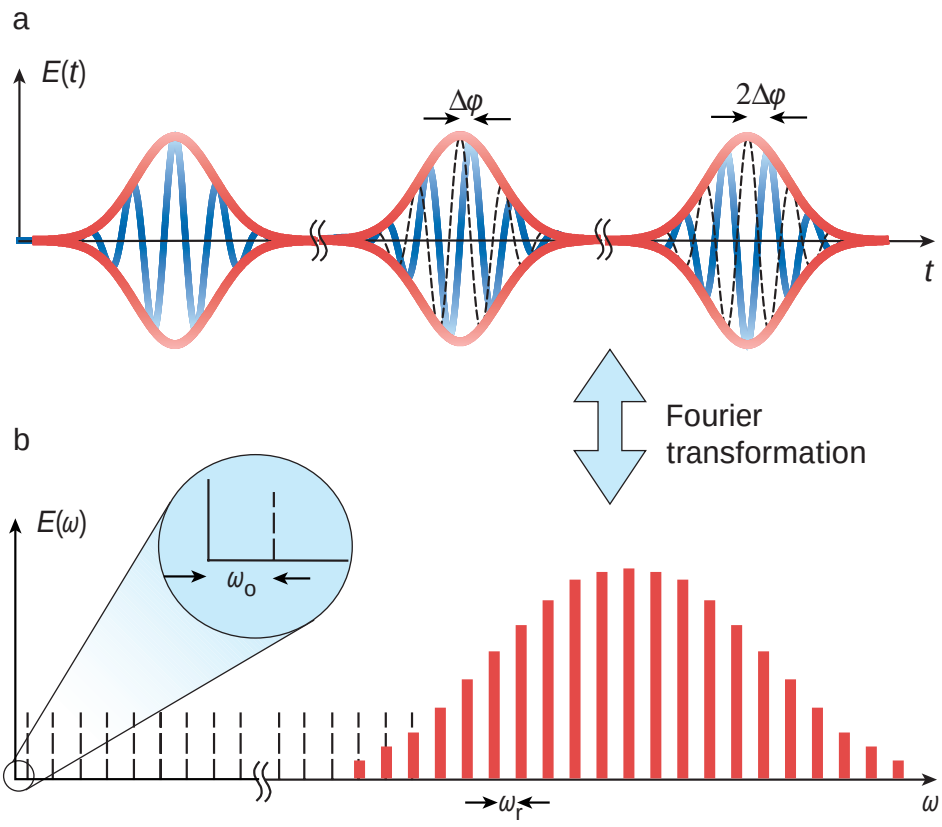

Figure 3.4: (a) Consecutive pulses from a laser. The difference between the carrier wave velocity, and the envelope group velocity creates a phase shift $\Delta\phi$ between pulses. (b) This phase shift results in a frequency offset $\omega_0 = \Delta\phi/T$, where T the time between pulses. The spectrum consists of the frequency offset of the first comb tooth, ω_0, and the spacing between comb teeth, ω_r, which is also the pulse repetition frequency [181].

go into the clock frequency.

We use a commercial rubidium clock as our local timebase. To reference absolute frequency, we use a Tallysman TW3972XF rooftop antenna that receives GPS L1 and L2C signals from NIST, fed to a SparkFun ZED-F9T GPS receiver that outputs a 1 PPS signal. We previously used a GPS disciplined oscillator (GPSDO). Unfortunately, we found that steering the rubidium clock directly with the GPSDO caused large $\sim 10^{-12}$ jumps, enough to shift the observed clock transition by ~ 30 Hz. To avoid this, we leave the rubidium clock free-running and instead implemented a time interval counter to count the drift between a 1 PPS from the GPS signal, and 1 PPS from the free-running rubidium clock [Fig.3.5]. We corrected for this drift in post-processing when calculating the absolute frequency. The rubidium clock feeds a 10 MHz signal to a distribution amplifier,

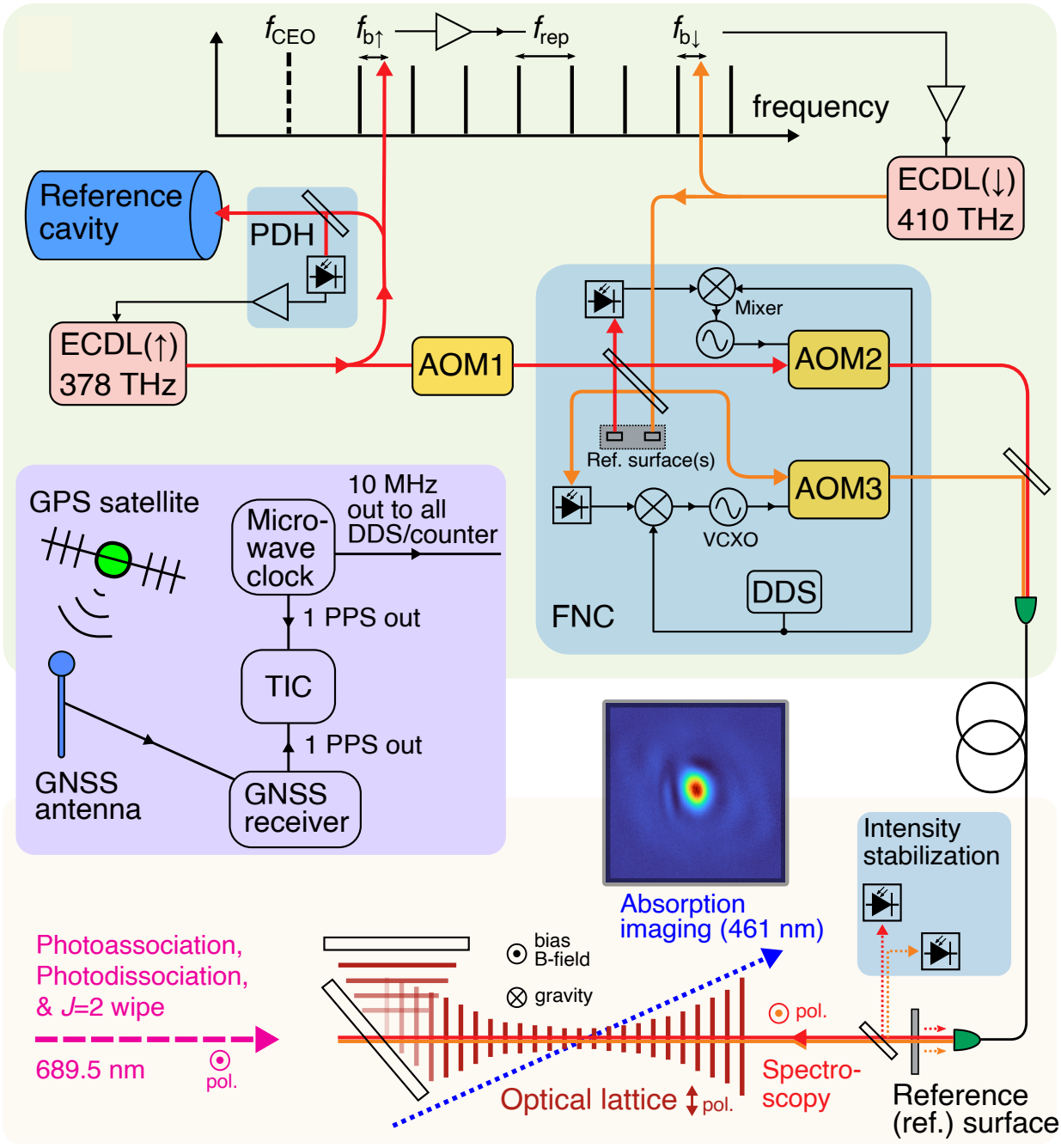

Figure 3.5: Frequency metrology chain for clock measurement. A time interval counter measured the drift of our rubidium clock relative to a GPS signal from NIST. The rubidium clock supplies a radiofrequency for the relevant frequency chain components, including frequency generators and frequency counters. The clock upleg is referenced to a high-finesse reference cavity, and the repetition rate of the comb is stabilized to this laser.

which outputs 10 MHz signals to the relevant frequency generators and references. These include direct digital synthesizers (DDS) that drive acousto-optic modulators (AOM), which control our clock lasers and the lattice laser. This is also the reference for our frequency counter, which records the repetition rate and carrier envelope offset for the comb.

The clock lasers consist of the upleg at $\sim$ 793 nm, which connects the $X(62, 0)$ state to the $0_u^+(11, 1)$, and the downleg at $\sim$ 732 nm, which connects the $0_u^+(11, 1)$ state to the $X(0, 0)$ absolute ground state. The upleg laser is Pound-Drever-Hall locked [183] to a high-finesse cavity [Fig.3.5], which serves as our optical frequency reference. The CEO of the comb is locked to a 10 MHz reference from the rubidium clock, and the nearest comb tooth is phase-locked to the upleg laser. This stabilizes the repetition rate of the comb. The clock frequency is given by the difference in frequency of the upleg and downleg lasers at the molecules' location. This is given by the comb tooth difference, AOM offset for each laser, and the beat frequency between the laser and the comb. Intensity stabilization and fiber noise cancellation (FNC) are implemented on the clock-laser delivery path to suppress path-length fluctuations.

3.1.3 Hyperpolarizability

During the evaluation of the lattice lightshift systematic, we observed hyperpolarizability [Fig.3.6]. This is the nonlinear dependence of the lightshift on the lattice trap depth. We write the clock shifts as[184]:

$$\Delta f_{clock} = -\alpha * U_0 - \beta * U_0^2, \tag{3.2}$$

where α captures the electric-dipole ($E1$), magnetic-dipole ($M1$) and electric-quadrupole ($E2$) polarizabilities and β captures the hyperpolarizability. Both coefficients are determined empirically from fits to the measured lightshifts.

The origin of this behavior is not fully understood, but we hypothesize it may be related to some two-photon scattering process. Similar effects have been reported by atomic clock groups [184]. The presence of this hyperpolarizability precludes the use of a perfectly magic wavelength

lattice. Instead, we tune the polarizability, α, and the hyperpolarizability, β, such that the lightshift is first-order insensitive to intensity fluctuations at the operational trap depth, $\sim 500\ E_R$. Further investigation is necessary to determine the cause of this effect.

Our lattice light source is a Titanium Sapphire laser, set to our magic wavelength of ~ 1005 nm. The precision of the lattice wavelength is especially crucial, so we also stabilize the lattice by locking to the frequency comb. We use a standard beat phase-lock to the comb and feed back to a voltage-controlled oscillator (VCO), controlling the frequency of an AOM. AOMs have a limited bandwidth, so in order to keep the VCO close to the optimal AOM frequency, the servo output monitor is fed back to the "fast" resonator piezo of the Ti:Sapph laser.

3.1.4 Results

We evaluated all of the relevant systematics and measured the absolute frequency of the molecular clock transition spanning the ground-state potential of $^{88}Sr_2$. The clock precision can be averaged down over time. The metric for this precision is the Allan variance [185–187]:

$$\sigma_y^2(\tau) = \frac{1}{2(M-1)} \sum_{i=1}^{M-1} \left[\langle y(\tau)\rangle_{i+1} - \langle y(\tau)\rangle_i\right]^2 . \tag{3.3}$$

We evaluated the Allan deviation, $\sigma_y(\tau) = \sqrt{\sigma_y^2(\tau)}$, for our clock transition [Fig.3.7]. Our clock up-time is limited by the stability of our system, especially the phase-locks of the lock lasers to the frequency comb. Further improvement of laser-lock stability could improve the up-time, and improve the statistics for this measurement.

Each systematic is evaluated by deliberately varying the relevant parameter and measuring the induced shift in the line center [Fig. 3.8], then extrapolating back to the unperturbed clock frequency. The uncertainty for each systematic is set by the precision with which we can determine the line center at each data point.

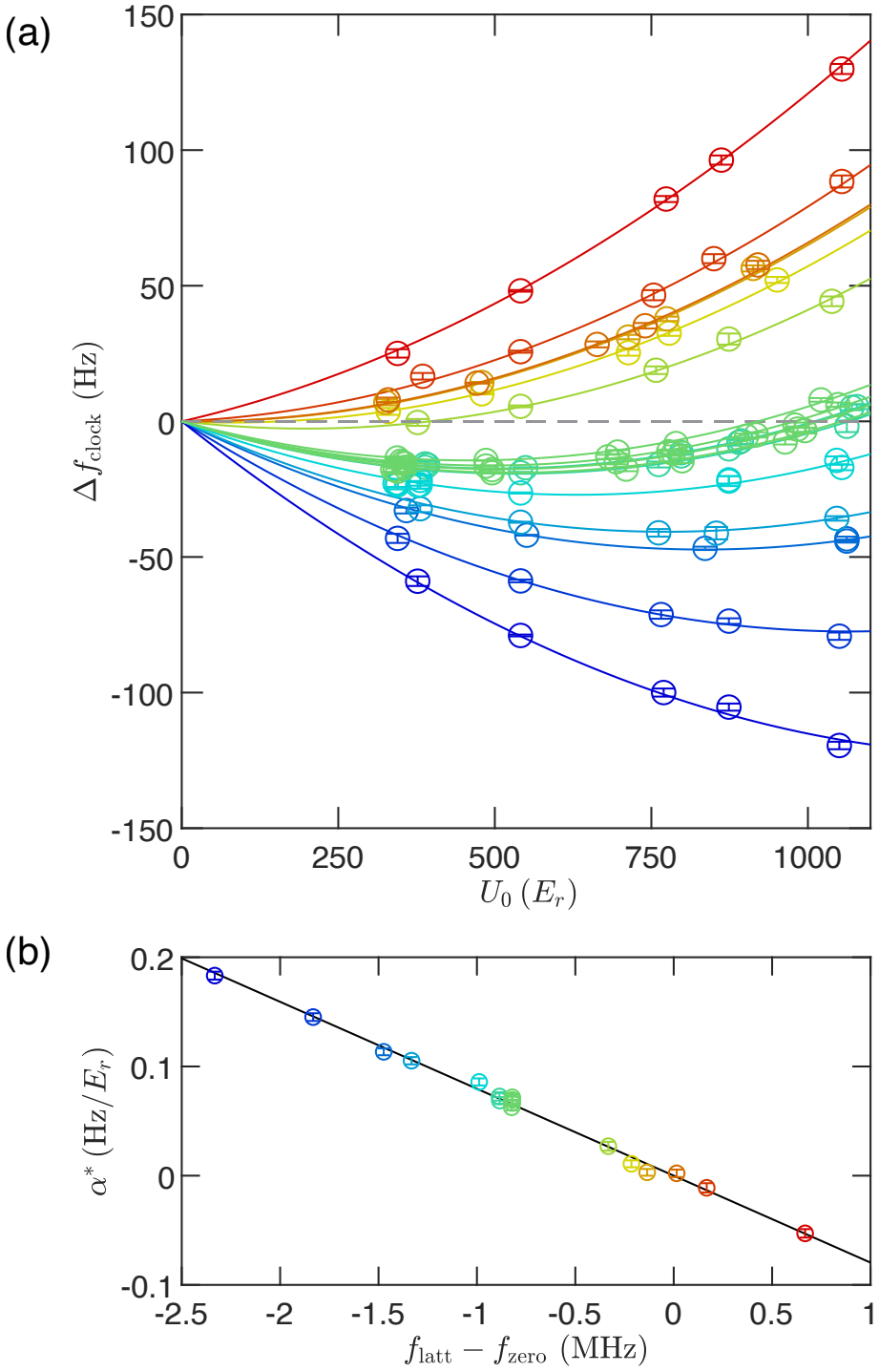

Figure 3.6: Lattice Stark shift of clock transition. (a) Nonlinear shift of clock transition at a range of lattice frequencies (different colors). The lines correspond to parabolas fit to the data. The operational lattice wavelength was chosen such that the curve is first-order insensitive to lattice power fluctuations at the operational intensity ($\sim 500\ E_R$) (b) Linear light-shift polarizability coefficient $\alpha*$ vs. lattice frequency.

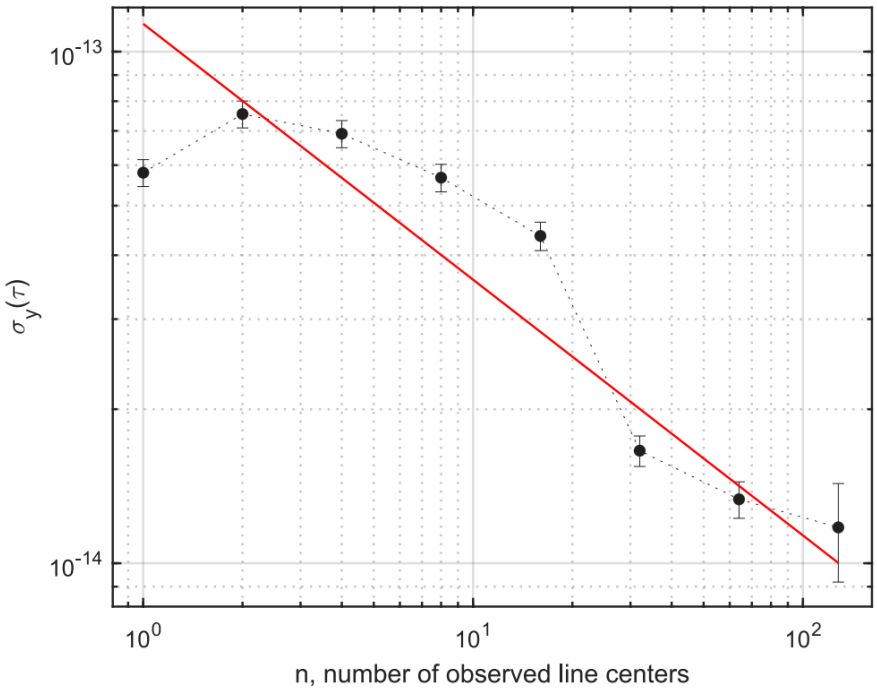

Figure 3.7: Allan deviation when the experimental parameters are left unchanged, as a function of observed line centers, n. The Allan deviation goes down as $\sim 10^{-13}/\sqrt{n}$ [158].

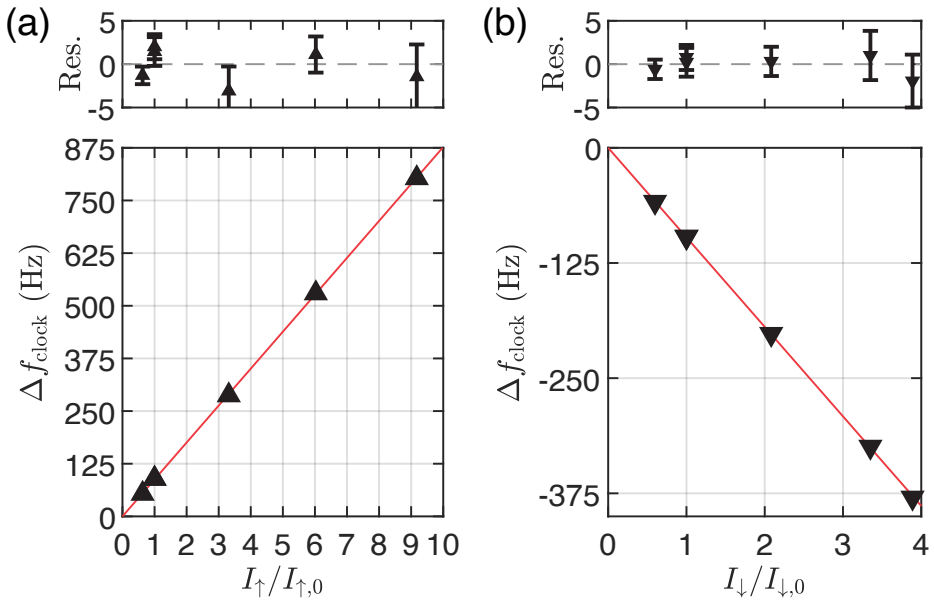

Figure 3.8: Light-shift evaluation for the probe lasers. (a) Upleg laser light-shift. (b) Downleg laser lightshift. Residuals and errors are shown in upper plots.

The dominant effects come from the lattice and probe lightshifts [Table 3.1]; the density-dependent shift is also evaluated. Reducing the systematic uncertainty requires lower line-center uncertainties, which in turn requires narrower Fourier-limited linewidths, and therefore longer coherence times. After coherence time is improved, the BBR systematic shift will be the limiting factor, one that is especially difficult to control and limit.

Table 3.1: Systematic uncertainty budget for the strontium molecular clock under operating conditions. All values are expressed in fractional units ($\times 10^{-14}$).

Systematic	Correction	Uncertainty
Lattice Stark ($E1, M1, E2$)	100.1	3.4
Lattice Stark (hyperpolarizability)	-50.8	1.9
Probe Stark (total)	31.5	2.2
BBR	-2.2	0.4
Density	-0.6	0.3
Quadratic Zeeman	0	0.05
dc Stark	0	< 0.1
Doppler and phase chirps	0	< 1
Lattice tunneling	0	< 0.1
Line pulling	0	< 0.1
Scan-and-fit	0	< 0.6
Total	77.9	4.6

3.2 Blackbody radiation systematic shift

After improving coherence time to narrow accessible Fourier limited linewidths, the lightshift and density shift uncertainties will also be reduced. Once these are reduced, the BBR shift will become the dominant source of uncertainty, and it lacks a straightforward path to reduction. It is a leading systematic for atomic clocks [188–195], and is a notoriously difficult systematic to constrain [196–198], so we consider this a priority for future investigation. Our clock evaluation relied on theoretical modeling that lacked experimental validation [154]. Here, we compare experimental measurement of dynamic polarizabilities to ab initio theoretical calculations at an infrared wavelength. We observe good agreement between theory and experiment, and extend theory to calculate clock state polarizabilities at a range of infrared frequencies. We use these calculated

polarizability values to determine the blackbody radiation shift for our clock transition at the 10^{-16} level, which paves the way to an improvement by up to two orders of magnitude for our clock. The Sr_2 molecular clock provides an array of potential clock states, so we explore the BBR shift for different combinations of clock states.

3.2.1 Infrared polarizability measurement

We measured the lightshift induced by a $\sim$ 1950 nm laser on two-photon Raman clock transitions to a range of selected clock states. We initialized the population via one-photon photoassociation targeting $X(62, 0)$ as the initial state. To initially locate each transitions, we use Autler-Townes spectroscopy, where the upleg laser is kept on, and the downleg laser is scanned until recovery is observed. For the clock transition, we used a detuning of +30 MHz from the intermediate state. To address clock states throughout the potential well, we used three different intermediate states in the excited $(1)\,0_u^+$ potential: $v'' = 11$ [at $-57\,084\,156.51(12)$ MHz from the $^1S_0$+$^3P_1$ threshold], $v'' = 15$ [at $-48\,855\,512.13(18)$ MHz], and $v'' = 16$ [at $-47\,036\,433.95(23)$ MHz]. The 1950 nm laser is coaligned with the clock lasers using a dichroic. We explored 8 different vibrational clock states from $X(62, 0)$.

Magic wavelength determination

We operate at 1 kHz linewidths for this spectroscopy, which requires a magic-wavelength lattice. For each clock transition, we explored several transitions to deeply bound $1u$ states in order to create the magic condition. We use a theoretical interaction model to calculate transition dipole moments to $1u$ for a potential magic wavelength. We chose the $1u$ states with line strength $\gtrsim 10^{-5} e^2 a_0^2$. We measure several dispersive curves, indicating resonances from the ground clock state to the $1u$ state [Fig. 3.9]. For each curve we measure lightshift as a function of lattice wavelength at several values around the resonance. We fit the equation:

$$\Delta_{\text{Stark}}(\lambda) = \frac{a}{\lambda - \lambda_0} + b \tag{3.4}$$

to lattice Stark shifts measured as a function of frequency to find the zero crossing, $\lambda_{\text{magic}} = \lambda_0 - a/b$. Our lattice wavelength is stabilized to a wavemeter at ~30 MHz precision.

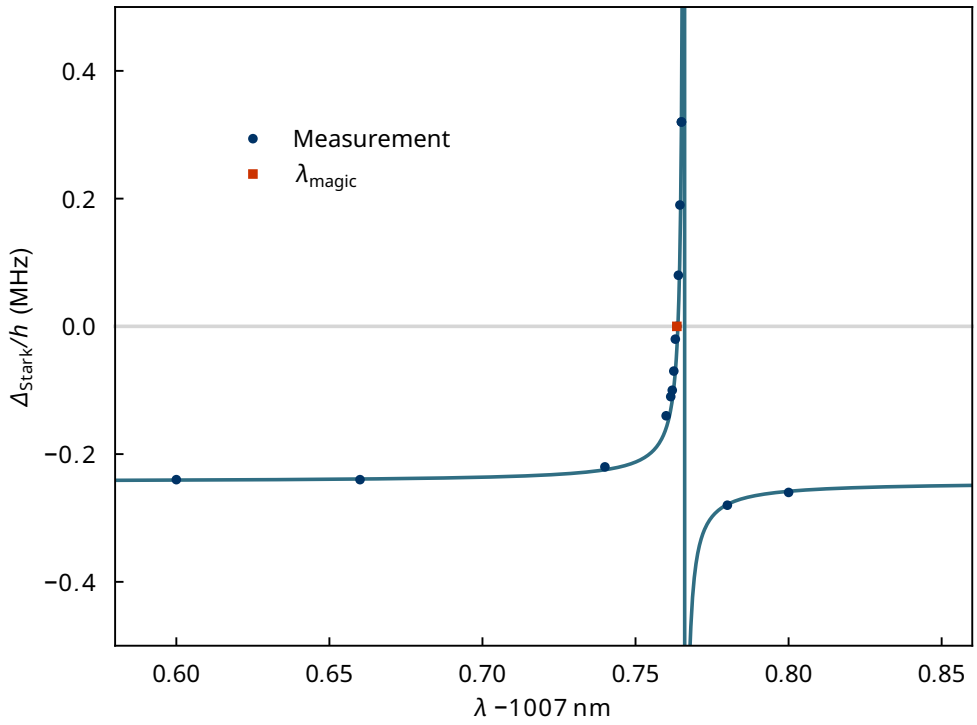

Figure 3.9: Search for the magic wavelength on the example of the $v = 12 \leftrightarrow v' = 62$ molecular clock transition. Points denote the experimental lattice-induced ac Stark shift as a function of lattice laser wavelength λ. The fitted function is Eq. (3.4). The red square indicates the magic wavelength $\lambda_{\text{magic}} = 1007.7634(10)$ nm, where the Stark shift Δ_{Stark} is cancelled out.

Differential polarizability measurement

For each clock transition, we measure the clock peak position at several different powers of the 1950 nm Stark beam [Fig.3.10]. For each scan, we fit a Lorentzian lineshape with the form:

$$n(\Delta) = n_0 - \frac{A}{2\pi} \frac{\gamma}{(\Delta - \Delta_c)^2 + (\gamma/2)^2}, \tag{3.5}$$

where n_0 is the background dissociated atom number, A is the area, γ is the full width at half maximum, and Δ_c is the center frequency. We typically operate with 1 kHz peak widths and can measure peak position to ~100 Hz.

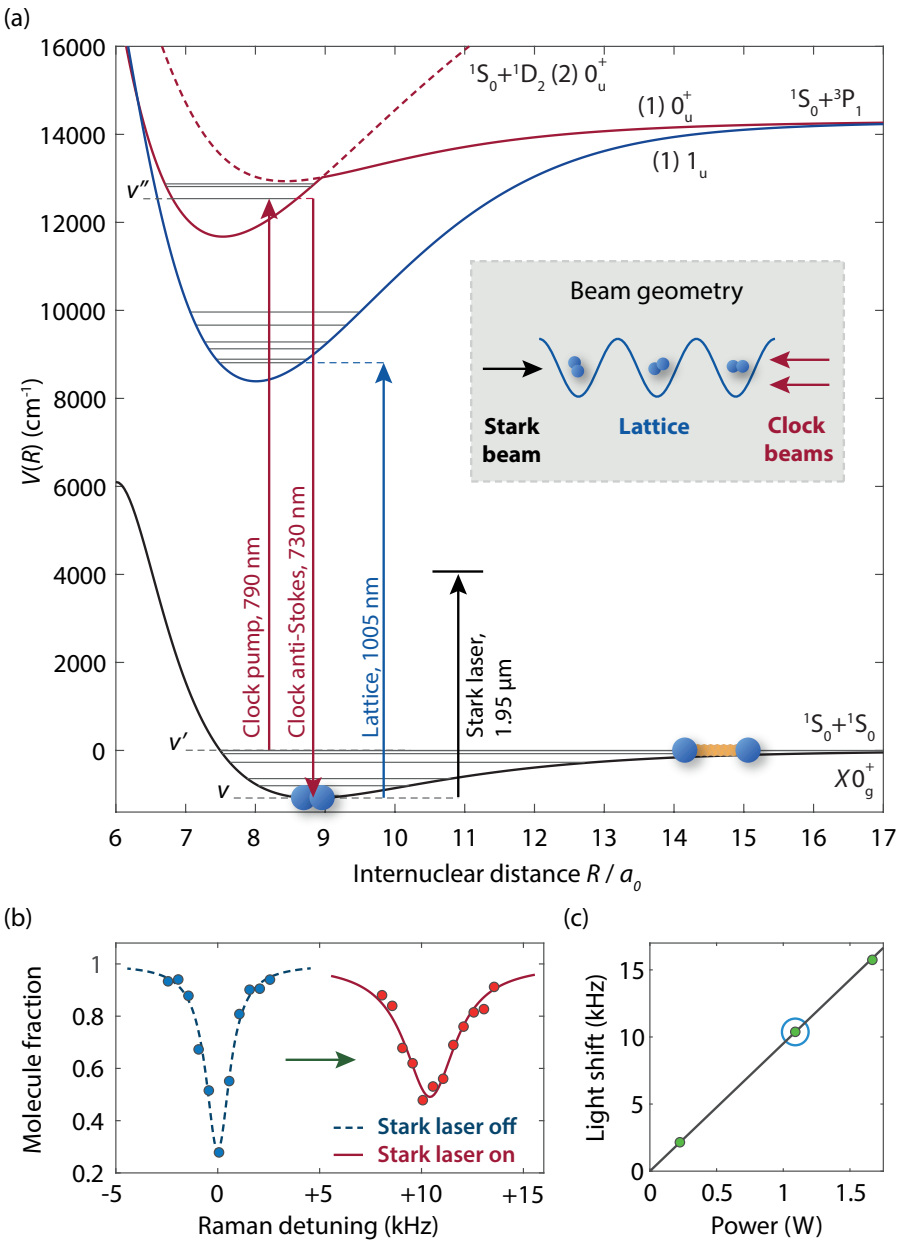

Figure 3.10: Stark shift spectroscopy in a Sr_2 molecular clock on the example $0 \leftrightarrow 62$ transition. (a) Our molecular clock relies on narrow two-photon Raman transition via an intermediate state in the $(1)\,0_u^+$ (red arrows) in a magic lattice that couples the deeply-bound clock state v to an excited $(1)\,1_u$ state (blue arrow). (b) We induce Stark shifts to probe differential polarizabilities of ground ro-vibrational states with 1.95 µm light. (c) Example light shift measurement. The encircled data point corresponds to the spectrum shown in (b).

We then fit a line as a function of Stark-laser power. The resulting slope is proportional to the differential polarizability between the two clock states. As long as we do not change the beam waist, we can directly compare the relative differential polarizabilities for different clock states.

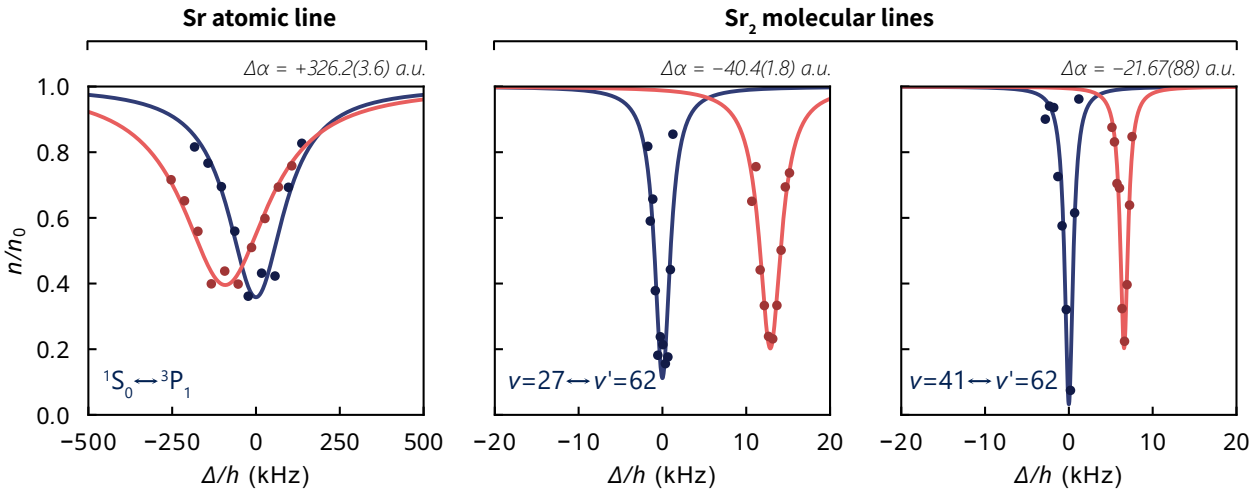

Figure 3.11: Example lineshapes seen in our ac Stark shift measurements. To determine the differential ac polarizability, we measure a lineshape each with the extra ac Stark laser off (dark blue) and on (light red). To determine the differential polarizabilities $\Delta\alpha$ we measure ratios of ac Stark shift slopes between different transitions. As an absolute reference we used the narrow $^1S_0 \leftrightarrow ^3P_1$ atomic intercombination transition with a known $\Delta\alpha = +326.2(3.6)$ a.u. [199]. The molecular ac Stark shifts were compared to a common $27 \leftrightarrow 62$ transition which were then calibrated to the atomic line.

This method yields differential polarizabilities between the $X(v, 0)$ and $X(62, 0)$ clock states. To calibrate the measurement, we reference to a known polarizability: the atomic $^1S_0 \leftrightarrow ^3P_1$ intercombination line, with $\Delta\alpha = +326.2(3.6)$ a.u. [199]. Every measurement day, we measure the lightshift slope for each $X(v, 0) \leftrightarrow X(62, 0)$ state relative to the $X(27, 0) \leftrightarrow X(62, 0)$ transition. We compare the $X(27, 0) \leftrightarrow X(62, 0)$ transition to the atomic $^1S_0 \leftrightarrow ^3P_1$ intercombination transition, in order to get an absolute value of differential polarizability in atomic units.

We can report the relative binding energies as the difference in laser frequency of the two clock legs [Table 3.2].

Uncertainty estimation

Since precise determination of transition frequencies is not the main purpose of this work, we did not characterize the Stark shifts experimentally. Instead, we calculate a conservative upper bound on the uncertainty of the binding energy by combining estimated lattice and Raman laser Stark shifts.

Using the Stark shift measured during magic wavelength determination, we fit a linear slope to Stark shift vs. lattice frequency near the operational magic wavelength. We then use this slope to convert the wavemeter-limited uncertainty of the lattice wavelength to a Stark shift, and take this Stark shift as our lattice contribution to the uncertainty of the binding energy.

Using measured laser power and waist, as well as *ab initio* polarizabilities calculated using the sum-over-states approach [200], we calculate the Raman Stark shifts,

$$\Delta f_{\text{clock}} = \frac{I_R}{2h\epsilon_0 c} \left[\alpha_0 (\lambda_R) - \alpha_{62} (\lambda_R)\right], \tag{3.6}$$

where I_R is the intensity of each Raman laser, α is polarizability for each vibrational state, and λ is the wavelength. We note that contributions from the Raman lasers have opposite signs [132]. We assign an additional conservative value of 50% to the *ab initio* polarizabilities, significantly larger than the discrepancy observed in comparison with measured polarizability ratios [154].

After estimating the lattice and Raman Stark shifts individually, we combine them to get total uncertainty on binding energy position. We find that the lattice Stark shift is about an order of magnitude greater than Raman Stark shift.

Finite sample temperature

Our experiment relies on Stark-induced shifts to molecular clock lines. Here we estimate the effect of finite sample temperature on the determination of differential polarizabilities from observed shifts.

In the absence of the Stark laser the molecules, whether in their initial (v), or target (v') vibrational states are trapped in the same magic-wavelength lattice potential. For a single lattice site this may be approximated by a harmonic trap potential:

$$V(x, y, z) = \frac{1}{2} M \omega_r^2 \left(x^2 + y^2\right) + \frac{1}{2} M \omega_z^2 z^2. \tag{3.7}$$

Here M is the mass of the molecule and $\omega_{r,z}$ are the radial (r) and axial (z) trapping frequencies.

We induce an ac Stark shift on the molecular clock $v \leftrightarrow v'$ transition by adding an extra collimated laser coaligned with the lattice which gives rise to an extra potential,

$$W(x, y, z) = \frac{1}{2} M \Omega_{v,v'}^2 \left(x^2 + y^2 \right) - U_{v,v'}, \tag{3.8}$$

where $\Omega_{v,v'}$ are the state-dependent radial trapping frequencies and $U_{v,v'}$ are the extra trapping depths. Both $\Omega_{v,v'}^2$ and $U_{v,v'}$ are directly proportional to the ac polarizabilities $\alpha_{v,v'}$ that we aim to measure. The increase in trap depth $U_{v,v'}$ leads to a temperature-independent line shift that is the basis for our experiment. However, the extra trapping frequency leads to a non-trivial temperature-dependent shift that we will evaluate here.

The total trapping potential of the combined laser beams is

$$V_{v,v'} + W_{v,v'} = \frac{1}{2} M \left(\omega_r^2 + \Omega_{v,v'}^2 \right) \left(x^2 + y^2 \right) + \frac{1}{2} M \omega_z^2 z^2 - U_{v,v'}. \tag{3.9}$$

This is equivalent to a three-dimensional harmonic oscillator with state-dependent trapping frequencies. As carrier transitions preserve the motional quantum numbers, the total shift may be evaluated as a difference of the quantum thermal averages of the trapping hamiltonians $H_{v,v'} = T + V + W_{v,v'}$:

$$\begin{aligned} \left\langle \delta E \right\rangle &= \left\langle H_{v'} \right\rangle - \left\langle H_v \right\rangle \\ &= -\Delta U + \hbar \Delta\omega \left[\left\langle n_x \right\rangle + \left\langle n_y \right\rangle + 1 \right], \end{aligned} \tag{3.10}$$

where $\Delta U = U_{v'} - U_v$ and the change in radial trapping frequency is

$$\Delta\omega = \sqrt{\omega_r^2 + \Omega_{v'}^2} - \sqrt{\omega_r^2 + \Omega_{v'}^2 - \Delta(\Omega_{v,v'}^2)}. \tag{3.11}$$

For us the transition-dependent term $\Delta(\Omega_{v,v'}^2) = \Omega_{v'}^2 - \Omega_v^2$ is on the whole substantially smaller

than either of the trapping frequencies Ω_v^2 or ω_r^2, hence we can expand $\Delta\omega$ as

$$\Delta\omega \approx \sqrt{\omega_r^2 + \Omega_{v'}^2}\left(\frac{1}{2}\frac{\Delta(\Omega^2)}{\omega_r^2 + \Omega_{v'}^2} - \frac{1}{8}\left(\frac{\Delta(\Omega^2)}{\omega_r^2 + \Omega_{v'}^2}\right)^2\right). \tag{3.12}$$

Importantly, the first term is linear in the measured differential polarizability as $\Delta(\Omega_{v,v'}^2)$ is directly proportional to $\Delta\alpha_{v,v'}$.

The mean vibrational quantum numbers for radial motion can be evaluated by averaging over the grand canonical ensemble:

$$\left\langle n_{x,y} \right\rangle = \frac{1}{Z}\sum_{n=1}^{\infty} e^{\frac{-E_n(x,y)}{k_B T}} \approx \frac{k_B T}{\hbar\omega_r}, \tag{3.13}$$

$$\tag{3.14}$$

where we used the partition function [201]

$$Z = \mathrm{Tr}(e^{-H_{v'}/k_B T}) = \frac{1}{2}\mathrm{csch}(\hbar\omega/2k_B T). \tag{3.15}$$

Finally, the total thermally averaged shift to the line is

$$\left\langle \delta E \right\rangle = -\Delta U + k_B T\frac{\Delta\omega}{\omega_r}. \tag{3.16}$$

The first term is the temperature-independent ac Stark shift. The second term is a temperature-dependent correction.

In our experiment the incoming lattice beam has a power of $P_l = 0.27$ W and a waist of $w_l = 36\,\mu$m. For all the measured transitions the wavelength of the lattice is chosen to achieve a magic condition. This means that the polarizability at the lattice wavelength for both the initial v' and target v molecular states is the same and can be modeled as twice the atomic polarizability. For the magic wavelengths ranging from $\lambda_{\mathrm{magic}} = 996.4379$ nm to $\lambda_{\mathrm{magic}} = 1016.9714$ nm the atomic polarizabilities range from $\alpha_{\mathrm{magic}} = 250.2$ a.u. to $\alpha_{\mathrm{magic}} = 247.6$ a.u., respectively. This

corresponds to total atomic trap depths

$$U_l = 4\alpha P_l/(\pi w_l^2 c\epsilon_0) \tag{3.17}$$

between 622 kHz $\times\, h$ and 616 kHz $\times\, h$ (approximately 30 μK). The factor of four stems from constructive interference between the incident and reflected lattice beams. Conversely, the radial trapping frequencies

$$\omega_r = \frac{2}{w_l}\sqrt{U_l/M} \tag{3.18}$$

of $\omega_r = 2\pi \times 469.9$ Hz to $2\pi \times 467.5$ Hz. The molecular sample temperature is estimated at 5 μK. For weakly-bound molecules the trap depth is twice that for atoms (because the polarizability is that of two atoms), however, the trapping frequencies are the same for atoms and molecules, as the extra trap depth cancels out with the twice larger mass M of the molecule.

The extra Stark shift laser has a wavelength of $\lambda = 1950$ nm and a maximum power of $P = 1.7$ W at a waist of $w = 125.9\,\mu$m. This provides an extra trap depth

$$U_v = \alpha_{x,v} P/(\pi w^2 c\epsilon_0) \tag{3.19}$$

between 67.1 kHz$\times h$ and 79.4 kHz$\times h$ *per atom in the molecule* and an extra radial confinement that varies from $\Omega_v = 2\pi \times 44.1$ Hz to $\Omega_v = 2\pi \times 48.0$ Hz. The polarizability per atom varies between $\alpha_x = 210.1$ a.u. for the most weakly bound state and $\alpha_x = 248.5$ a.u. for the rovibrational ground state.

The temperature-independent shift ΔU of up to 12.3 kHz $\times\, h$ by far outweighs the temperature-dependent term. Note that the total shift for the diatomic molecule is $2\Delta U$ and it therefore reaches 24.6 kHz $\times\, h$. The extra temperature-dependent term stems from the change in the total radial confinement of the effective trap created by the lattice and ac Stark laser. The contribution to radial trapping from the ac Stark laser is an order of magnitude smaller than the baseline provided by the lattice laser. The figure of merit is the difference in the extra confinement between different

vibrational states as compared to the lattice radial frequency. We find $\Delta\omega$ to vary between $2\pi \times 6.4 \times 10^{-4}$ Hz for a $v = 61 \leftrightarrow v' = 62$ transition and $2\pi \times 0.38$ Hz for a $v = 0 \leftrightarrow v' = 62$ line. The total temperature-dependent shift, $k_B T(\Delta\omega/\omega_r)$ is consistently below 0.7% of the temperature-independent shift, at most 84.3 Hz $\times h$ for the $v = 0 \leftrightarrow v' = 62$ transition. This is already significantly smaller than our experimental error bars.

We also point out that most of the thermal shift is, just like ΔU, directly proportional to the differential polarizability we aim to measure. In fact, the linear term in the Taylor expansion for $\Delta\omega$, Eq. (3.12) overestimates the real value by at most 0.4% making the nonlinear systematic negligible for this work.

Another possible source of systematic error is the variation in magic wavelength and the corresponding lattice radial confinement between the different molecular lines. We find that this variation contributes at most a 1.2% relative uncertainty to the temperature-dependent shift. Again, for us this contribution is two orders of magnitude smaller than our experimental uncertainty and therefore negligible.

3.2.2 Polarizability theory

To calculate the BBR shifts, we need a model of the differential polarizabilities at all wavelengths from dc to infrared. The overwhelming majority of the BBR spectrum falls at wavelengths longer than 2 μm. While we cannot experimentally probe this entire range of wavelengths, we can leverage close agreement between theory and experiment at 1.95 μm and extend theoretical models to provide a full description of the BBR shift. We use modern quantum chemistry methods to calculate the differential polarizabilities for all molecular clock transitions in two steps: first, we calculate *ab initio* electronic polarizabilities of the strontium dimer as a function of internuclear distance R, and second, we obtain the polarizability for each vibrational level as an average of the electronic polarizability over the vibrational wavefunction.

In homonuclear molecules only electronic transitions contribute to polarizabilities and BBR shifts. To calculate the electronic polarizability, we employ the approach based on asymmetric an-

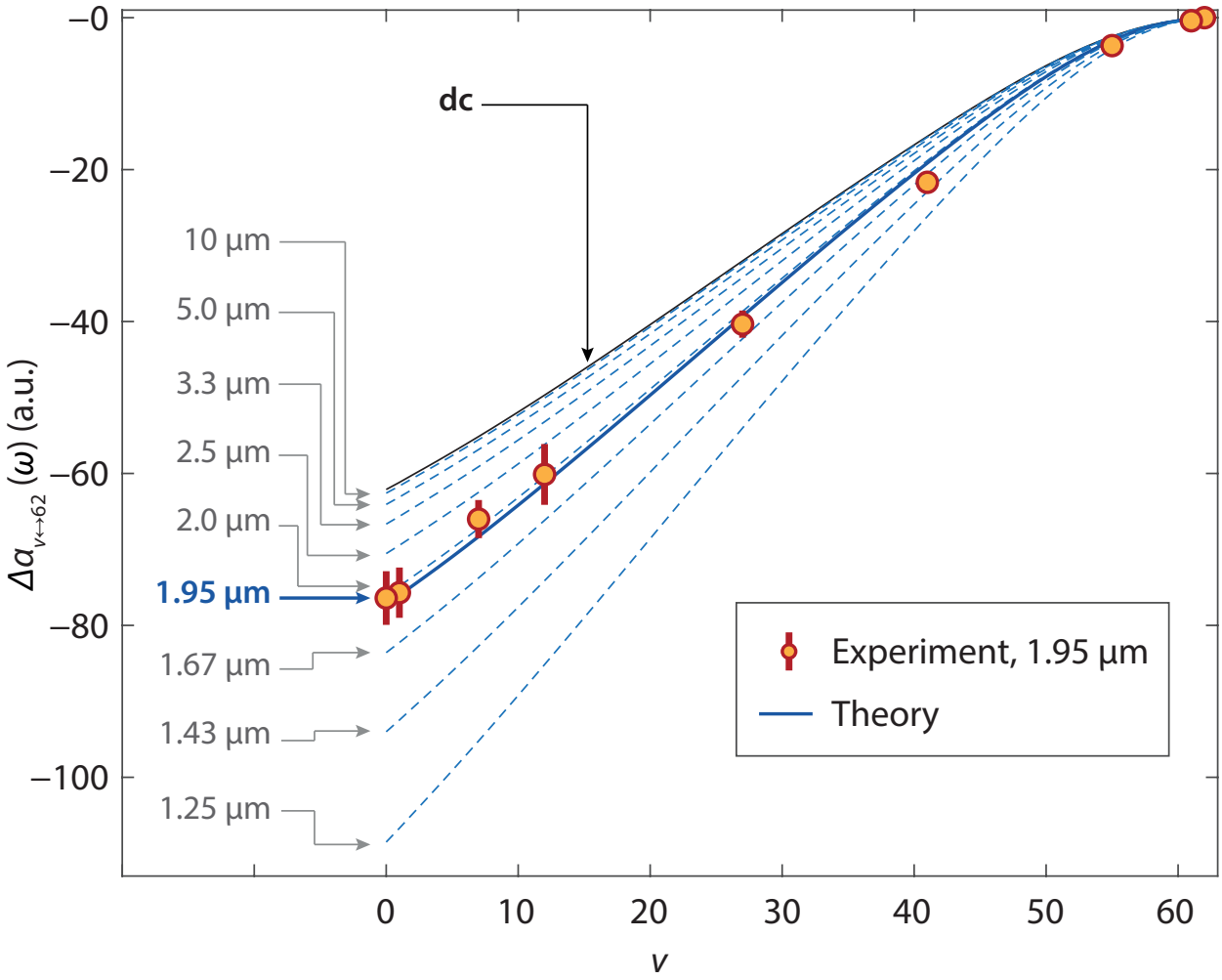

Figure 3.12: Differential polarizability with respect to the least-bound $v = 62$ state in ground state Sr_2. Points denote experimentally measured ac polarizabilities at $\lambda = 1.95\,\mu m$. Lines are *ab initio* polarizabilities from dc to $\lambda = 1.25\,\mu m$.

alytical derivative of the coupled-cluster energy with single and double excitations (CCSD) [202], as implemented in the Q-Chem 5 package [203]. We use the ECP28MDF pseudopotential together with its dedicated valence basis set [204]. For any given lattice light frequency ω, we first calculate the interaction-induced polarizability of Sr_2 molecules, $\alpha_{ij}^{\text{int}}(\omega; R) = \alpha_{ij}(\omega; R) - 2\alpha_{\text{atom}}(\omega)$, where $\alpha_{ij}(\omega)$ are tensor components of the total molecular polarizability and $\alpha_{\text{atom}}(\omega)$ is the atomic polarizability at frequency ω. The interaction-induced polarizability is the molecular contribution due to interactions between the nuclei, and becomes dominant for more deeply bound vibrational states in the potential. Since we are working only with isotropic $J = 0$ states, we take the trace

polarizability $\alpha^{\rm int}(\omega;R) = [\alpha^{\rm int}_{zz}(\omega;R) + 2\alpha^{\rm int}_{xx}(\omega;R)]/3$ [157, 205]. We extend the model for large R using a fitted long-range form $\alpha^{\rm int}(\omega;R) \sim A_6(\omega)R^{-6} + A_8(\omega)R^{-8} + A_{10}(\omega)R^{-10}$ [206]. Figure 3.14 shows the isotropic component $\alpha^{\rm int}(\omega;R)$ at 1.95 μm as a function of R.

In the second step, we calculate the polarizability of each vibrational level v by averaging the electronic polarizability $\alpha^{\rm int}(R)$ over the level's vibrational wavefunction $\Psi_v(R)$:

$$\alpha^{\rm int}_v(\omega) = \int_0^\infty |\Psi_v(R)|^2\, \alpha^{\rm int}(\omega;R) dR \tag{3.20}$$

where the differential polarizability for a transition $v \leftrightarrow v'$ is

$$\Delta\alpha_{v\leftrightarrow v'}(\omega) = \alpha^{\rm int}_{v'}(\omega) - \alpha^{\rm int}_v(\omega). \tag{3.21}$$

We obtain the vibrational wavefunctions by solving the Schrödinger equation, $[-(\hbar^2/2\mu)(d^2/dR^2)+ V(R)]\Psi_v(R) = E_v\Psi_v(R)$, using a discrete variable representation (DVR) [207, 208]. We use an empirical molecular potential $V(R)$ [209]; the reduced mass μ equals half the mass of a Sr atom. The uncertainties of the potential curve are negligible for our purposes (Supplemental Material). Figure 3.12 shows calculated differential dc and ac polarizabilities for $v \leftrightarrow 62$ transitions. It should be noted that this approach is valid only when the adiabaticity condition is maintained, that is, that the ground-state potential does not cross any of the excited-state potentials if shifted upwards by the energy of the incident photon. In Sr_2, this limits the photon wavenumber to about 8000 cm^{-1} (1.25 μm). Both our 1.95-μm (5128-cm^{-1}) laser and the room-temperature BBR spectrum are well within this margin.

Table 3.2: Bound states of the $^{88}Sr_2$ molecule investigated in this work. The initial molecular state is always the rotationless near-threshold $v' = 62$ level. Here v denotes the vibrational quantum number of the target bound state in the electronic $^1S_0$+$^1S_0$ 0_g^+ ground state and λ_{magic} is the magic wavelength. The differential polarizabilities are expressed in atomic units of $e^2a_0^2/E_h$, where e is the electron charge, a_0 is the Bohr radius and E_h is the Hartree energy [210]. The error bars on theoretical polarizabilities stem from comparison to experiment.

Clock transitions				Differential polarizability $\alpha_{v\leftrightarrow v'}(\omega)$ (a.u.)				
$X\,0_g^+$ $v \leftrightarrow v'$	v''	$f_{v\leftrightarrow v'}$ (MHz)	$\tilde{R}_v$ (a.u.)	λ_{magic} (nm)	Exp. (1.95 µm)	Th. (1.95 µm)	Th. (dc)	$\Delta f_{v\leftrightarrow v'}$ (Hz)
$61 \leftrightarrow 62$	15	1263.673 58(20) [211]	43.6	–	−0.41(0.52)	−0.1326(35)	−0.1080(28)	$+9.32(25)\times10^{-4}$
$55 \leftrightarrow 62$	15	108 214.221(10)	21.6	–	−3.68(0.38)	−2.985(78)	−2.429(63)	+0.020 99(56)
$41 \leftrightarrow 62$	11	2 177 876.735(81)	13.6	996.4379(10)	−21.67(0.88)	−19.10(50)	−15.60(41)	+0.134 9(37)
$27 \leftrightarrow 62$	11	8 075 406.280(18)	11.1	1006.5787(10)	−40.4(1.8)	−39.3(1.0)	−31.99(84)	+0.276 8(75)
$12 \leftrightarrow 62$	16	19 176 451.651(35)	9.62	1007.7634(10)	−60.1(4.0)	−61.3(1.6)	−49.7(1.3)	+0.430(12)
$7 \leftrightarrow 62$	15	24 031 492.422(24)	9.27	1007.1334(10)	−66.0(2.5)	−68.3(1.8)	−55.1(1.4)	+0.477(13)
$1 \leftrightarrow 62$	11	30 640 159.753(75)	8.91	1016.9714(10)	−75.7(3.3)	−76.0(2.0)	−61.1(1.6)	+0.529(15)
$0 \leftrightarrow 62$	11	31 825 183.207 5928(51) [154]	8.86	1004.7720(10)	−76.4(3.6)	−77.2(2.0)	−62.1(1.7)	+0.538(15)

We first validate the *ab initio* model using polarizabilities of the ground-state Sr atom. At dc we find a polarizability of +197.327 a.u., in excellent agreement with the state-of-the-art semi-empirical value of +197.14(20) a.u. [212]. Similarly, our ac polarizability of +207.524 a.u. at 1.95 µm agrees perfectly with the value of +208.2(1.1) a.u. [199].

Uncertainty of the theoretical polarizabilities due to empirical potential

To calculate the blackbody radiation shifts we needed the vibrational wavefunctions for all nonrotating vibrational states of strontium molecules in their electronic ground state. These were obtained by solving the radial Schrödinger equation using an accurate potential obtained empirically from Fourier transform spectroscopy [209]. The potential was provided in two versions: one in terms of a piecewise function and as a Morse/Long-Range (MLR) fit [213]. We used the latter.

We estimated the uncertainty of the theoretical model by comparing theoretical ac polarizabilities to experimental data and concluded that model is accurate to within 2.6%. We expect that most of this error bar is coming from the combination of the limited accuracy of the *ab initio* polarizabilities and the experimental accuracy. Here, we additionally look at the uncertainty of the theoretical model stemming from the use of an empirical potential [209]. To estimate the sensitivity of the theoretical polarizabilities to the experimental uncertainty we vary three of the most

important parameters of the potential – dissociation energy D_e, equilibrium distance R_e and the leading van der Waals coefficient C_6 and rerun our calculation. The parameters $R_e = 4.6720(1)$ and $D_e = 1081.64(2)\,\mathrm{cm}^{-1}$ [209] are varied within their stated experimental uncertainties whereas C_6 was varied such that the (well known) position of the near-threshold $v = 62$ bound state at -137 MHz shifted by at most 1 MHz.

The contributions due to D_e, R_e and C_6 are shown in Fig. 3.13. The variation of each parameter influences the predicted polarizabilities in a distinct manner. As the polarizability depends chiefly on the mean internuclear distance of a given vibrational level, scaling the potential depth D_e, for example, has little influence on the polarizability of deeply bound states. On the other hand, these states are naturally more sensitive to varying the equilibrium distance R_e. Lastly, weakly bound states are the most sensitive to the variation of the long-range van der Waals interaction coefficient, C_6. Nevertheless, we find that all of these error contributions are at least one order of magnitude smaller than the uncertainty we assigned to the model via direct measurements of ac Stark shifts and for our purposes are negligible.

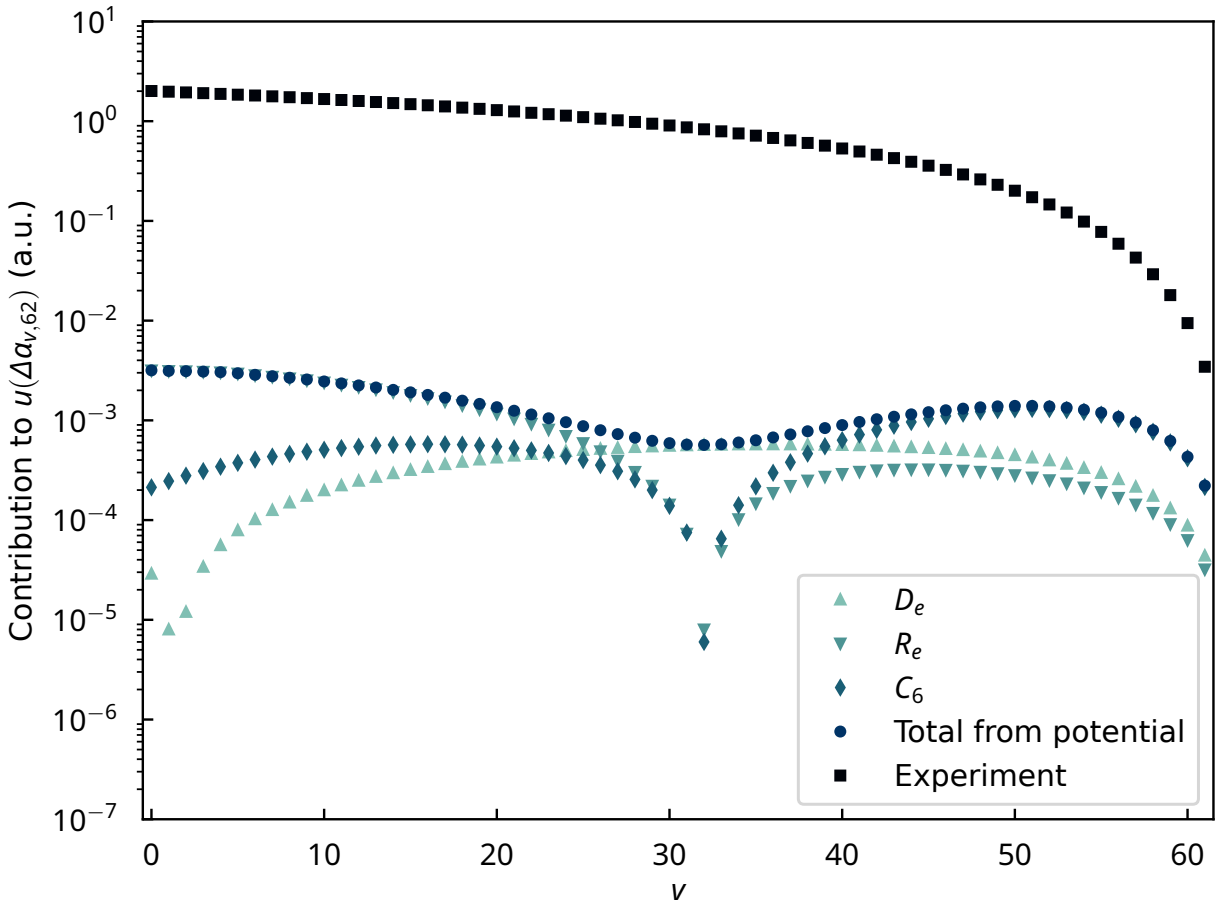

Figure 3.13: Contributions to the uncertainty of the theoretical polarizabilities due to the use of empirical potential from Ref. [209]. For all investigated transitions the contributions are all at least one order (typically more than two) of magnitude smaller than the error bar assigned to our theoretical model through comparison with experiment.

3.2.3 Application to BBR

In order to determine the BBR shift, we rely on good agreement between our experimental measurement and *ab initio* theory at 1.95 μm. The differential polarizability decreases monotonically as we go to more weakly bound target states [Fig.3.14]. We can describe this using the R-centroid approximation [214] and the concept of a LeRoy radius R_{LR} [215, 216]. The LeRoy radius approximates the boundary between two regimes. Below it, quantum mechanical terms dominate the interactions between the particles. Above it, classical interactions dominate. It is defined as $R_{LR} = 2(r_A + r_B)$, where $r_A = r_B = 4.15\ a_0$ are the charge radii of the two atoms [217]. Within the R-centroid approximation, the interaction-induced polarizability at the mean internuclear distance $\tilde{R}_v$ of state v can be extracted from the differential polarizability of the $v \leftrightarrow 62$ transition:

$$\alpha^{\mathrm{int}}(\omega; \tilde{R}_v) \approx -\Delta\alpha_{v\leftrightarrow 62}(\omega), \tag{3.22}$$

where $\tilde{R}_v = \int_0^\infty |\Psi_v(R)|^2\, R dR$. This formula neglects the small interaction-induced polarizability of the $v' = 62$ state. Thus, different vibrational transitions effectively serve as probes of polarizabilities, each at a different internuclear separation (Figure 3.14).

Our measured transitions then probe polarizabilities over a range of 8.86 a_0 (roughly the equilibrium distance R_e) to 43.6 a_0. The LeRoy radius $R_{LR} = 16.6\ a_0$, and beyond this distance, the interaction-induced polarizability becomes negligible, and we can think of Sr_2 as a "physicist's molecule" [218], where its polarizability is just that of two atoms. Below the LeRoy radius, the polarizability dramatically increases (up to 80 a.u.) due to the interaction-induced contribution, and it becomes more of a "chemist's molecule". By choosing different vibrational levels, we can sample a range of interaction-induced polarizabilities, probing distinct molecular properties.

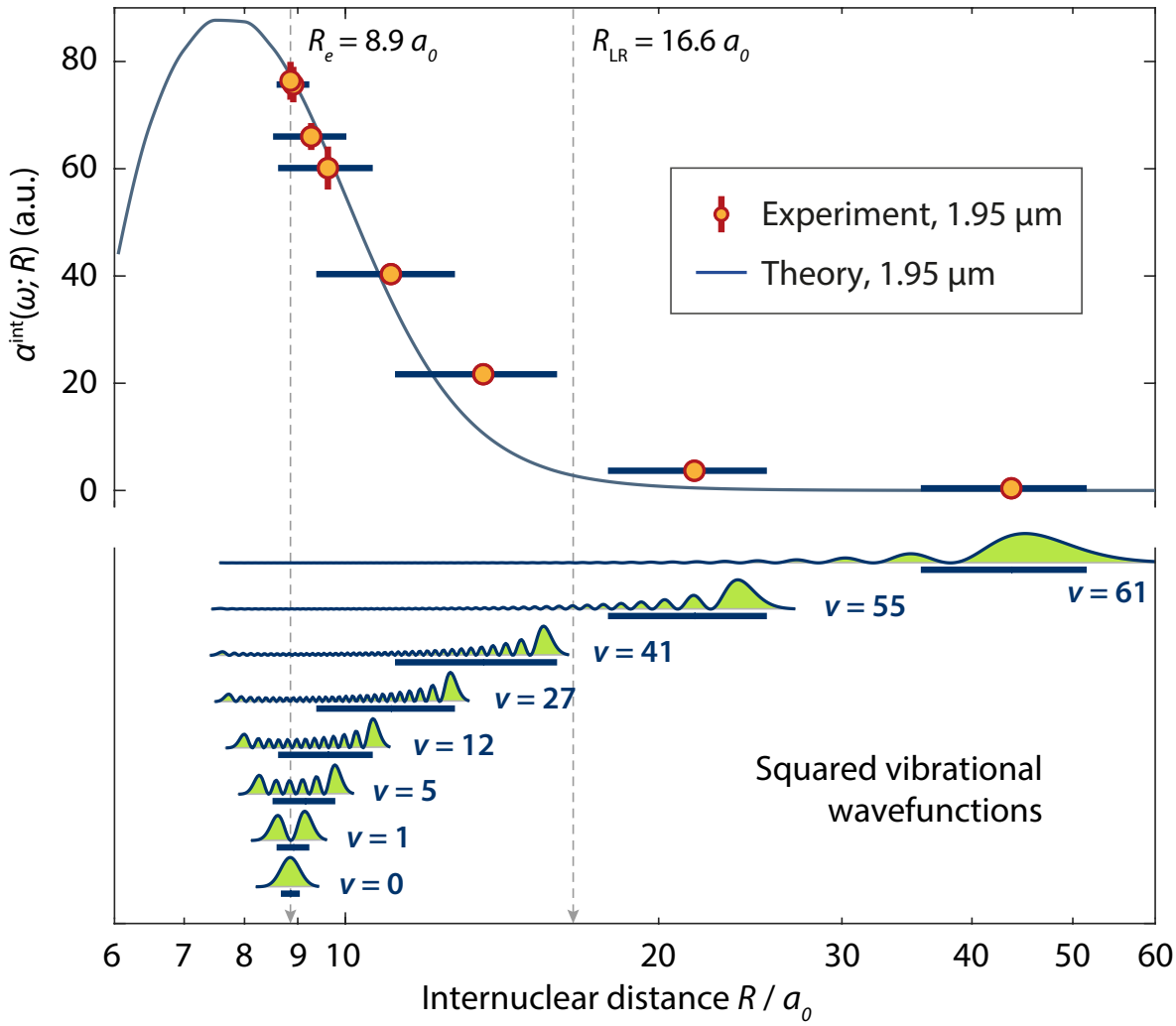

Figure 3.14: Interaction-induced ac polarizability at $\lambda = 1.95\,\mu$m. In addition to the *ab initio* result we show absolute experimental polarizabilities in relation to mean internuclear distances $\tilde{R}$ (Table 3.2). Horizontal bars indicate the range $[\tilde{R}_v - S_{R_v}, \tilde{R}_v + S_{R_v}]$ of internuclear distances probed by the vibrational wavefunctions shown in the lower panel. Here $\tilde{R}_v$ and S_{R_v} are the mean and standard deviation internuclear distances for wavefunction squared treated as a probability distribution. R_e and R_{LR} are, respectively, the equilibrium distance and the LeRoy radius [215, 216].

We can estimate the uncertainty of our theoretical model by allowing a free scaling parameter in a fit to the experimental data and checking whether the best-fit scaling is significant. We perform a least-squares fit to our data, and obtain a best-fit scaling of +1.8(2.4)%. Since this is within error, we determine that scaling is not necessary. In fact, the reduced chi-square for the scaled model χ^2/d.o.f= 1.78 is worse than for the unscaled model χ^2/d.o.f= 1.69. This justifies not scaling, as well as using the theoretical model for other infrared wavelengths. Nevertheless, out of caution we combine the 2.4% uncertainty from the scaling factor with an additional 1.8% possible systematic error to obtain a "Type B" uncertainty [219] of 2.6%.

BBR Shift Calculation

Finally, we calculate the BBR shift $\Delta f_{v\leftrightarrow v'}$ by expressing it as an ac Stark shift integrated over the BBR spectrum [220–222]:

$$\Delta f_{v\leftrightarrow v'} = -\frac{1}{2h}\int_0^\infty \frac{4\pi}{\epsilon_0 c} B_\omega(T)\Delta\alpha_{v\leftrightarrow v'}(\omega)d\omega, \tag{3.23}$$

where the spectral radiance of the BBR field at temperature T is

$$B_\omega(T) = \frac{\hbar\omega^3}{4\pi^3c^2}\frac{1}{\exp(\hbar\omega/k_BT)-1}. \tag{3.24}$$

Typically, BBR shifts for atomic clocks are determined using a sum-over-states approach to calculate the static and dynamic terms [212, 220, 222–224], but here we already have computed the dynamic polarizabilities, so we can directly integrate the BBR shift.

The *ab initio* calculations produce polarizability as a function of R at discrete infrared wavelengths. In order to compute the BBR shift Eq. (3.23), we need the continuous polarizability as a function of photon frequency for each vibrational state. Since practically all of the BBR spectrum falls below any resonance frequencies in our system, we can do this by expanding the polarizability in terms of Cauchy coefficients [223]: $\Delta\alpha_{v\leftrightarrow v'}(\omega) = \Delta\alpha^{(0)}_{v\leftrightarrow v'} + \Delta\alpha^{(2)}_{v\leftrightarrow v'}\omega^2 + \Delta\alpha^{(4)}_{v\leftrightarrow v'}\omega^4 + \ldots$ that we fit to tenth order to numerically calculated polarizabilities [Fig. 3.15(a)]. This allows us to express

the BBR shift as a series:

$$\Delta f_{v\leftrightarrow v'} = \sum_{n=0,2,\ldots} \Delta f_v^{(n)} = \sum_{n=0,2,\ldots} -\frac{c_n \Delta\alpha^{(n)}_{v\leftrightarrow v'}}{4\pi^3\epsilon_0 c^3}\left(\frac{k_B T}{\hbar}\right)^{4+n}, \tag{3.25}$$

where the Planck integrals $c_n = \int_0^\infty u^{3+n}/(e^u - 1)du$ are given in Table 3.3. The leading term is the well known static contribution to the BBR shift [212, 221], while further terms constitute a dynamic correction η on the order of 0.5–0.6 % (Table 3.3). Here terms beyond the second order are negligible.

Our calculation of the blackbody radiation shift relies on expanding the differential polarizability of a transition in terms of a series of Cauchy coefficients. Averaging each contribution to the polarizability over the Planck distribution involves calculating integrals of the following type:

$$c_n = \int_0^\infty \frac{u^{3+n}}{\exp(u) - 1} du = \mathrm{Li}_{n+4}(1)\Gamma(n+4) \tag{3.26}$$

for even n. Here $\mathrm{Li}_s(z)$ is the polylogarithm function of order s,

$$\mathrm{Li}_s(z) = \sum_{k=1}^{\infty} \frac{z^k}{k^s}, \tag{3.27}$$

and $\Gamma(x)$ is Euler's gamma function. While for our purposes it was enough to cut the series off at $n = 4$, in the future, higher orders might be needed. For future reference, here we list the first eight

Table 3.3: Contributions to the BBR shift at 300 K for the $0 \leftrightarrow 1$ and $0 \leftrightarrow 62$ transitions.

n	c_n	$\Delta f^{(n)}_{0\leftrightarrow 1}$ (Hz)	$\Delta f^{(n)}_{0\leftrightarrow 1}/f_{0\leftrightarrow 1}$	$\Delta f^{(n)}_{0\leftrightarrow 62}$ (Hz)	$\Delta f^{(n)}_{0\leftrightarrow 62}/f_{0\leftrightarrow 62}$
0	$\pi^4/15$	$+0.0081$	$+6.8\times10^{-15}$	$+0.53$	$+1.7\times10^{-14}$
2	$8\pi^6/63$	$+6.1\times10^{-5}$	$+5.1\times10^{-17}$	$+0.0033$	$+1.0\times10^{-16}$
4	$8\pi^8/15$	$+6.5\times10^{-7}$	$+5.5\times10^{-19}$	$+6.3\times10^{-5}$	$+2.0\times10^{-18}$
η (%)		0.54		0.62	

integrals:

$$
\begin{aligned}
c_0 &= \frac{\pi^4}{15} \approx 6.49393940226683\ldots \\
c_2 &= \frac{8\pi^6}{63} \approx 122.081167438134\ldots \\
c_4 &= \frac{8\pi^8}{15} \approx 5060.54987523764\ldots \\
c_6 &= \frac{128\pi^{10}}{33} \approx 363240.911422383\ldots \\
c_8 &= \frac{176896\pi^{12}}{4095} \approx 39926622.9877311\ldots \\
c_{10} &= \frac{2048\pi^{14}}{3} \approx 6227402193.41097\ldots \\
c_{12} &= \frac{3703808\pi^{16}}{255} \approx 1307694352218.91\ldots \\
c_{14} &= \frac{1437433856\pi^{18}}{3591} \approx 355688785859224\,. \qquad (3.28)
\end{aligned}
$$

The molecular clock, based on a vibrational transition in the ground-state potential of Sr_2, can in principle use any pair of vibrational states as clock states. Using a more deeply bound vibrational state would involve coherently transferring the population from a weakly bound state via STIRAP [163]. In Fig. 3.15(b), we plot the BBR shift for $v \leftrightarrow 62$ transitions, $\Delta f_{v\leftrightarrow 62}$ (red line). For our previously measured clock transition [154] $\Delta f_{0\leftrightarrow 62} = +538(15)$ mHz, which leads to a BBR contribution to fractional uncertainty of $u(\Delta f_{v\leftrightarrow v'})/f_{v\leftrightarrow v'} = 4.7\times10^{-16}$. We further find that the BBR contribution to fractional uncertainty of the molecular clock transition can be reduced by strategically selecting $0 \leftrightarrow v'$ clock transitions (blue line) between deeply bound vibrational states [Fig. 3.15(c)]. This configuration could allow fractional uncertainties as low as 1.8×10^{-16}, a factor of ~2.5 lower than the $0 \leftrightarrow 62$ transition. This technique has the tradeoff of having a smaller transition frequency, with several possible benefits.

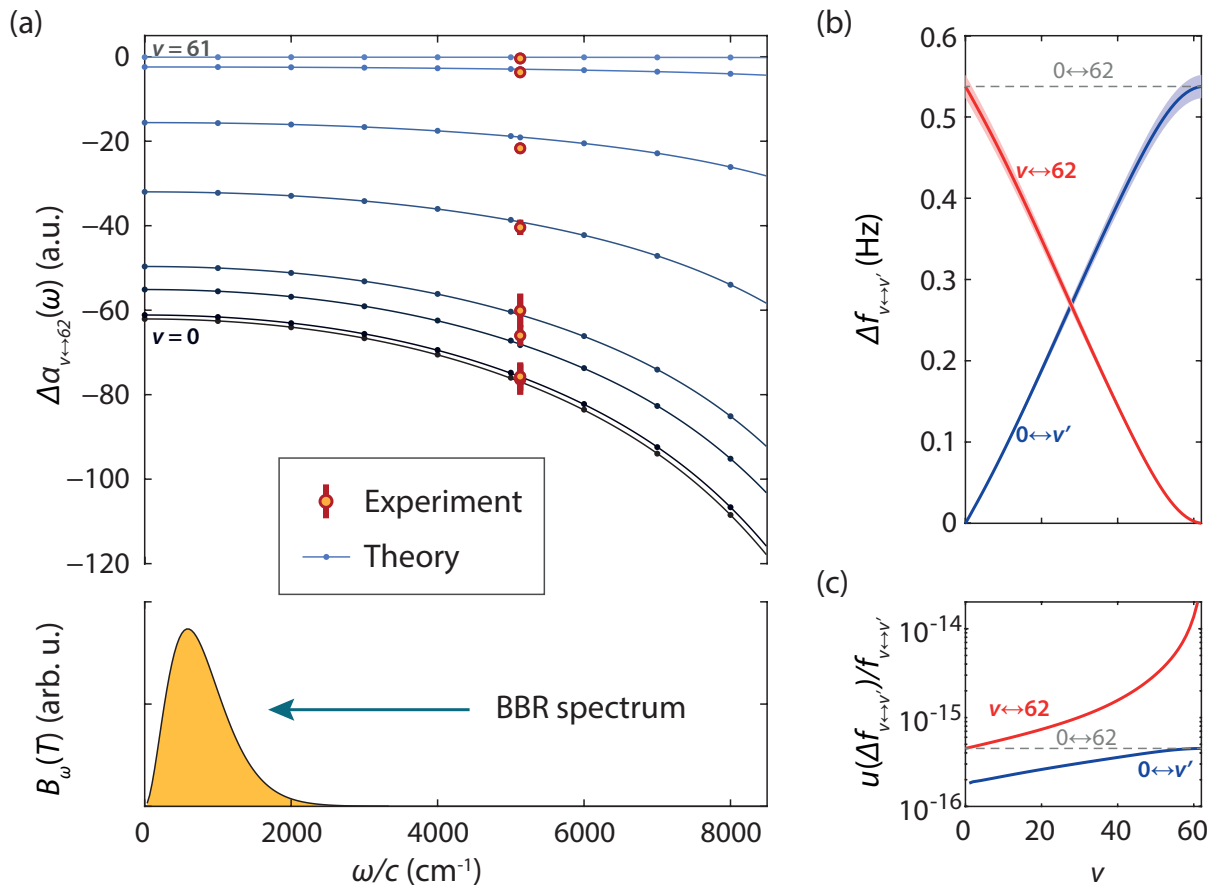

Figure 3.15: (a) Differential polarizabilities for the selected clock transitions. Below, a plot of a BBR spectral radiance $B_\omega(T)$ at 300 K. (b) Absolute BBR shift for $0 \leftrightarrow v'$ clock transitions. (c) Relative BBR uncertainty for the same clock configurations.

BBR summary

We have determined the BBR shift for our strontium molecular lattice clock to the level of 10^{-16}. We have done so by leveraging agreement between experimental Stark shift measurements of clock transitions at 1.95 μm, and *ab initio* calculations of the electronic polarizability of the strontium dimer. Based on this agreement, we extend the theoretical polarizability method to other infrared frequencies. We expand polarizability using a Cauchy coefficient expansion, and then integrate the calculated polarizability over the BBR spectrum range. We extend this technique to other potential clock state pairs. This calculation paves the way to improvement of the molecular clock to the 10^{-16} level.

3.3 Clock outlook and improvements

There remains a clear path toward improved metrology with the Sr_2 molecular clock. Efforts to build a second-generation molecular clock are underway, which will implement an in-vacuum cavity, and orient the lattice in the vertical direction, rather than horizontal. Both of these upgrades are geared towards improving the clock coherence time. In the horizontal lattice, our minimum operational trap depth is limited because lowering the lattice power dramatically decreases MOT-to-lattice transfer efficiency. In the future, we could trap atoms at high intensity and then ramping down to lower intensity for the clock probe pulse. This would reduce the lattice-induced scattering that limits our $v = 0$ clock-state lifetime. Additionally, as we progress towards lower intensities, tunneling creates Doppler broadening that limits the accessible clock linewidths. Switching to a vertical orientation tilts the lattice potential under gravity, creating a Wannier-Stark ladder that lifts the degeneracy between adjacent trap sites and suppresses tunneling [225]. Additionally, supporting atoms against gravity with the tighter axial confinement allows operation at even lower lattice intensities.

The cavity implementation allows us to significantly increase the beam waist size, and therefore lattice trapping volume, while still maintaining high intensity due to the buildup. This will allow us to use lower densities, while still having high absolute number. The larger beam waist and cavity creates a more homogeneous beam profile, which could also reduce the inhomogeneous broadening from the lattice. Additionally, one could imagine using a blue-detuned optical trap, where the molecules are trapped at an intensity anti-node rather than a node, so that the lattice intensity would be at a minimum. This would greatly reduce the lattice scattering. With the cavity, we can lock to the Laguerre-Gaussian 01 “donut" mode, which provides the necessary radial confinement. Some groups distribute the sample over more lattice sites using excited-band delocalization [226], allowing a larger total number while reducing per-site density. A further improvement could be implementation of a 3D lattice or optical tweezers, enabling single-site occupancy at high molecule number and eliminating collisional loss.

In order to improve the absolute frequency metrology, we plan to upgrade the local timebase as well. Currently, we use a commercial rubidium clock which has a restrictive precision of $\sim 10^{-12}$. When it is steered by the GPS signal, it also has large jumps on the order of 10^{-12}, which disrupt clock operation. A cesium clock or hydrogen maser would offer better frequency precision, removing the local timebase as a limiting factor in our absolute frequency measurement. Additionally, we could implement two-way time transfer, which involves exchanging timing information between our GPS receiver and the GPS reference at NIST [227]. This allows improved determination of absolute position for absolute frequency measurement.

We have several ideas for improving overall stability. First, the downleg laser was previously a homemade external cavity diode laser (ECDL), which experienced stability issues, especially with regards to locking to the comb. We replaced this with a Toptica DLPro laser, which has much better frequency stability and a larger mode-hop free range. We also hope to explore alternative solutions to improve comb phase-locking stability. This includes detecting the beat note with a balanced photodetector rather than a single photodiode, an approach that has shown success in reducing phase-lock instability [228]. Additionally, we observed day-to-day fluctuations in the probe lightshift caused by beam pointing instability. In future iterations, we could calibrate the probe intensity daily using Autler-Townes spectroscopy.

In the future, we could improve the BBR systematic uncertainty by performing Stark-shift measurements with the full Hz-level clock precision, rather than the current kHz peak widths. Additionally, we could use a 10 μm CO_2 laser to measure the Stark shift. This is close to the BBR wavelength, and would give us a more direct measurement of the BBR shift. We could also implement different clock schemes for the reduction of lattice scattering. For example, we could change clock states such that both clock states are deeply bound vibrational states. This would require population initialization via STIRAP but would give access to clock-state pairs with closer baseline polarizabilities. This would allow larger magic detunings, reducing lattice scattering to the $1u$ state. Deeply bound vibrational states have spacings of $\sim$ 1 THz, whereas weakly bound states can be separated by hundreds of MHz, so selecting a transition between two deeply bound

states, such as $v = 0 \leftrightarrow v = 20$, would preserve a large clock frequency ($\sim$ 19 THz) while allowing much larger magic detunings thanks to the closer baseline polarizabilities.

Currently, we only use $J = 0$ states for clock states. In the future, one could envision instead using one or both $J = 2$ states. In this case, we could implement a polarization-aided magic condition, a technique demonstrated by other groups [229]. The total trap potential is:

$$U = -\frac{\mathcal{E}_0^2}{4}\left(\alpha_{\mathrm{sc}} - \alpha_{\mathrm{vec}}\frac{M}{2J}\, i(\boldsymbol{\epsilon}^* \times \boldsymbol{\epsilon}) \cdot \hat{\mathbf{q}} + \alpha_{\mathrm{tns}}\frac{3M^2 - J(J+1)}{J(2J-1)}\frac{3|\boldsymbol{\epsilon} \cdot \hat{\mathbf{q}}|^2 - 1}{2}\right). \tag{3.29}$$

The laser polarization vector is:

$$\boldsymbol{\epsilon} = \hat{\mathbf{Z}}\cos\theta + \hat{\mathbf{X}}e^{i\phi}\sin\theta, \tag{3.30}$$

The scalar, vector, and tensor polarizabilities are[158, 230]:

$$\alpha_{\mathrm{sc}} = \frac{1}{\hbar}\frac{1}{3(2J+1)}\sum_f |\langle f||d^{(1)}||i\rangle|^2 \frac{2\omega_{fi}}{\omega_{fi}^2 - \omega^2}, \tag{3.31}$$

$$\alpha_{\mathrm{vec}} = -\frac{1}{\hbar}\sqrt{\frac{6J}{(2J+1)(J+1)}}\sum_f (-1)^{J+J'}\begin{Bmatrix} 1 & 1 & 1 \\ J & J' & J \end{Bmatrix}|\langle f||d^{(1)}||i\rangle|^2 \frac{2\omega}{\omega_{fi}^2 - \omega^2}, \tag{3.32}$$

$$\alpha_{\mathrm{tns}} = \frac{1}{\hbar}\sqrt{\frac{10J(2J-1)}{3(2J+1)(J+1)(2J+3)}}\sum_f (-1)^{J+J'}\begin{Bmatrix} 1 & 2 & 1 \\ J & J' & J \end{Bmatrix}|\langle f||d^{(1)}||i\rangle|^2 \frac{2\omega_{fi}}{\omega_{fi}^2 - \omega^2}. \tag{3.33}$$

One can imagine tuning the vector and tensor polarizability terms in Eqn. 3.29, to create a polarizability crossing between two states that is at a much larger magic detuning. This would also increase the scattering lifetime.

A further exciting direction is to create a heteronuclear combination of bosonic isotopes, such as ^{86}Sr-^{88}Sr. For the homonuclear combinations, direct transitions between vibrational states in the ground-state potential are forbidden by selection rules. In a heteronuclear molecule, this transition

is weakly allowed because the nuclei can exchange positions. This enables a clock based on a direct ground-state vibrational transition, a true THz frequency standard with possible frequencies from 100 MHz to 30 THz. In this case, the one-photon resonant probe lightshift would be greatly reduced, but the potential systematic shift due to DC, or near DC electric fields such as BBR could be increased. Groups have successfully locked lasers around this $\sim$ 30 THz frequency range to frequency combs [231], so the technology exists to make this possible.

Chapter 4: Weakly bound $^{86}Sr_2$ molecules

Building on our work with $^{88}Sr_2$ molecules, which characterized the full ground-state vibrational structure and precisely measured a clock transition, we now extend these techniques to $^{86}Sr_2$. Precision measurement of the same clock transition in $^{86}Sr_2$, along with good agreement with *ab initio* data, can place novel constraints on mass-dependent Yukawa forces at the nm scale [232]. $^{86}Sr_2$ is especially interesting for its weakly bound halo state, with a binding energy of just $\sim$ 83 kHz, more than three orders of magnitude smaller than the $\sim$ 137 MHz binding of the most weakly bound state in $^{88}Sr_2$. This shallow binding gives the halo state an exceptionally large spatial extent and makes it highly sensitive to small changes in the interatomic interaction. It is particularly sensitive to long-range quantum electrodynamics (QED) effects, including the Casimir–Polder interaction [233–237]. The halo state is also of interest for studies of Efimov physics [238, 239] and for the tuning of interparticle interactions via optical Feshbach resonances [240, 241]. Whereas halo molecules are usually produced via magnetic Feshbach resonances [81], the $^{86}Sr_2$ halo is free of the hyperfine structure that complicates bialkali systems, simplifying *ab initio* quantum chemistry treatments of the interactions. Other field-free halo molecules have been produced, including Ca_2 [242] and He_2 [243–245], but both are more deeply bound by orders of magnitude, with correspondingly smaller spatial extents. The large spatial extent of the halo state is directly tied to its scattering length a, which for a weakly bound near-threshold state is [246]

$$a \approx \bar{a} + \frac{\hbar}{\sqrt{2\mu E_b}}, \tag{4.1}$$

where the mean (background) scattering length is

$$\bar{a} = \frac{\Gamma(3/4)}{2\Gamma(5/4)}\left(\frac{2\mu C_6}{\hbar^2}\right)^{\frac{1}{4}}, \tag{4.2}$$

Here μ the molecular reduced mass, E_b the binding energy, and C_6 is the leading van der Waals coefficient.

Although photoassociative spectroscopy of atomic ^{86}Sr has determined molecular binding energies [235, 247], stable samples of $^{86}Sr_2$ molecules have not previously been produced. Here, we report the first such samples. We first produce ^{86}Sr atomic samples and demonstrate interleaved loading of ^{88}Sr and ^{86}Sr MOTs on alternating experimental cycles. After transferring atoms into the optical lattice, we perform two-photon Autler-Townes photoassociative spectroscopy to measure transition strengths to potential initial states. Guided by these measurements, we drive one-photon photoassociation into weakly bound excited states and allow spontaneous decay to populate weakly bound levels of the ground-state potential. To probe the long-range portion of the ground-state potential alongside the halo state, we measure the two weakly bound vibrational splittings, $v = -1 \leftrightarrow v = -2$ and $v = -2 \leftrightarrow v = -3$. After evaluating the dominant systematics, lattice and probe-laser Stark shifts, we determine the vibrational splittings to sub-100 Hz precision. These measurements, combined with the previously reported halo-state binding energy [235], will inform ongoing quantum chemistry calculations of the long-range potential.

4.1 ^{86}Sr atomic sample preparation

4.1.1 Isotope switching

Toward our ultimate goal of an Sr_2 isotope-shift measurement, we must first trap ^{86}Sr atoms in the two-stage $^1S_0$–$^1P_1$ and $^1S_0$–$^3P_1$ MOTs. Switching from ^{88}Sr to ^{86}Sr requires accounting for the atomic isotope shifts of both transitions. These are -124.8 MHz for the $^1S_0$–$^1P_1$ transition and -163.81 MHz for the $^1S_0$–$^3P_1$ transition [248, 249]. These are easily addressable with acousto-optic modulators (AOMs). For the blue MOT we use a single-pass AOM together with a galvo mirror [Fig. 4.1(a)]. The choice of AOM configuration, single-pass vs. double-pass, was dictated by the available hardware bandwidth and deflection angles. The galvo mirror coaligns the AOM's (-1) order (used to address ^{86}Sr) with the zeroth order (used for ^{88}Sr). In order to switch between isotopes, the AOM is turned on/off and the galvo position is flipped. The red MOT is simpler:

a double-pass AOM toggles cleanly between the two isotope frequencies, requiring only a TTL signal [Fig. 4.1(b)]. The (0) order and the (-1) order retroreflect off separate mirrors, so their alignments are tuned independently.

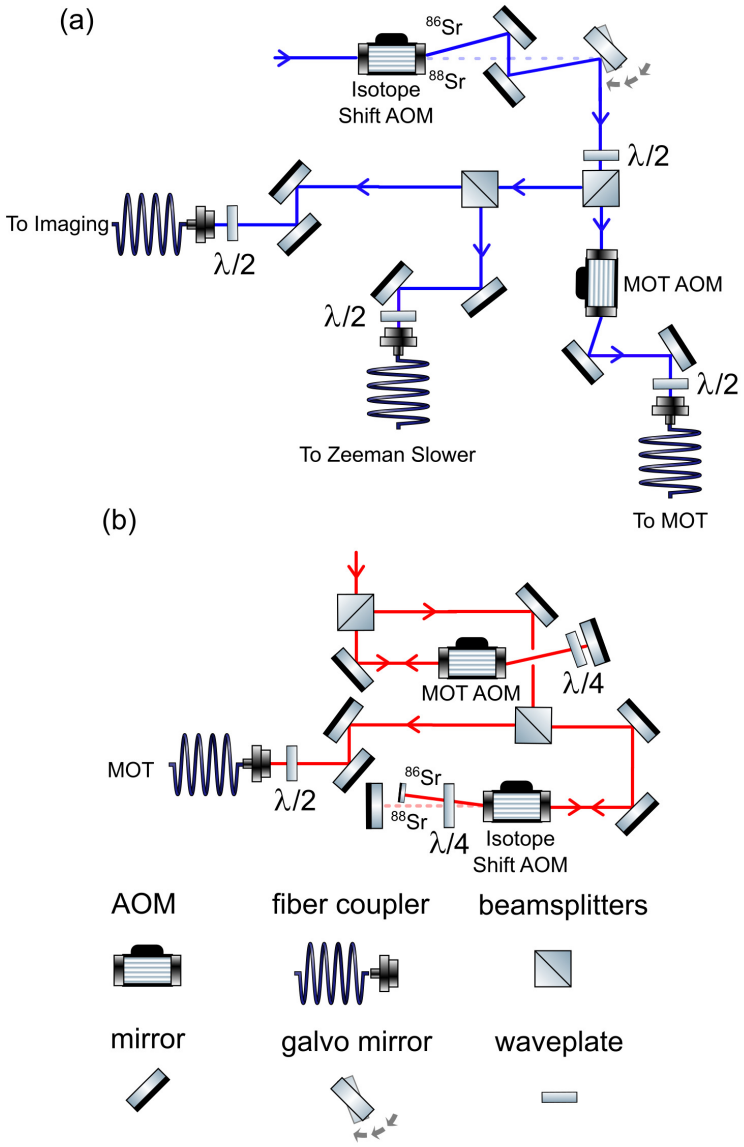

Figure 4.1: Configuration of AOMS to address the isotope shift between ^{86}Sr and ^{88}Sr. (a) Isotope shift setup for 461 nm $^1S_0$–$^1P_1$ blue MOT transition. (b) Isotope shift setup for 689 nm $^1S_0$–$^3P_1$ red MOT transition.

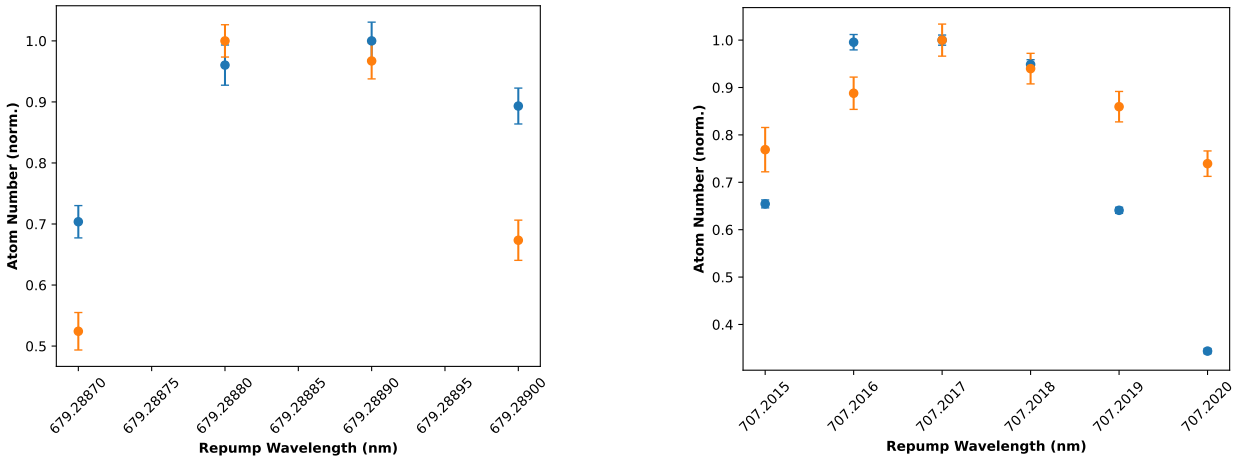

Figure 4.2: Dependence of atom number on repump wavelength for ^{86}Sr and ^{88}Sr. (a) Atom number dependence for the 679 nm repump transition. (b) Atom number dependence for the 707 nm transition.

In principle, the 679 nm and 707 nm repump lasers should also be retuned when switching species. To quantify the required shift, we measured the MOT atom number versus repump wavelength for both isotopes [Fig.4.2], and found only minor variation between them. This is convenient because our repumps are wavemeter-locked with a slow servo, making sub-second switching difficult. We therefore chose not to retune the repumps between isotopes.

A future isotope-shift measurement will require a direct comparison between the $^{86}Sr_2$ and $^{88}Sr_2$ clock transitions. One approach is to measure each isotope at different times and reference both to International Atomic Time (TAI). With our current rubidium timebase, however, the measurement precision would be limited by the absolute-frequency referencing. An alternative is to interleave the isotopes between cycle iterations. We demonstrated this by alternating blue-MOT loading between ^{86}Sr and ^{88}Sr on successive cycles [Fig.4.3]. This sets the stage for a possible interleaved clock measurement between $^{86}Sr_2$ and $^{88}Sr_2$. Further effort is required to optimize interleaved loading.

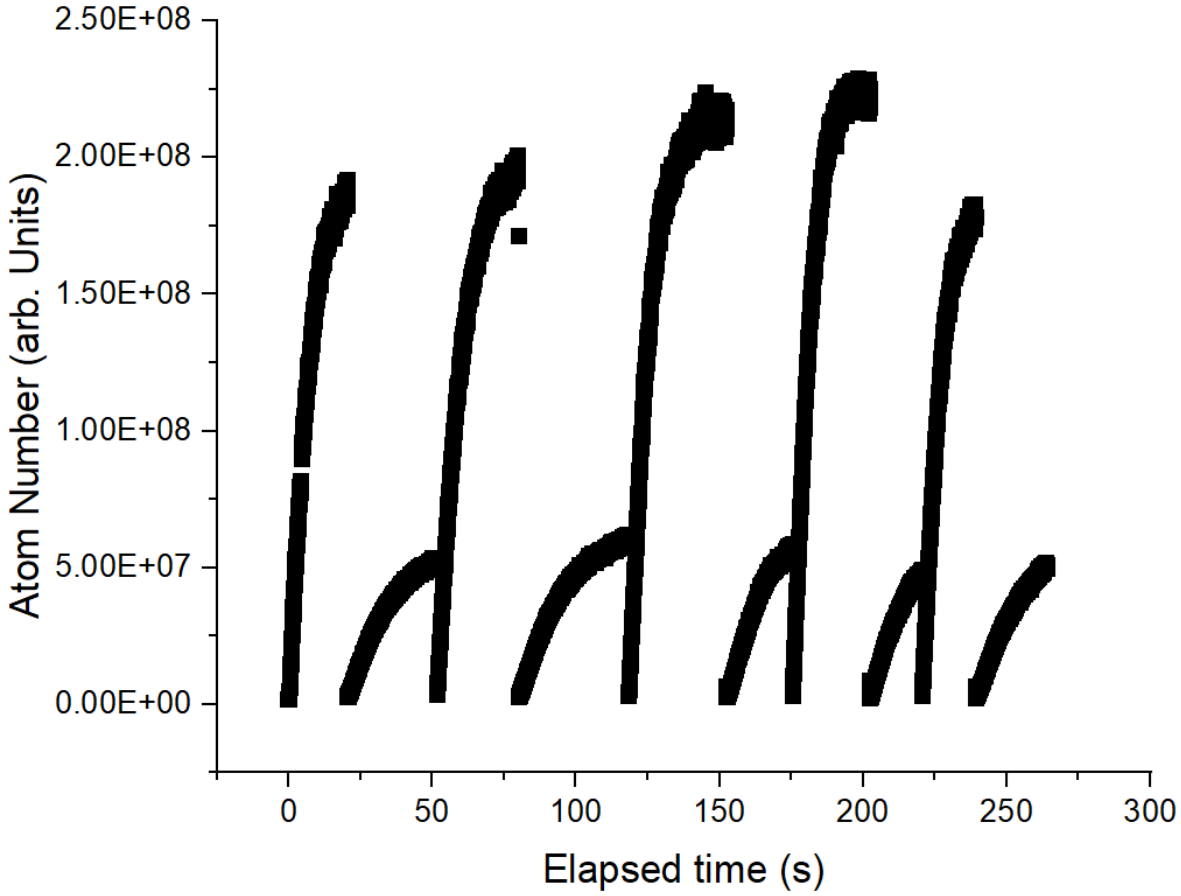

Figure 4.3: Interleaved loading of the $^1S_0-^1P_1$ MOT between ^{86}Sr and ^{88}Sr.

4.1.2 Characterization of atomic ^{86}Sr magneto-optical trap

We successfully transferred atoms to the red MOT and characterized its properties. We measure the temperature of the red MOT by varying the time-of-flight, and fitting the Gaussian width of the resulting absorption images [Fig.4.4]. We use typical ballistic thermal expansion:

$$\sigma = \sqrt{\sigma_0^2 + \frac{k_B T}{M} t^2} \tag{4.3}$$

where σ_0 is the initial width, T is the temperature, M is the atomic mass, and t is the expansion time. We obtain a typical temperature of $\sim 2.5\ \mu$K.

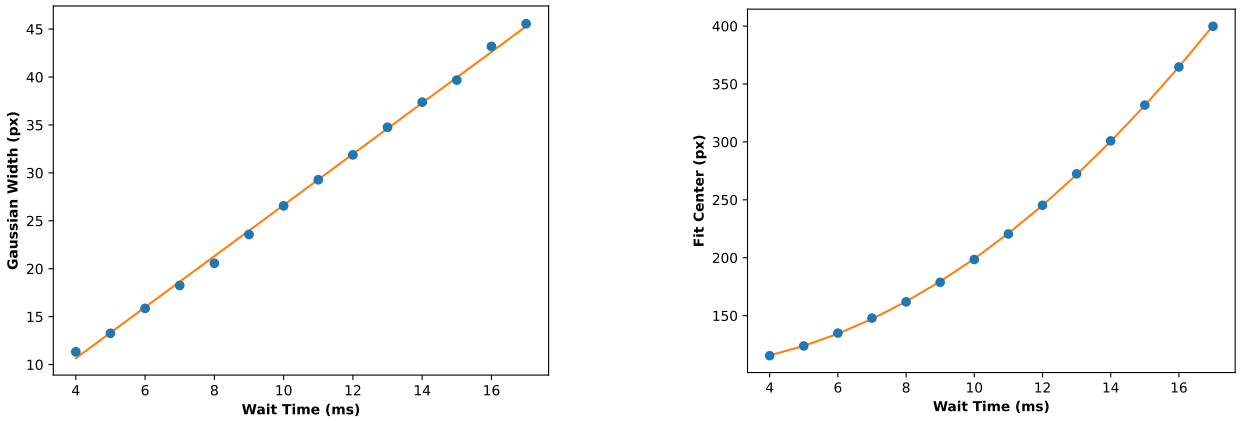

Figure 4.4: Time-of-flight of atoms in the red MOT. A 2D Gaussian is fit to each image. (a) The width of the Gaussian fit for the red MOT temperature versus expansion time. (b) Position of the center of the Gaussian fit in the vertical direction versus expansion time.

We determine the blue MOT atom number via fluorescence imaging, calibrated as follows. The camera is first calibrated by illuminating it with a beam of known optical power. For each pixel there is a maximum 255 value, and we need the conversion from counts to photons. We acquire an image of the calibration beam and fit a 2D Gaussian:

$$z_0 + A * exp\left(-\frac{1}{2}\left(\frac{x}{W_x}\right)^2 - \frac{1}{2}\left(\frac{y}{W_y}\right)^2\right) \tag{4.4}$$

Integrating over the fit yields the total pixel-count integral. Given the incident beam power P_{laser} and the exposure time T_{expo}, the total optical energy delivered is

$$E = P_{\text{laser}}\, T_{\text{expo}} \approx 3.57 \times 10^{-10}\text{J}, \tag{4.5}$$

which converts to photon number via $N_{\text{phot}} = \frac{E}{h\nu}$, giving the photons-per-count calibration. A fluorescence image of the MOT is then similarly fit to a 2D Gaussian. The integrated pixel counts, corrected for the collection solid angle, yield the total number of photons emitted during the exposure. Combined with the measured laser intensity, this determines the saturation parameter,

$$s = \frac{I}{I_{sat}} * \frac{1}{1 + (2\delta/\Gamma)^2} \tag{4.6}$$

which sets the per-atom fluorescence rate (phot/s/atom) and therefore gives the total atom number.

With this procedure, we estimate a blue-MOT atom number of $\sim 4 \times 10^7$ after 2 s of loading.

The red MOT atom number is measured by absorption imaging after sufficient time-of-flight to avoid saturation, with a 2D Gaussian fit to the column density. The absorption of the light by the cloud of atoms follows the Beer-Lambert law, and each image is converted to optical density,

$$OD \equiv \sigma_0 \, \rho_c$$

where σ_0 is the resonant absorption cross section and ρ_c is the column density. For the blue transition, $\sigma_0 = 1 \times 10^{-13} \mathrm{m}^2$. The fitting function used below is of the form $A \, \exp\left(-\frac{x^2}{2\,\Delta_x^2} - \frac{y^2}{2\,\Delta_y^2}\right) +$ offset. The amplitude is in raw (0-255) brightness units, converted to optical density by multiplying by $5.0/255$. Widths are in pixels, converted to meters via the imaging magnification.

Thus, using those units for A, Δ_x, Δ_y the integral of the Gaussian fit in terms of optical density is given by : $\sigma_0 \iint \rho_c \, dA = 2\pi A \, \Delta_x \, \Delta_y \times 2.245 \times 10^{-12}$ m^2 where $\int \int \rho_c$ is the atom number N_{at}.

Using this method, we measure a red MOT atom number of $\sim 5 \times 10^5$. Applying the same procedure after transferring atoms into the optical lattice, we observe a transfer efficiency of roughly 50%.

4.2 Production of weakly bound $^{86}Sr_2$ molecules

4.2.1 Photoassociative Autler-Townes spectroscopy for transition strength measurements

Our PA method involves one-photon excitation of ground state atoms into weakly bound vibrational states in the 0_u^+ or 1_u potential near the $^1S_0$-$^3P_1$ atomic threshold (Fig. 4.5(a)). The molecules then decay into weakly bound states of the ground-state electronic potential $X^1\Sigma_g^+$. The decay branching ratios are set by the relative transition strengths, which are proportional to the vibrational wavefunction overlap, known as the Franck-Condon factor. A near-unity Franck-Condon factor ensures efficient creation of molecules in a single vibrational state v of the ground state [85].

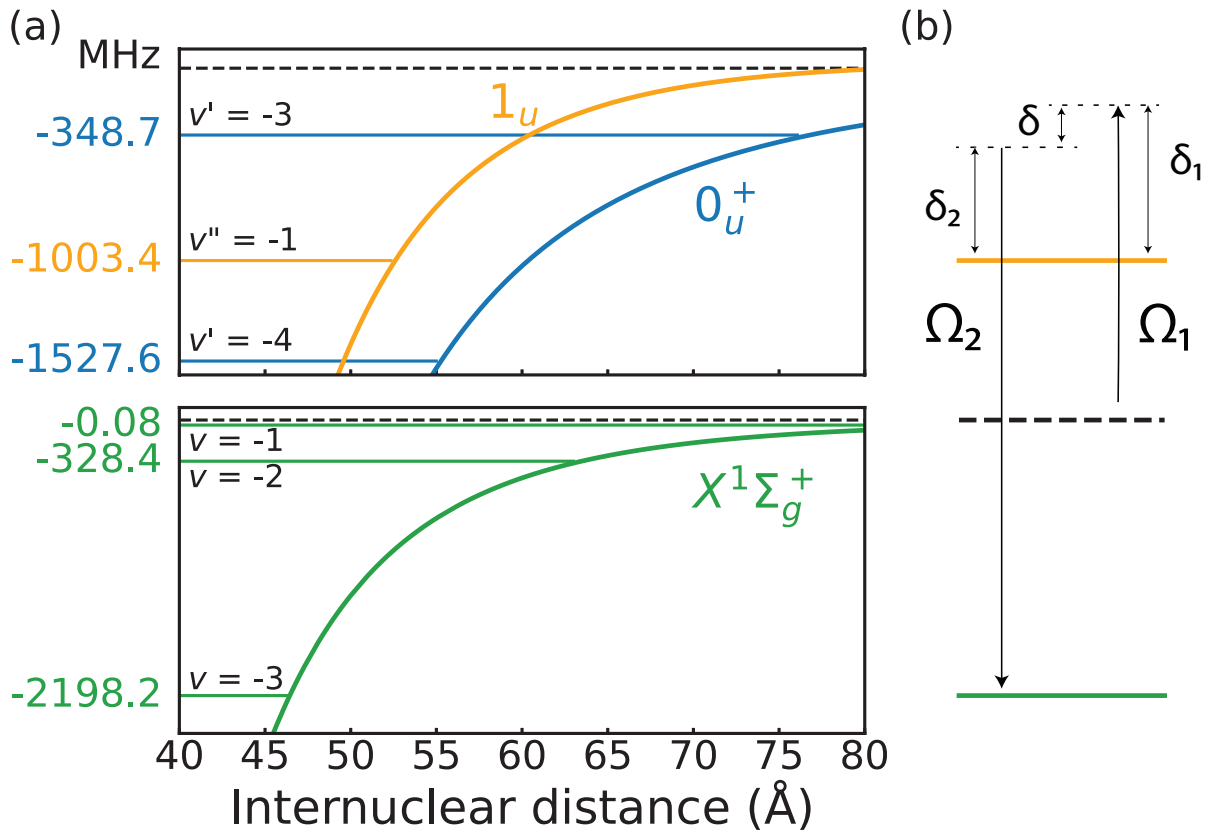

Figure 4.5: (a) The ground-state electronic potential $X^1\Sigma_g^+$ asymptotes to the $^1S_0$+$^1S_0$ atomic threshold, and the excited-state potentials 1_u and 0_u^+ asymptote to the $^1S_0$+$^3P_1$ intercombination threshold. The weakly bound vibrational states are displayed (v, v', and v'' for the three potentials, as labeled). (b) The Rabi frequency (Ω_1, Ω_2) and detuning (δ_1, δ_2, δ) scheme for photoassociative Autler-Townes spectroscopy.

To measure the transition strengths, we use photoassociative Autler-Townes spectroscopy. In this two-photon process, the pump laser (Rabi frequency Ω_1) couples free atoms to the excited intermediate state, and the anti-Stokes laser (Rabi frequency Ω_2) connects the intermediate state to the target state. The anti-Stokes laser is kept at a fixed frequency while the pump laser is scanned to reveal the characteristic Autler-Townes splitting of the photoassociation peak. The detuning configuration is shown in Fig. 4.5(b). For each measurement, we fit an Autler-Townes doublet of

the form [128, 164]

$$N(\delta_1,\delta_2,t) = N_0 \exp\left[-2\pi t \frac{\Gamma |\Omega_1|^2}{\Gamma^2 + 4\delta_1^2} \times \left(1 - |\Omega_2|^2 \frac{|\Omega_2|^2 - 8(\delta_1 - \delta_2)\delta_1 + \Gamma_{\text{eff}}\Gamma\left(1 - 4\delta_1^2/\Gamma^2\right)}{|\Omega_2|^2 + |(\Gamma + 2i\delta_1)\left(\Gamma_{\text{eff}} + 2i(\delta_1 - \delta_2)\right)|^2}\right)\right] \tag{4.7}$$

where δ_1 and δ_2 are the detunings of the pump and anti-Stokes beams respectively, and t is the probe time. Ω_1 and Ω_2 are the corresponding Rabi frequencies. Γ is the excited state linewidth, dominated by power broadening, and Γ_{eff} is a decoherence rate that represents the relative linewidth between the pump and anti-Stokes lasers. Γ_{eff} is a free parameter that was fit to each scan, with an average value of 14(4) kHz.

If only the pump laser is present, i.e., the one-photon free-to-bound transition is driven, then we can set $\Omega_2 = \delta_2 = \Gamma_{\text{eff}} = 0$ and Eq. (4.7) becomes

$$N = N_0 \exp\left(\frac{-2\pi t|\Omega_1|^2\Gamma}{\Gamma^2 + 4\delta_1^2}\right). \tag{4.8}$$

For each excited state, t is fixed and δ_1 is scanned to locate the resonance. Next, the laser is kept on resonance while t is varied, in which case Eq. (4.8) becomes $N = N_0 \exp(-2\pi t|\Omega_1|^2/\Gamma)$. The parameters Ω_1 and Γ are found by fitting these decay curves. Finally, with both lasers turned on we obtain a series of Autler-Townes spectra as shown in the insets of Fig. 4.6.

From fitting the spectral lines to Eq. (4.7), we can directly determine Ω_2 and therefore the relative anti-Stokes transition strengths. Alternatively, the splitting between the higher- and lower-frequency Autler-Townes peaks ($D_\pm$) depends on δ_2 as

$$(D_+ - D_-)^2 = \delta_2^2 + |\Omega_2|^2 \,. \tag{4.9}$$

Therefore, finding the minimum of this parabola, measured with constant laser beam intensities, yields $|\Omega_2|^2$ and the relative transition strengths. Measuring the parabolas for several pairs of

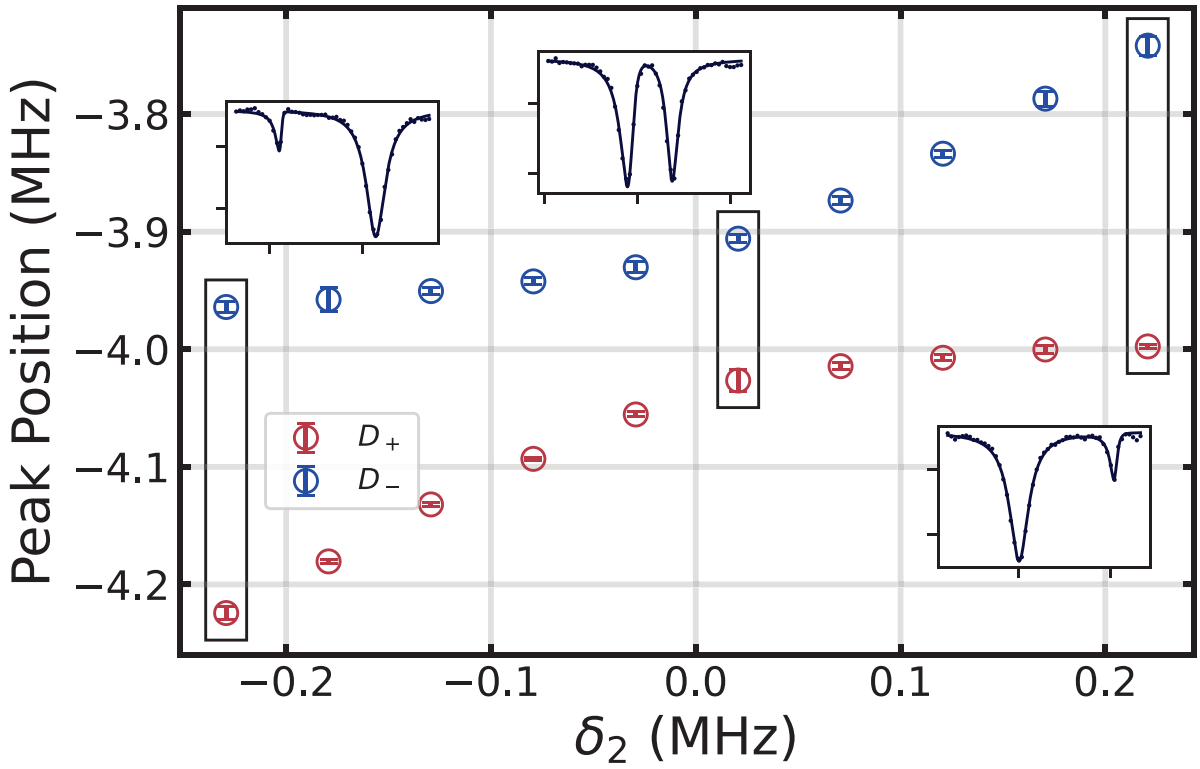

Figure 4.6: Autler-Townes doublet peak positions for the $1_u(-1)$ and $X(-3)$ pair of states. Example scans are shown in insets.

vibrational states yields a direct comparison of transition strengths. The results for all 5 measured state pairs with sizable transition strengths are displayed in Fig. 4.7 and Table 4.1. The quoted transition strengths are normalized to the largest measured value.

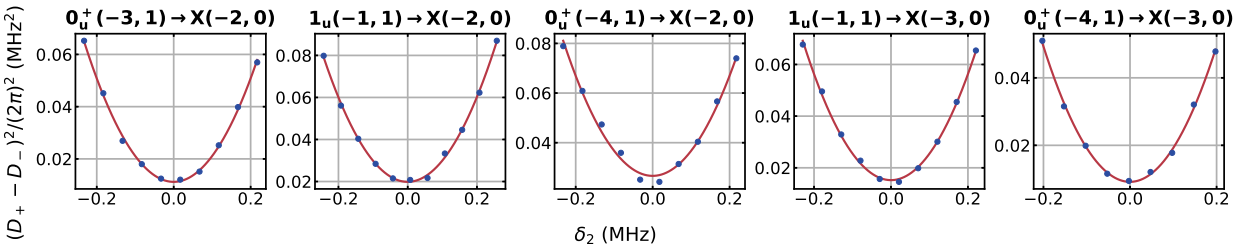

Figure 4.7: All Autler-Townes doublet separation parabolas. The minima of the parabolas are proportional to the relative transition strengths. The quantum numbers in parentheses correspond to (v, J).

Table 4.1: Summary of measured relative transition strengths for photoassociation pathways. Values are normalized to the strongest transition.

$^1S_0 + {}^3P_1$ level	$^1S_0 + {}^1S_0$ level	
	$v = -2$	$v = -3$
$0_u^+(-3, 1)$	0.42(2)	–
$1_u(-1, 1)$	0.74(2)	0.57(2)
$0_u^+(-4, 1)$	1.00(4)	0.34(2)

4.2.2 Production of weakly bound molecules via one-photon photoassociation

Guided by the transition strength measurements summarized in Fig. 4.7, we photoassociate ground state atoms to $0_u^+(-4, 1)$ and allow them to decay into the $X(-2, 0)$ state. An optional two-photon Raman π-pulse is then applied via the $0_u^+(-2, 1)$ (-44.1 MHz) state to move the molecules to the halo state $v = -1$, and a resonance signal is observed as loss from $v = -2$. At the end of each sequence, the remaining $v = -2$ molecules are detected by first photodissociating to the $^1S_0 + {}^3P_1$ threshold and then absorption imaging the atoms. We also can directly photodissociate the halo state to the $^1S_0 + {}^3P_1$ threshold (Fig. 4.8(a)). Attempts to directly populate the $v = -1$ halo state with one-photon photoassociation produced smaller molecule samples. The $1/e$ lifetimes of the $v = -2$ and $v = -1$ halo molecule samples were measured to be $\sim$ 50 ms, limited by two-body collisional loss.

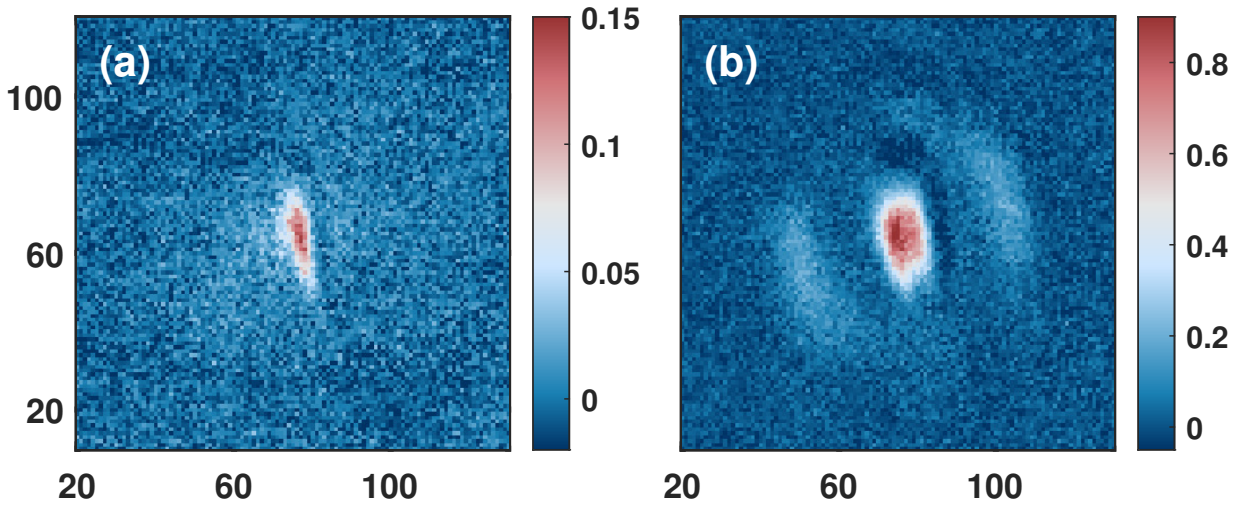

Figure 4.8: Observation of $^{86}Sr_2$ molecule samples via photodissociation and subsequent absorption imaging of the resultant atomic fragments. Images are captured slightly off-axis from the optical lattice. Horizontal axis is along gravity, and both axes are in units of μm. Color bars represent optical density in arbitrary units. (a) The halo state, $v = -1$. Only the state with total angular momentum $J = 0$ is bound. (b) The $v = -2$ molecules, with $J = 0$ dissociation at the center and $J = 2$ molecules receiving a greater kinetic energy and forming the outer ring; odd values of J are forbidden by bosonic quantum statistics.

In order to investigate the collisional properties of the exceptionally large halo molecule, we measured its lifetime and compared it to that of the $v = -2$ state molecules (Fig.4.9). Despite its large internuclear separation, we observe lifetimes comparable to those in the $v = -2$ weakly bound state. Both lifetimes, on the order of tens of milliseconds, are similar to those of the $^{88}Sr_2$ clock states [162].

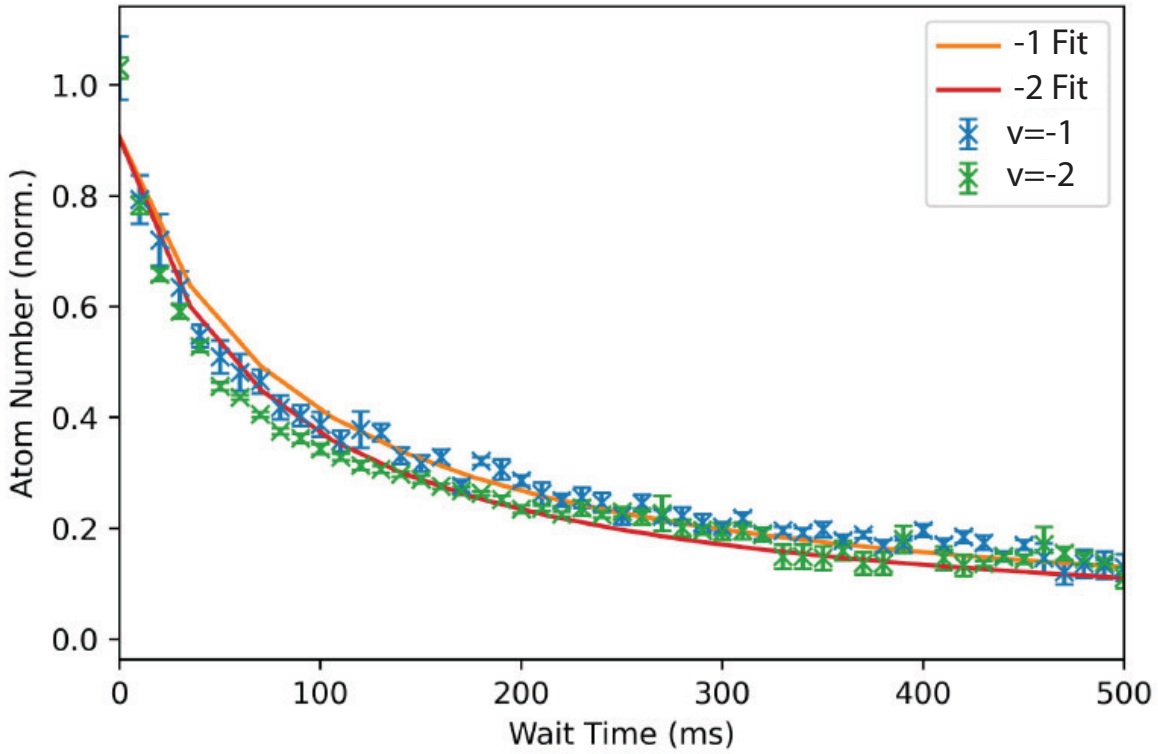

Figure 4.9: Lifetimes of the $v = -1$ and $v = -2$ weakly bound vibrational states. The solid fits are two-body loss curves.

4.3 Precision spectroscopy with weakly bound $^{86}Sr_2$ molecules

4.3.1 Two-photon spectroscopy to measure vibrational splittings

To characterize the ultralong-range portion of the ground-state potential, we measure energy splittings among the three least-bound vibrational states. The splittings are measured via two-photon Raman spectroscopy of the trapped molecular sample, utilizing weakly bound states in the 0_u^+ potential as intermediate states (Fig. 4.10(a)). For each scan (representative lineshapes in Fig. 4.11), the anti-Stokes laser frequency is held fixed, and the pump laser is scanned across the resonance. The common detuning is much larger than any residual Zeeman splitting in 0_u^+. The target vibrational splitting is read off as the difference between the two Raman laser frequencies. Both Raman lasers are phase-locked (with different beat frequencies) to the 689 nm narrow-line

MOT laser, which itself is Pound-Drever-Hall locked to a high-finesse cavity. A further offset is introduced by double-passed AOMs in each beam path. All RF frequencies for the beats and AOMs are generated by direct digital synthesizers referenced to a commercial Rb frequency standard steered by GPS.

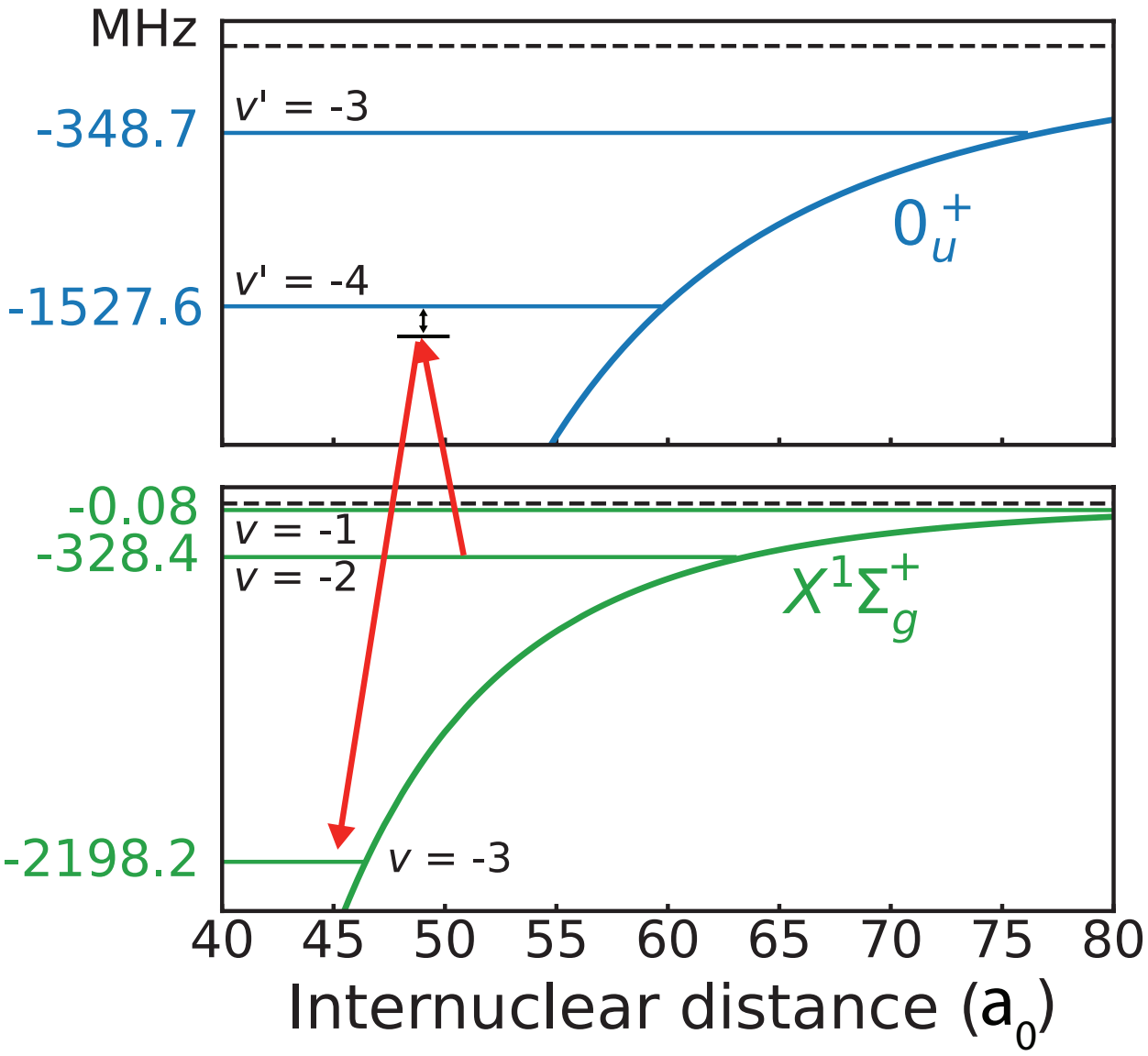

Figure 4.10: Configuration for measurement of the splittings between weakly bound vibrational states.

The $v = -2 \rightarrow v = -1$ transition is fit to a Lorentzian lineshape (Fig. 4.11(a)), while the $v = -2 \rightarrow v = -3$ transition, which is power-broadened, is fit to a Rabi lineshape [Fig. 4.11(b)]:

$$N = \frac{|\Omega|^2}{|\Omega|^2 + \delta^2} \sin^2\left(\frac{\sqrt{|\Omega|^2 + \delta^2}}{2} t\right), \tag{4.10}$$

where Ω is the Rabi frequency, δ is the detuning, and t is pulse time.

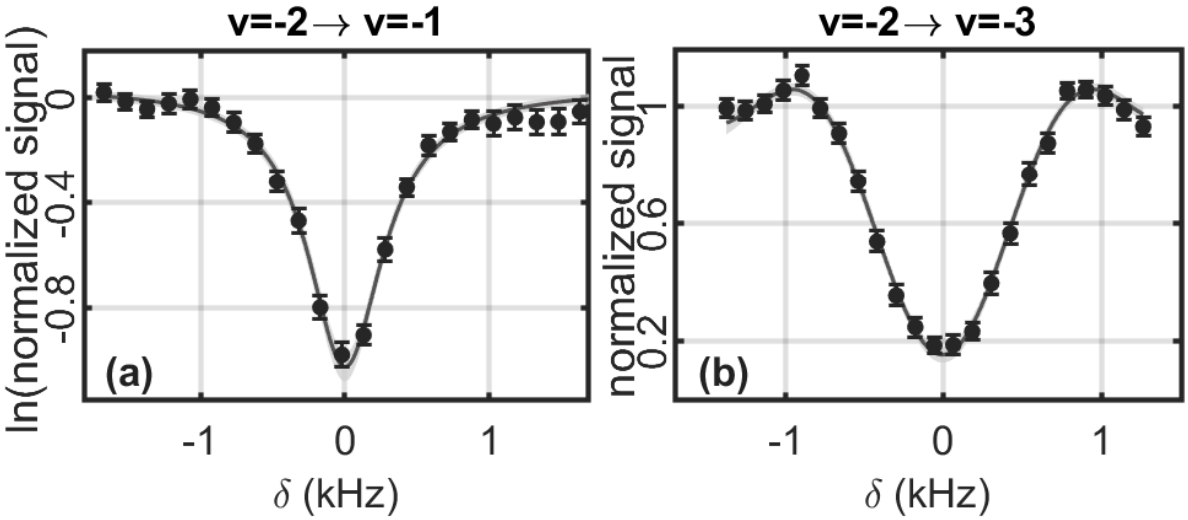

Figure 4.11: Spectra of Raman transitions between weakly bound states at operational intensities for (a) $v = -2 \rightarrow v = -1$ and (b) $v = -2 \rightarrow v = -3$. Black points are (a) natural logarithm of normalized signal and (b) normalized signal versus δ. Fitted curves have (a) Lorentzian and (b) Rabi lineshapes. The error bars display standard error of the mean.

We coherently drive the $v = -2 \rightarrow v = -3$ transition. With both Raman lasers held on resonance and the pulse time varied, the $v = -2$ population oscillates between the two states [Fig. 4.12]. We attribute the coherence-time limit to off-resonant scattering to the excited state and two-photon photodissociation.

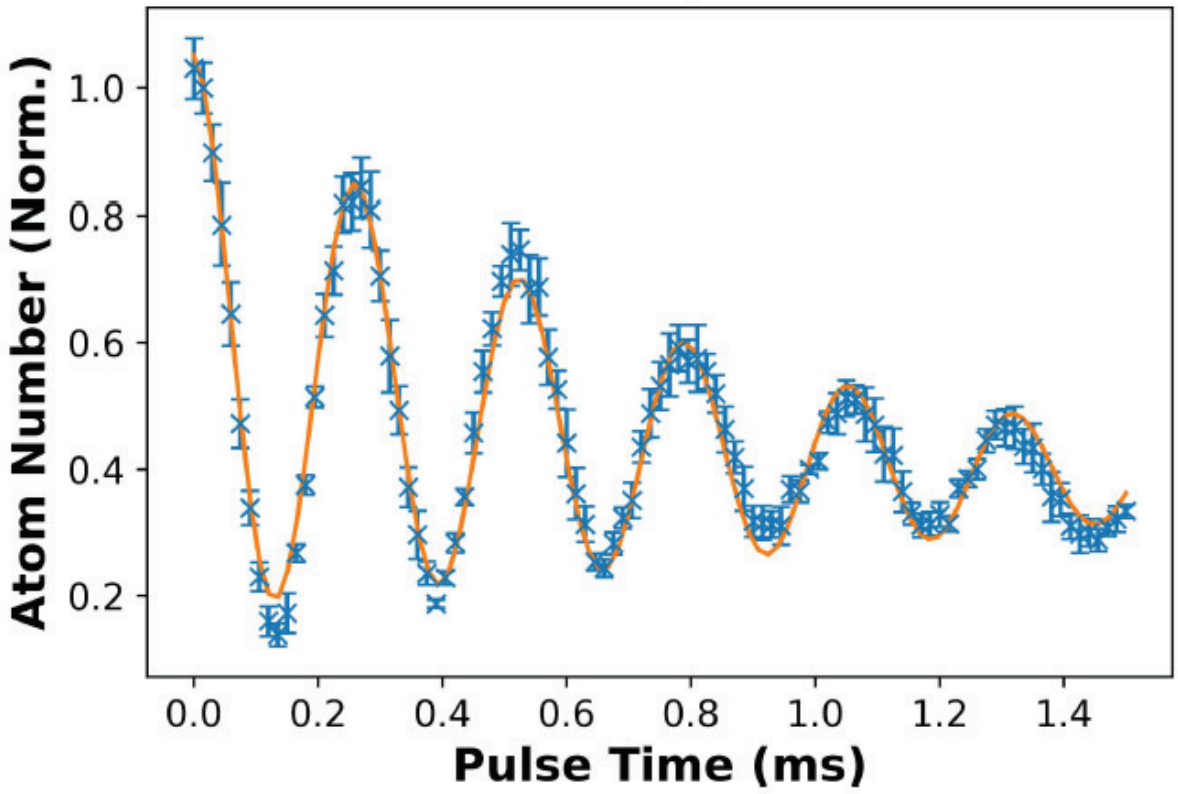

Figure 4.12: Rabi oscillations for a transition between the $v = -2$ and the $v = -3$ states.

The Raman transitions are normally detected as depletion of the initial state at zero relative detuning. Alternatively, directly photodissociating the final state converts the signal into a positive peak (Fig. 4.10(b)). In this scheme, the photodissociation laser selectively dissociates the final state. This approach is only viable when the binding energy of the final state is less than that of the initial state, otherwise both states are dissociated by the PD laser. The resonance then appears as a positive peak rather than a dip (Fig. 4.13). This dual-detection capability will be useful for future clock operation: locking the laser to the transition via a symmetric peak-lock servo, as in atomic clocks [5], requires detection of both initial and final states.

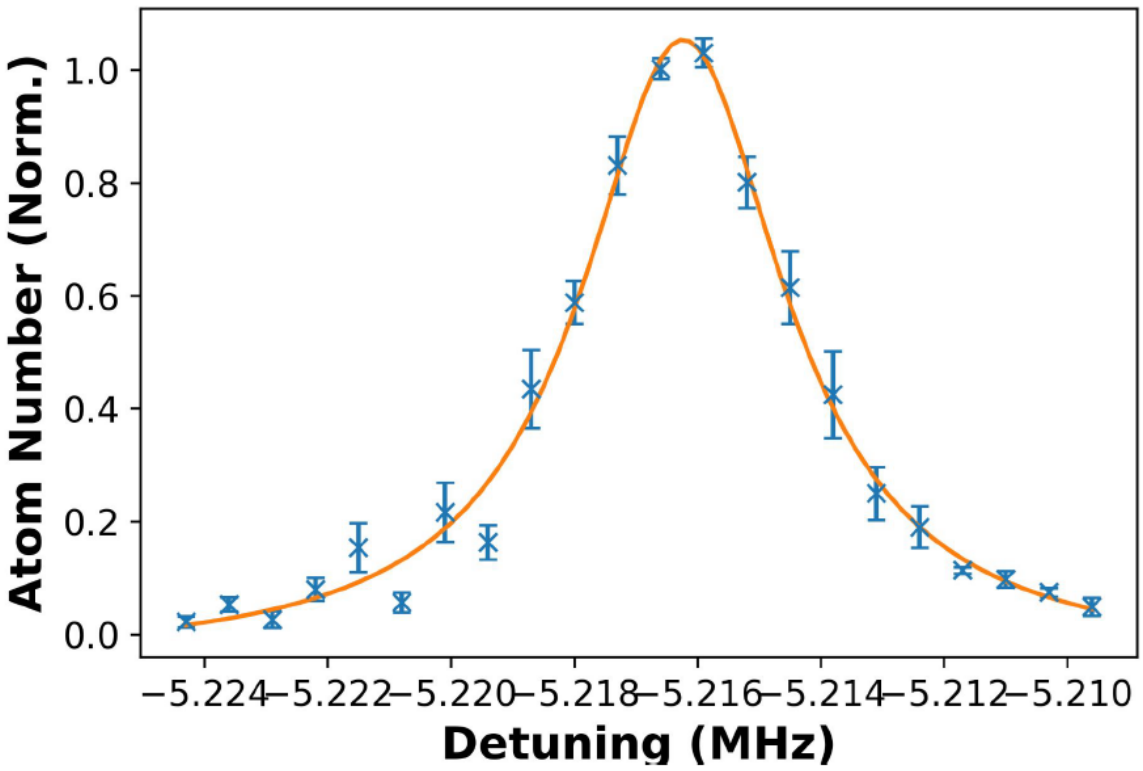

Figure 4.13: Observation of positive peak for the $v = -2 \leftrightarrow v = -1$ transition. Molecules are initialized in the $v = -2$ state, but only the $v = -1$ state is photodissociated as the laser is scanned across the resonance.

4.3.2 Systematic shifts

Determining the vibrational splittings to high precision requires measuring and correcting for systematic shifts. The dominant systematics are Stark shifts from the probe and lattice lasers, which we evaluate to better than 100 Hz uncertainty. For both transitions and for each of the contributing systematic effects, line centers are measured at several laser intensities, with the accessible range limited by available laser power (Fig. 4.14). Each data point averages five trials, and a weighted linear fit extrapolates the shift to zero intensity. The systematic corrections and their uncertainties are reported in Table 4.2.

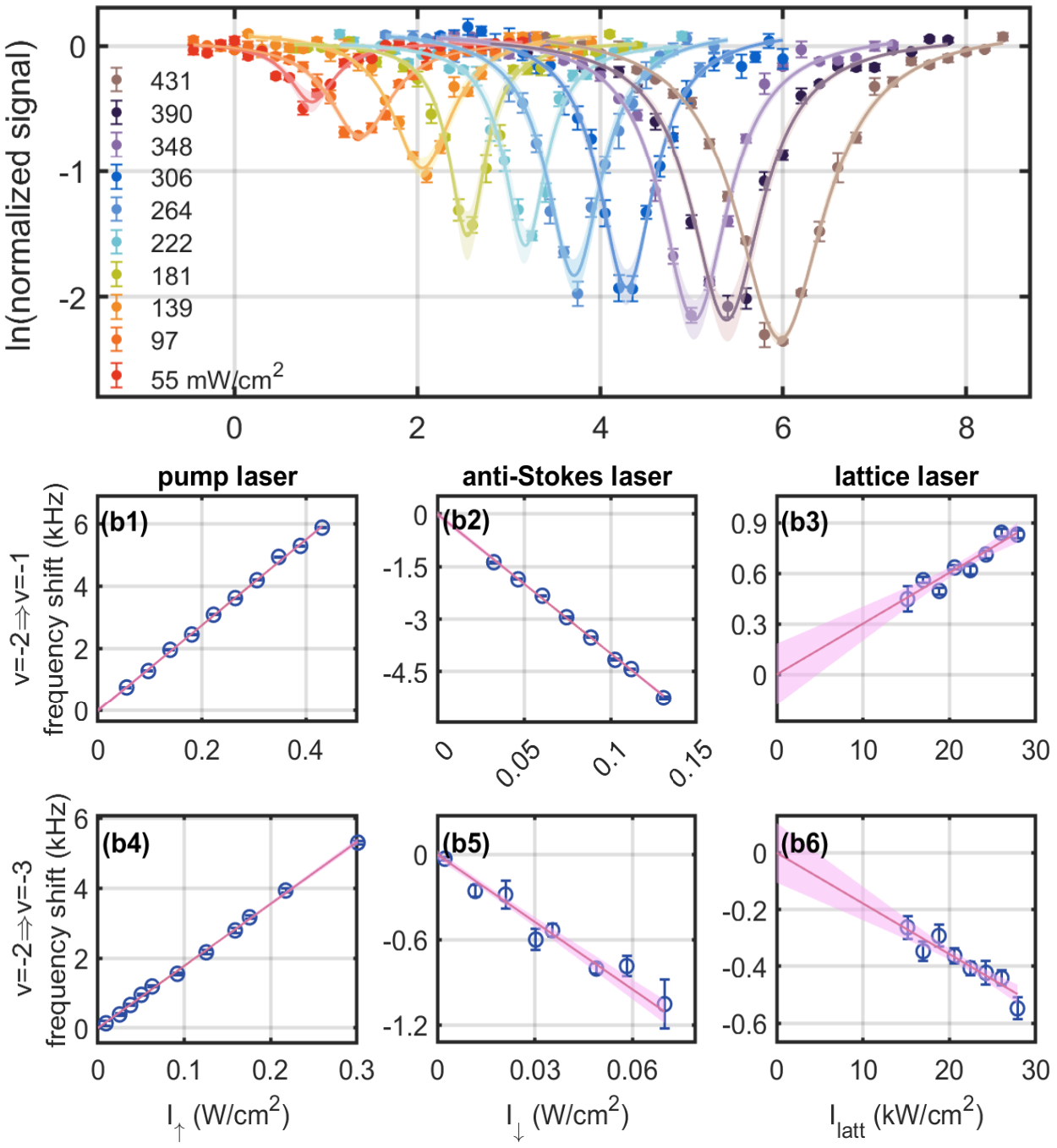

Figure 4.14: (a) Sample spectra of a two-photon Raman transition exhibiting probe light shifts. Points represent data for 10 different upleg probe laser intensities. Error bars are statistical standard errors obtained from 5 trials. Lines represent Lorentzian fits of the natural logarithm of the detected atom number. Lower panels: Shifts induced by probe and lattice lasers versus light intensity for $v = -2 \rightarrow v = -1$ (b, top row) and $v = -2 \rightarrow v = -3$ (b, bottom row). (b1,b4) Light shifts induced by the pump laser; (b2,b5) light shifts induced by the anti-Stokes laser; and (b3,b6) light shifts induced by the lattice laser.

Table 4.2: Leading systematic shifts (light shifts due to the probe and lattice lasers) for $v = -2 \rightarrow v = -1$ and $v = -2 \rightarrow v = -3$ vibrational splitting measurements.

Stark shift (Hz)	$v = -2 \rightarrow v = -1$	$v = -2 \rightarrow v = -3$
Pump	1820(50)	742(32)
Anti-Stokes	−1855(46)	−147(25)
Lattice	567(37)	−335(23)
Total	**532(77)**	**259(47)**

4.3.3 Results

After applying these systematic corrections, we obtain the vibrational splittings: 328.394 288 (78) MHz for $v = -2 \rightarrow v = -1$ and 1869.681 045 (47) MHz for $v = -2 \rightarrow v = -3$. Combined with the previously reported $v = -1$ halo-state binding energy of −83.00(7)(20) kHz [235], these splittings yield the absolute binding energies of the weakly bound states $v = -2$ and $v = -3$ (Table 4.3).

Table 4.3: Binding energies of weakly bound states in the $X^1\Sigma_g^+$ potential of $^{86}Sr_2$, calculated with the measured vibrational splittings and the halo state binding energy previously determined via photoassociative spectroscopy [235].

Vibrational state	Binding energy (kHz)
$v = -1$	−83.00(7)(20) [235]
$v = -2$	−328,477.288(226)
$v = -3$	−2,198,158.333(231)

4.3.4 Two-photon photodissociation

As a cross-check, we measure the absolute binding energy directly via two-photon photodissociation to the atomic $^1S_0 - ^1S_0$ threshold. The frequency difference between the two PD lasers at resonance equals the binding energy (Fig. 4.15). We can fit the following equation:

$$N(f) = C + N_0 \cdot \left(1 - e^{C_{2D} \cdot \left[\pi/2 + \tan^{-1}(2(f - f_0)/\gamma)\right]}\right), \tag{4.11}$$

following [250], where f_0 is the desired frequency difference. For $v = -2$, this yields 328.6(8) MHz, in good agreement with the Raman-spectroscopy value. We observe positive signal

in this scheme. The $v = -2$ state is populated via one-photon PA, then the relative detuning for two-photon PD is scanned until the dissociation signal recovers.

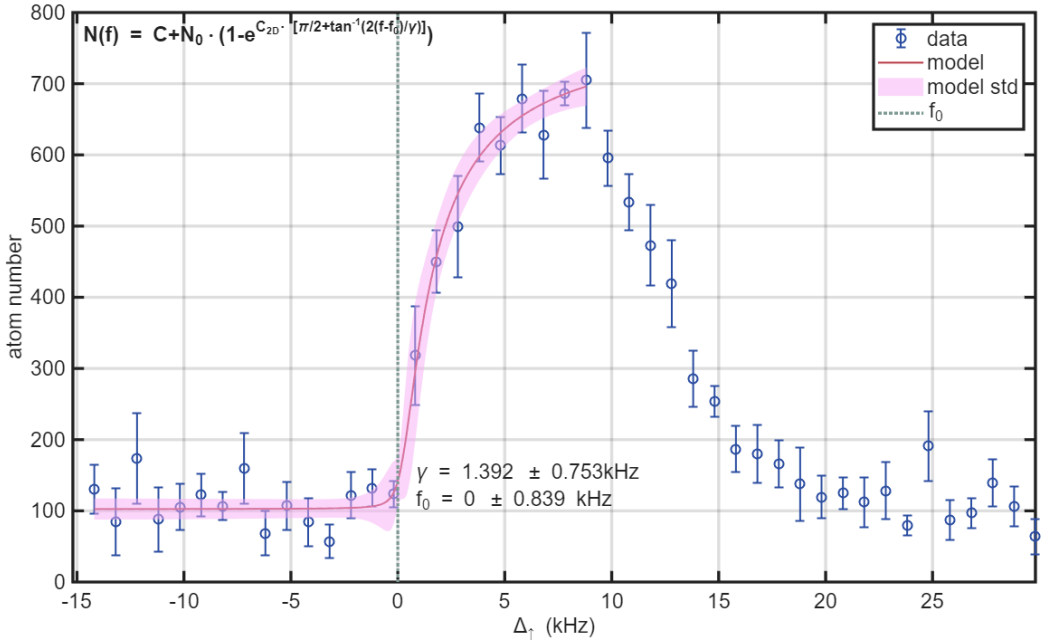

Figure 4.15: Two-photon photodissociation of the $v = -2$ weakly bound vibrational state. The difference between the two laser frequencies gives the absolute binding energy relative to the threshold. The model fit is shown using the PD equation, and the pink shading is the standard error of the fit.

4.4 Summary

We have demonstrated the first stable production of weakly bound $^{86}Sr_2$ molecules, identified favorable PA pathways, and measured transition strengths between weakly bound excited-state and ground-state levels. We performed sub-kHz level spectroscopy of the vibrational splittings among the three least bound states, after evaluating the dominant Stark-shift systematics. These measurements introduce a new platform for probing long-range internuclear interactions. The spinless ground-state $^{86}Sr_2$ is particularly amenable to *ab initio* quantum chemistry calculations, enabling precise characterization of effects such as the Casimir-Polder interaction. This work is also a step toward a molecular isotope-shift measurement. The next step is to characterize the

entire ground-state potential in $^{86}Sr_2$. Longer-term, we aim to measure its clock transition.

Chapter 5: Evaluation of Sr_2 *ab initio* calculations

As a first step toward a precision molecular isotope shift measurement, we perform coarse spectroscopy of the full $X^1\Sigma_g^+$ ground-state potential of $^{86}Sr_2$ using frequency comb-assisted EIT spectroscopy, similar to how we have done previously. This provides a complete map of the ground-state potential to MHz-level precision. Using the same data measured previously with $^{88}Sr_2$[163], we can experimentally determine the isotope shifts of all 63 levels between $^{88}Sr_2$ and $^{86}Sr_2$. We first measure the binding energy of the absolute ground state ($v = 0$) to sub-MHz precision after evaluating the dominant systematic, the lattice lightshift.

Our theory collaborators in the Moszynski group have been performing *ab initio* calculations of the $X^1\Sigma_g^+$ ground-state potential using state-of-the-art quantum chemistry methods. They calculated the Born-Oppenheimer potential, as well as the smaller beyond-Born-Oppenheimer (BBO) corrections. They previously used the pseudopotential method, which is isotope-independent. Here we report results from the Dirac-Coulomb method. The *ab initio* calculations produce discrete points, which we convert into a continuous analytical form by fitting. We describe this fitting procedure here.

To compare with experiment, we solve the Schrödinger equation on the fitted potential to obtain vibrational bound-state energies, and we can directly compare to the experimentally measured values. In particular, the exceptionally large spatial extent of the $^{86}Sr_2$ halo state makes it a sensitive probe of the Casimir-Polder interaction[236]. By fitting the theoretical potential first to *ab initio* points and then to the experimental $^{86}Sr_2$ data, we aim to demonstrate that the Casimir-Polder retardation is required to reproduce the halo-state binding energy.

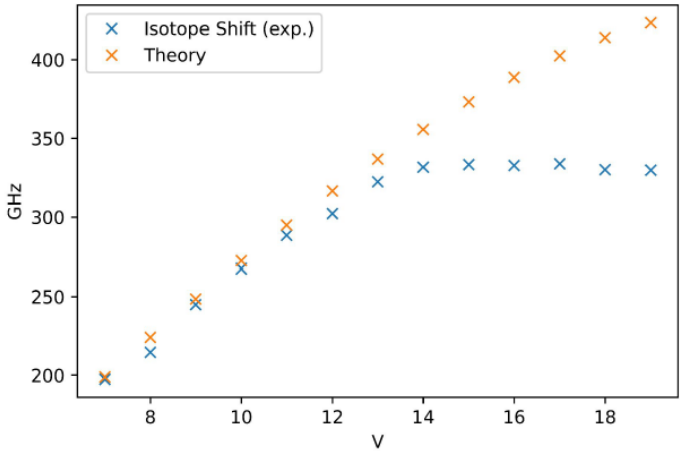

Figure 5.1: Theory prediction for the isotope shift of the 0_u^+ potential vs. experimental measurements. 'Theory' measurement is from a Morse long-range fit to experimental data [163, 164, 251]

5.1 $^{86}Sr_2$ spectroscopy

5.1.1 0_u^+ Excited state spectroscopy

To perform full spectroscopy of the ground-state potential, we first must find suitable intermediate states. These are typically deeply bound states in the excited-state 0_u^+ potential, accessed here by one-photon spectroscopy from molecules initialized in the weakly bound $v = -2$ state. The relevant transition wavelength is near 780 nm. The one-photon pulse depletes population from $v = -2$, and the remaining $v = -2$ population is detected via state-selective PD. Scanning the laser detuning across the resonance yields a characteristic depletion dip. We scan across 13 deeply bound states in the 0_u^+ potential, and report their binding energies here [Table 5.1]. We can also report the isotope shift of these levels relative to $^{88}Sr_2$, which we show in Figure 5.1.

Table 5.1: Vibrational energy levels for the 0_u^+ state of $^{88}Sr_2$ and $^{86}Sr_2$. All values in MHz; uncertainties in parentheses.

	$^{88}Sr_2$		$^{86}Sr_2$	
v	$E(J{=}1)$ (MHz)	$E(J{=}3) - E(J{=}1)$	$E(J{=}1)$	$E(J{=}3) - E(J{=}1)$
7	66 016 088(60)	—	65 818 697(50)	7 156(10)
8	63 745 468(60)	—	63 531 012(50)	6 905(10)
9	61 497 833.94(12)	—	61 252 849(50)	7 077(10)
10	59 275 910.26(35)	—	59 008 514(50)	7 032(10)
11	57 084 156.51(12)	—	56 795 780(50)	6 988(10)
12	54 929 909.90(11)	—	54 622 759(50)	6 932(10)
13	52 825 520.41(4)	—	52 503 225(50)	6 868(10)
14	50 791 292.56(10)	—	50 459 693(50)	6 781(10)
15	48 855 512.13(18)	—	48 522 233(50)	6 653(10)
16	47 036 433.95(23)	—	46 703 799(50)	6 531(10)
17	45 320 332.03(14)	—	44 986 592(50)	6 417(10)
18	43 686 942.35(9)	—	43 356 907(50)	6 300(10)
19	42 124 784.98(7)	—	41 798 118(50)	6 206(10)

5.1.2 Ground state spectroscopy

We perform EIT spectroscopy in order to find the binding energies of all of the vibrational states in the ground-state potential. We are guided by previous Fourier transform spectroscopy of Sr_2[209], which serves as a starting point for our spectroscopy search. To initially locate each state, we deliberately power-broaden the transitions using high probe intensity. The upleg laser is a Toptica DL pro, locked to a high-finesse cavity via a double-pass AOM and further controlled by a second double-pass AOM that also serves as a shutter. The downleg laser is a Ti:Sapphire laser, chosen for its broad tunability. Its output bypasses any AOM, so the molecules see the bare laser frequency, simplifying the binding-energy determination. The carrier envelope offset of the optical frequency comb is stabilized to a radiofrequency signal, and the repetition rate is stabilized to the upleg laser. The procedure is as follows: the upleg frequency is tuned to resonance, and the power is adjusted until $\sim$ 90% depletion is observed in a 10 ms pulse time. The downleg is then set to maximum power ($\sim$ 50 mW) and tuned to the expected binding energy from Ref. [209].

When both lasers are on resonance, we observe recovery of the $v = -2$ signal, or lack of depletion [Fig. 5.2(a)]. At this high power, the recovery feature is broadened. We reduce the downleg power until we transition from the Autler-Townes to the EIT regime, and the center recovery feature is sub-MHz width.

For the $v = 0$ absolute ground state we lock the downleg to the comb when it is on resonance. Scanning the upleg laser across the broad depletion feature reveals a typical EIT lineshape [Fig. 5.2(a)], which is fit to

$$N(\delta_1, \delta_2, t) = N_0 \exp\left[-2\pi t \frac{\Gamma|\Omega_1|^2}{\Gamma^2 + 4\delta_1^2}\right] \times \left(1 - |\Omega_2|^2 \frac{|\Omega_2|^2 - 8(\delta_1 - \delta_2)\delta_1 + \Gamma_{\text{eff}}\Gamma\left(1 - 4\delta_1^2/\Gamma^2\right)}{|\Omega_2|^2 + |(\Gamma + 2i\delta_1)(\Gamma_{\text{eff}} + 2i(\delta_1 - \delta_2))|^2}\right) \tag{5.1}$$

where N_0 is the initial atom number, $\delta_{1,2}$ are the detunings of the pump and anti-Stokes lasers, $\Omega_{1,2}$ are the respective Rabi frequencies, Γ is the excited-state linewidth, Γ_{eff} is the relative linewidth between the two lasers, and t is the probe time. From this fit, we can obtain the peak center. The laser frequency difference at the molecules corresponds to the relative binding energy difference. For this absolute ground state, we want to measure to higher precision, so we choose to measure the dominant systematic. Since we are not in a magic lattice, the lattice lightshift is by far the dominant systematic. We evaluate this by measuring the EIT feature at different lattice intensities and linearly extrapolating to zero intensity [Fig. 5.2(b)], giving a relative binding energy to be 31 818 437.1566(447) MHz.

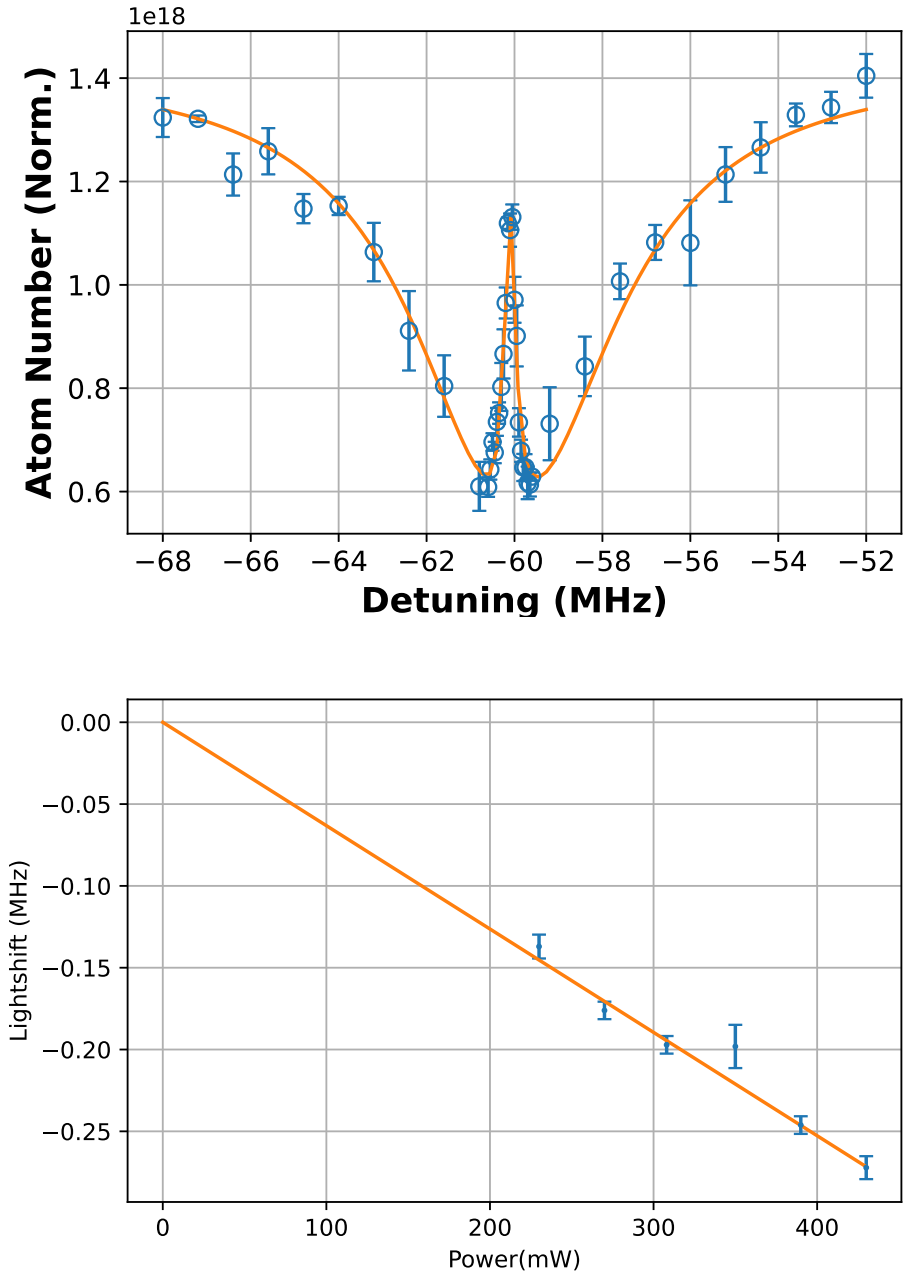

Figure 5.2: (a) Example EIT scan for $v = 61 \leftrightarrow v = 0$ transition. Corresponds to the power=310 mW point in the lightshift plot. (b) Lattice lightshift for the $v = 61 \leftrightarrow v = 0$ transition.

We then moved on to performing coarse spectroscopy of the entire ground-state potential. We used two intermediate states, $0_u^+(11,1)$ and $0_u^+(15,1)$. In general, we use a similar procedure where we leave the upleg on resonance depleting roughly 90% of the signal. After finding the EIT resonance at high power, we lower the power until we can resolve the resonance position to ±3 MHz. Instead of locking the downleg laser to the comb, we monitor the beat frequency between the downleg laser and the comb with a spectrum analyzer. Using this method, we measured the remaining vibrational states $v = 1-60$ [Fig. 5.3]. Several of the states had a much lower transition strength, even at maximum downleg power, which is why we had to use a second intermediate state.

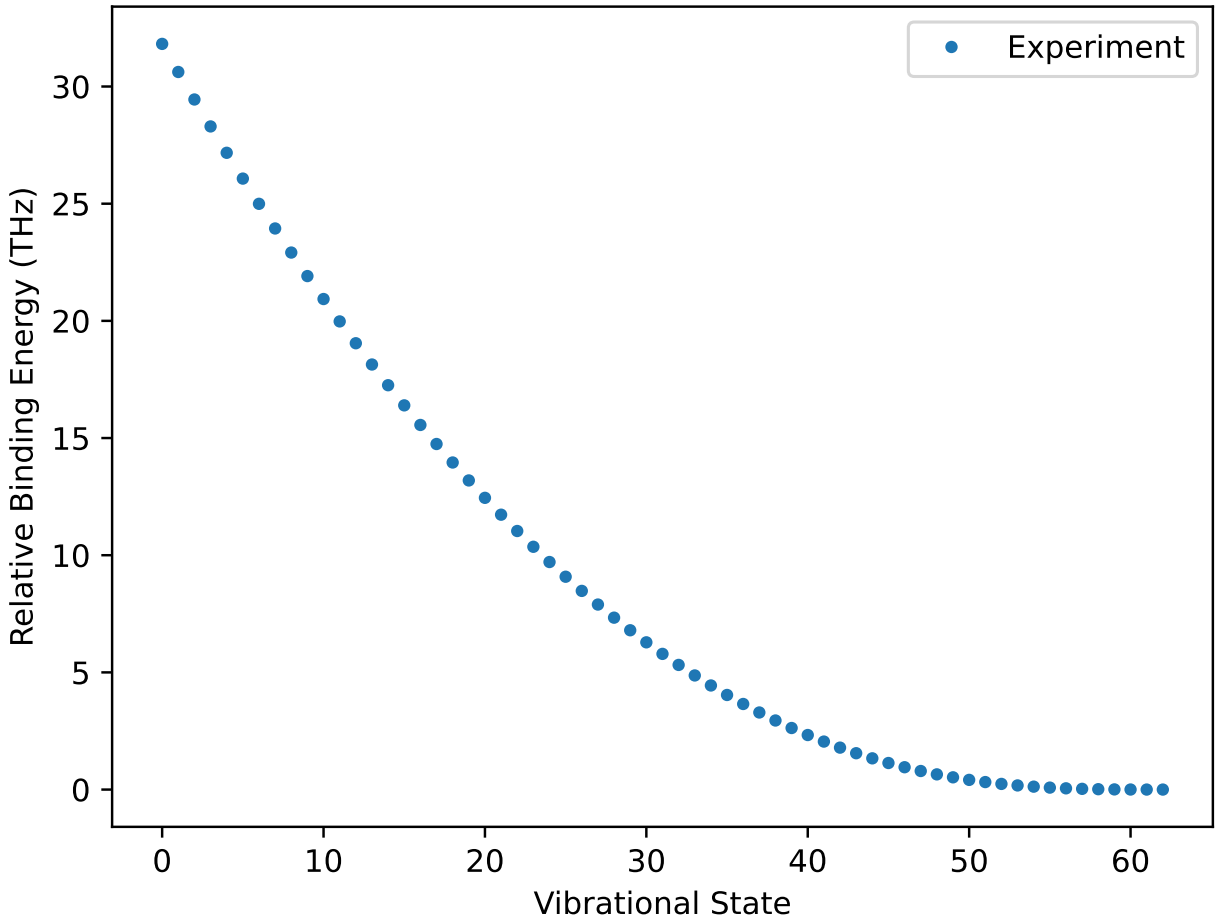

Figure 5.3: Relative binding energies for the vibrational states $v = 0-61$ in $^{86}Sr_2$. In this case, binding energies are positive, so $v = 0$ is the most deeply bound vibrational state.

Combining our reported absolute binding energies for $v = 60, 61$[252], the reported binding energy for $v = 62$[235], and these measured values, we have the absolute binding energies for all vibrational states in the $X^1\Sigma_g^+$ potential for $^{86}Sr_2$. We report them in Table 5.2. Using the previously measured binding energies for $^{88}Sr_2$, we can determine the isotope shifts for all 63 vibrational states between $^{88}Sr_2$ and $^{86}Sr_2$. We plot them in Figure 5.4. We find good agreement with the Fourier transform spectroscopy values [209]. We can observe the vibrational state dependence of the isotope shift.

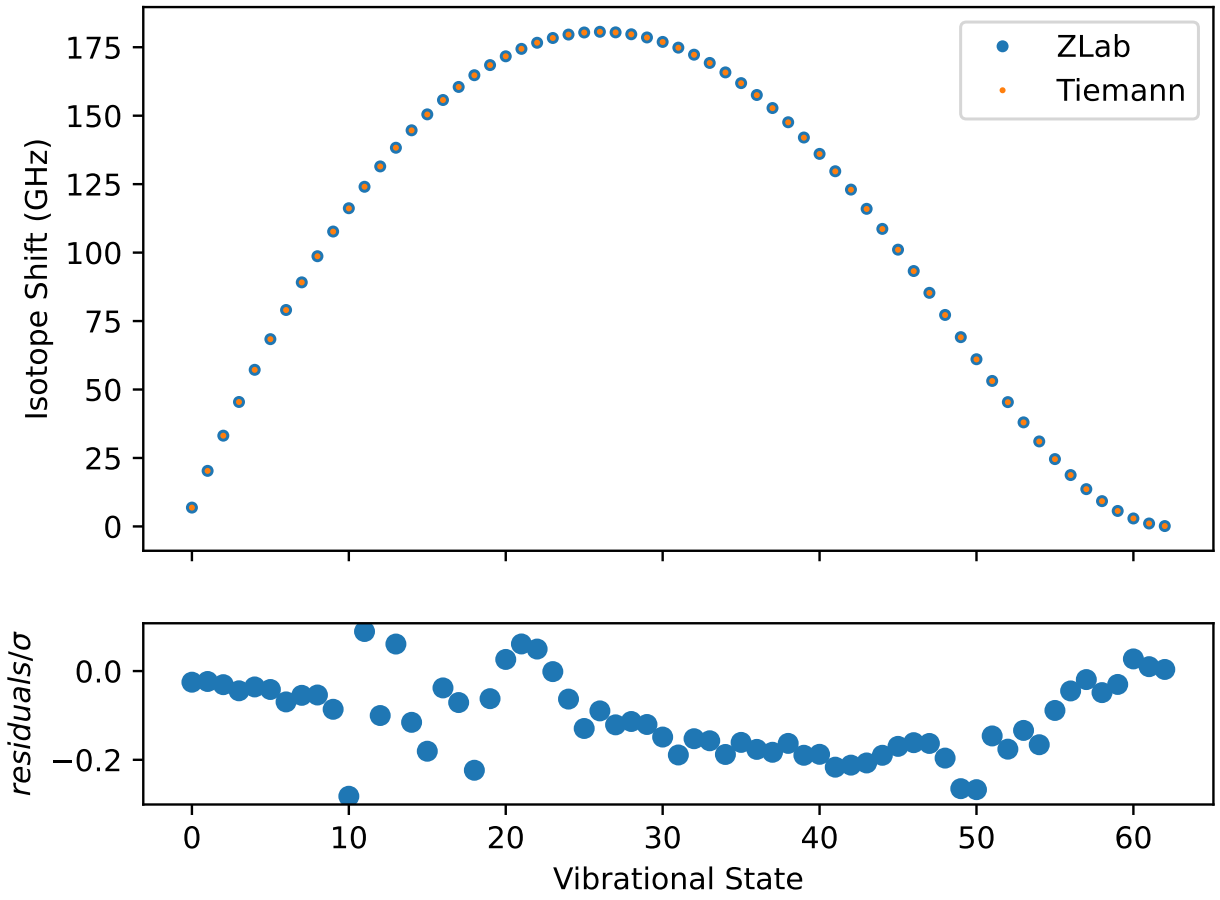

Figure 5.4: Isotope shift for all 63 vibrational states in the X potential between $^{88}Sr_2$ and $^{86}Sr_2$. The larger blue circles are experimental measurements. The smaller orange circles are from Fourier-transform spectroscopy [209]. The bottom figure shows the ratio of the residuals to the combined uncertainty σ. These uncertainties are dominated by the Fourier transform spectroscopy measurements.

Table 5.2: Absolute binding energies $|E_{J=0}|$ (MHz) of vibrational levels of the $X0_g^+$ state of $^{88}Sr_2$ and $^{86}Sr_2$. Uncertainties in parentheses refer to the last quoted digit(s).

v	$^{88}Sr_2$	$^{86}Sr_2$
0	31 825 319.852(5)	31 818 437.2396(447)
1	30 640 296.437(28)	30 620 004(5)
2	29 479 197.638(27)	29 446 049(5)
3	28 342 002.355(26)	28 296 551(5)
4	27 228 683.489(11)	27 171 488(5)
5	26 139 208.322(26)	26 070 817(5)
6	25 073 538.149(11)	24 994 498(5)
7	24 031 629.148(26)	23 942 497(5)
8	23 013 431.546(11)	22 914 751(5)
9	22 018 900(120)	21 911 205(5)
10	21 048 000(120)	20 931 794(5)
11	20 100 500(120)	19 976 460(5)
12	19 176 600(120)	19 045 124(5)
13	18 276 000(120)	18 137 706(5)
14	17 398 800(120)	17 254 135(5)
15	16 544 800(120)	16 394 317(5)
16	15 713 900(120)	15 558 171(5)
17	14 906 100(120)	14 745 601(5)
18	14 121 300(120)	13 956 517(5)
19	13 359 300(120)	13 190 820(5)
20	12 620 100(120)	12 448 413(5)
21	11 903 600(120)	11 729 197(5)
22	11 209 700(120)	11 033 069(5)

continued on next page

Table 5.2 – continued

v	$^{88}Sr_2$	$^{86}Sr_2$
23	10 538 300(120)	10 359 928(5)
24	9 889 287(120)	9 709 663(5)
25	9 262 568(120)	9 082 180(5)
26	8 658 009(120)	8 477 367(5)
27	8 075 549(120)	7 895 117(5)
28	7 515 067(120)	7 335 332(5)
29	6 976 461(120)	6 797 892(5)
30	6 459 628(120)	6 282 688(5)
31	5 964 469(120)	5 789 620(5)
32	5 490 845(120)	5 318 566(5)
33	5 038 674(120)	4 869 409(5)
34	4 607 839(120)	4 442 030(5)
35	4 198 199(120)	4 036 302(5)
36	3 809 659(120)	3 652 099(5)
37	3 442 049(120)	3 289 255(5)
38	3 095 249(120)	2 947 642(5)
39	2 769 099(120)	2 627 072(5)
40	2 463 424(120)	2 327 373(5)
41	2 178 039(120)	2 048 329(5)
42	1 912 719(120)	1 789 708(5)
43	1 667 229(120)	1 551 244(5)
44	1 441 289(120)	1 332 629(5)
45	1 234 579(120)	1 133 505(5)
46	1 046 739(120)	953 465(5)

continued on next page

Table 5.2 – continued

v	$^{88}Sr_2$	$^{86}Sr_2$
47	877 339(120)	792 032(5)
48	725 889(120)	648 654(5)
49	591 819(120)	522 693(5)
50	474 464(120)	413 405(5)
51	373 094(120)	319 958(5)
52	286 789(120)	241 388(5)
53	214 639(120)	176 634(5)
54	155 564(120)	124 521(5)
55	108 369(120)	83 777(5)
56	71 824(120)	53 063(5)
57	44 599(120)	30 981(5)
58	25 339(120)	16 101(5)
59	12 639(120)	6 986(5)
60	5 110.5739(51)	2 198.8290(2)
61	1 400.3182(50)	328.4773(2)
62	136.6447(50)	0.0830(2)

5.2 *Ab initio* ground-state potential

5.2.1 Background: Coupled-cluster methods

With the Born-Oppenheimer approximation[253], we can separate the electronic and nuclear wavefunctions:

$$\Psi_{total}(\vec{x}_i, r) \approx \phi_{elec}(\vec{x}_i; r)\Psi_{nuc}(r) \tag{5.2}$$

$$\Psi_{nuc}(r) = R_{v,J}(r)Y_{JM}(\theta, \phi) \tag{5.3}$$

where $\vec{x}_i$ is the combined coordinate r_i and $m_{s,i} = \pm 1/2$ and $i = 1 \rightarrow n$. $\phi_{elec}(\vec{x}_i; r)$ means that the electronic wavefunction depends parametrically on r. This is valid because the nuclear mass is much larger than the electron mass. This means that for different arrangements of the nuclei, ϕ_{elec} is a different function of the electronic coordinates. The exact solution requires completeness in both the one-electron (orbital) space and the N-electron (Fock) space; errors in each are qualitatively different and cannot compensate for one another. We can solve the Schrödinger equation separately for the electrons and nuclei. We first solve:

$$\hat{H}|0\rangle = E|0\rangle \tag{5.4}$$

The spin-free nonrelativistic second quantization representation of the molecular electronic Hamiltonian is[254]

$$\hat{H} = \sum_{PQ} h_{PQ}\, a_P^\dagger a_Q + \frac{1}{2} \sum_{PQRS} g_{PQRS}\, a_P^\dagger a_R^\dagger a_S a_Q + h_{\text{nuc}} \tag{5.5}$$

$$h_{PQ} = \int \phi_P^*(\mathbf{x}) \left(-\frac{1}{2}\nabla^2 - \sum_I \frac{Z_I}{r_I} \right) \phi_Q(\mathbf{x})\, \mathrm{d}\mathbf{x}, \tag{5.6}$$

$$g_{PQRS} = \iint \frac{\phi_P^*(\mathbf{x}_1)\phi_R^*(\mathbf{x}_2)\phi_Q(\mathbf{x}_1)\phi_S(\mathbf{x}_2)}{r_{12}}\, \mathrm{d}\mathbf{x}_1\, \mathrm{d}\mathbf{x}_2, \tag{5.7}$$

$$h_{\mathrm{nuc}} = \frac{1}{2} \sum_{I \neq J} \frac{Z_I Z_J}{R_{IJ}}. \tag{5.8}$$

and h_{nuc} is the nuclear repulsion term.

The molecular orbitals are expanded in a finite set of nonorthogonal atomic orbitals, which is a function of the Cartesian coordinates of a single electron:

$$\phi_p(\mathbf{r}) = \sum_\mu C_{\mu p} \chi_\mu(\mathbf{r}) \tag{5.9}$$

We may express the solution to the Schrödinger equation as a superposition of determinants:

$$|0\rangle = \sum_i C_i |i\rangle \tag{5.10}$$

The two-electron Coulomb repulsion term prevents the electronic Hamiltonian from being written as a sum of one-electron operators, making the exact many-body wavefunction non-separable into a product of single-electron functions. The full wavefunction cannot be written as $\Psi(\mathbf{r}_1, ..., \mathbf{r}_N) = \phi_1(\mathbf{r}_1)...\phi_N(\mathbf{r}_N)$. The total energy for fixed nuclei also includes the constant nuclear repulsion.

The total energy $\mathcal{E}_{\mathrm{elec}}(\{\mathbf{R}_A\})$ provides a potential for nuclear motion.

With the Hartree-Fock approximation, the electronic wave function is approximated by a single configuration of spin orbitals, and the energy is optimized with respect to variations of these spin orbitals[255, 256]. The Hartree-Fock determinant is the one that minimizes the energy, and each electron moves in the average field of all others. The simplest antisymmetric N-electron

wavefunction is a single Slater determinant of spin-orbitals,

$$|\phi_{P_1}\phi_{P_2}\cdots\phi_{P_N}| = \frac{1}{\sqrt{N!}}\begin{vmatrix} \phi_{P_1}(\mathbf{x}_1) & \phi_{P_2}(\mathbf{x}_1) & \cdots & \phi_{P_N}(\mathbf{x}_1) \\ \phi_{P_1}(\mathbf{x}_2) & \phi_{P_2}(\mathbf{x}_2) & \cdots & \phi_{P_N}(\mathbf{x}_2) \\ \vdots & \vdots & \ddots & \vdots \\ \phi_{P_1}(\mathbf{x}_N) & \phi_{P_2}(\mathbf{x}_N) & \cdots & \phi_{P_N}(\mathbf{x}_N) \end{vmatrix} \tag{5.11}$$

The wave function may be written in the form

$$|\ \kappa\rangle = exp(-\hat{\kappa})|0\rangle \tag{5.12}$$

where the operator $\hat{\kappa}$ is written as

$$\hat{\kappa} = \sum_{PQ} \kappa_{PQ} a_P^\dagger a_Q \tag{5.13}$$

The ground-state Hartree-Fock wave function is obtained by minimizing the energy with respect to the orbital-rotation parameters

$$E_{\mathrm{HF}} = \min_{\boldsymbol{\kappa}} \langle \boldsymbol{\kappa}|\hat{H}|\boldsymbol{\kappa}\rangle \tag{5.14}$$

The optimal Hartree-Fock determinant may be found by solving a set of effective one electron Schrödinger equations called the Hartree-Fock equations, and the associated Hamiltonian is the Fock operator

$$\hat{f} = \sum_{PQ} f_{PQ} a_p^\dagger a_Q \tag{5.15}$$

The elements make up the Fock matrix. In the Fock operator, the electron portion of the Hamiltonian is kept the same, but the two-electron part is replaced

$$\hat{f} = \hat{h} + \hat{V}, \tag{5.16}$$

$$\hat{V} = \sum_{PQ} V_{PQ} a_P^\dagger a_Q, \tag{5.17}$$

$$V_{PQ} = \sum_I (g_{PQII} - g_{PIIQ}) \tag{5.18}$$

Where the index I is over all occupied spin orbitals and P and Q are over all spin orbitals (occupied and unoccupied). The Fock potential $\hat{V}$ incorporates the Coulomb repulsion in an average sense, corrected for Fermi (exchange) correlation through the antisymmetry of the wave function.

The Fock equations are solved by diagonalizing the Fock matrix:

$$f_{PQ} = \delta_{PQ} \varepsilon_P. \tag{5.19}$$

The Fock matrix is defined in terms of its own eigenvectors, so it can only be diagonalized with an iterative procedure. The remaining higher orbitals $\phi_{N+1}, \phi_{N+2}, ...$ are called virtual orbitals. Standard notation uses $I, J, K, ...$ for occupied orbitals, and $A, B, C, ...$ for virtual orbitals.

We use coupled-cluster with singles, doubles and perturbative triples. It improves on the Hartree-Fock procedure by incorporating electron correlation, the tendency of electrons to avoid each other beyond what the mean-field approximation describes.

We start from the Hartree-Fock reference $|HF\rangle$:

$$|CC\rangle = exp(\hat{T})|HF\rangle \tag{5.20}$$

Where $\hat{T}$ is the cluster operator. Unlike the linear CI parametrization, the exponential ansatz ensures size-extensivity, because the wave function factorizes for non-interacting subsystems.

The Hartree–Fock equations yield a complete set of spin-orbitals $\{\chi_p\}$, of which the N lowest in energy are *occupied* and appear in $|\Phi_0\rangle$ (labeled $I, J, K, \dots$), while the remainder are *virtual* (unoccupied) orbitals (labeled $A, B, C, \dots$) that do not appear in the reference determinant.

For coupled-cluster singles and doubles [257, 258],

$$\begin{aligned} \hat{T} &= \hat{T}_1 + \hat{T}_2 \\ \hat{T}_1 &= \sum_{AI} t_I^A \hat{a}_A^\dagger \hat{a}_I \\ \hat{T}_2 &= \frac{1}{4} \sum_{\substack{AB \\ IJ}} t_{IJ}^{AB} \hat{a}_A^\dagger \hat{a}_B^\dagger \hat{a}_I \hat{a}_J \end{aligned} \tag{5.21}$$

where t_{IJ}^{AB} are antisymmetric in AB and antisymmetric in IJ.

For CCSD(T), the triples contribution to the energy is estimated perturbatively using the CCSD amplitudes [259, 260]. The perturbative correction accounts for connected triple excitations to fifth order in the fluctuation potential, at a computational cost scaling as $O(N^7)$ rather than the $O(N^8)$ of full CCSDT:

$$E^{CCSD(T)} = E^{CCSD} + \Delta E^{CCSD(T)} \tag{5.22}$$

$$\Delta E^{CCSD(T)} = \sum_{AI} \bar{t}_I^{A*} T_I^A + \sum_{ABIJ} \bar{t}_{IJ}^{AB*} T_{IJ}^{AB} \tag{5.23}$$

where

$$\bar{t}_I^A = 2t_I^A \tag{5.24}$$

$$\bar{t}_{IJ}^{AB} = 4t_{IJ}^{AB} - 2t_{JI}^{AB} \tag{5.25}$$

$${}^*T_I^A = \sum_{CDKL} \left({}^*t_{IKL}^{ACD(2)} - {}^*t_{LKI}^{ACD(2)} \right) L_{KCLD} \tag{5.26}$$

$${}^*T_{IJ}^{AB} = \sum_{CDK} \left({}^*t_{IJK}^{ACD(2)} L_{BCKD} - {}^*t_{KJI}^{ACD(2)} g_{KDBC} \right) - \sum_{CKL} \left({}^*t_{IKL}^{ABC(2)} L_{KJLC} - {}^*t_{LKI}^{ABC(2)} g_{KJLC} \right) \tag{5.27}$$

where

$$L_{PQRS} = 2g_{PQRS} - g_{PSRQ} \tag{5.28}$$

We also depend on the choice of basis set, and expand each electronic orbital as:

$$\phi_i(\mathbf{r}) = \sum_{\mu}^{M} c_{\mu i}\chi_{\mu}(\mathbf{r}) \tag{5.29}$$

One choice is Gaussian-type orbitals (GTOs)[261, 262]:

$$\chi(\mathbf{r}) = r^l e^{-\alpha r^2} Y_L^M(\theta, \phi) \tag{5.30}$$

where l, m, n are integers controlling the angular shape($s, p, d, f, ...$) and α controls the spatial extent. $L = l + m + n$ The advantage of using these, even though they are not the exact shape of atomic orbitals, is practical. The product of two Gaussians on different centers is another Gaussian on a third center, making all two-electron integrals analytically tractable. This is called the Gaussian product theorem.

An alternative is Slater-type orbitals (STOs) [263, 264]:

$$\chi(\mathbf{r}) = r^{n-1} e^{-\zeta r} Y_l^m(\theta, \phi). \tag{5.31}$$

These are the correct asymptotic form of atomic orbitals but the two-electron integrals require numerical quadrature, making them much more expensive.

There are two hierarchies of approximation. The first is the choice of relativistic Hamiltonian, the second is the choice of basis set[265]. After choosing these, we start with the calculation of the Born-Oppenheimer potential. We can directly compare the potentials with different relativistic Hamiltonians. We calculate with progressively larger basis sets, and then extrapolate to the CBS limit [266–268]. We calculated relativistic corrections using the same method [269, 270]. We then fit to an analytic form [271], which is a modified version of a Tang-Toennies potential [272]. We can then solve the radial Schrödinger equation using DVR[207].

We can then solve the nuclear Schrödinger equation to get exact vibrational bound states:

$$[-\frac{\hbar^2}{2\mu}\frac{d^2}{dr^2} + V(r) + \frac{\hbar^2 J(J+1)}{2\mu r^2}]\chi_{v,J} = E_{v,J}\chi_{v,J}(R). \tag{5.32}$$

We can also implement a switching function to fit the short-range to the long-range[273]

5.2.2 Born-Oppenheimer potential results

Relativistic Hamiltonian

There is a hierarchy of relativistic treatments available, which we evaluate in turn. The Douglas-Kroll-Hess method [269, 270] is a two-component method. The Dirac equation is block-diagonalized via unitary transformation to decouple the large and small components of the 4-component spinor. DKH works with regular non-relativistic basis sets recontracted for the DKH Hamiltonian. It only captures scalar relativity, meaning mass-velocity and Darwin terms, but not spin-orbit coupling. DKH truncates the block-diagonalization at a finite order (typically second order, DKH2), applying two successive unitary transformations.

X2C is a more modern two-component approach[274]. Rather than perturbative DKH expansion, X2C performs the exact block-diagonalization of the one-electron Dirac matrix in the chosen basis set, and does the same unitary transformation to infinite order. This makes it formally more complete than DKH at finite order.

Dirac-Coulomb is the full four-component relativistic treatment [275]. Each orbital is a 4-component spinor with large and small components, and the Hamiltonian is the Dirac-Coulomb operator:

$$\hat{H}_{DC} = \sum_i \sum_A \left(c\boldsymbol{\alpha}_i \cdot \hat{\mathbf{p}}_i + \beta_i m_e c^2 - \frac{Z_A}{r_{iA}} \right) + \sum_{i<j} \frac{1}{r_{ij}} \tag{5.33}$$

where α and β are the 4×4 Dirac matrices. This is the most complete option because it includes scalar relativity and spin-orbit exactly. It is more expensive because basis sets must describe both large and small components, the small component basis must satisfy the kinetic balance condition,

and four-component integrals are more costly.

A pseudopotential replaces the 36 core electrons with a fitted potential [276]. Only the two valence electrons per Sr atom are correlated explicitly. The relativistic effects of the core are folded into the ECP parameters at the fitting stage. The advantage is a dramatic reduction in computational cost. "PP-exp CBS" is the pseudopotential extrapolated to the complete basis set limit using the standard $E = E_\infty + AX^{-3}$ formula.

Here we present the results from the calculation of the relativistic potential with the choice of relativistic Hamiltonian (Fig. 5.5).

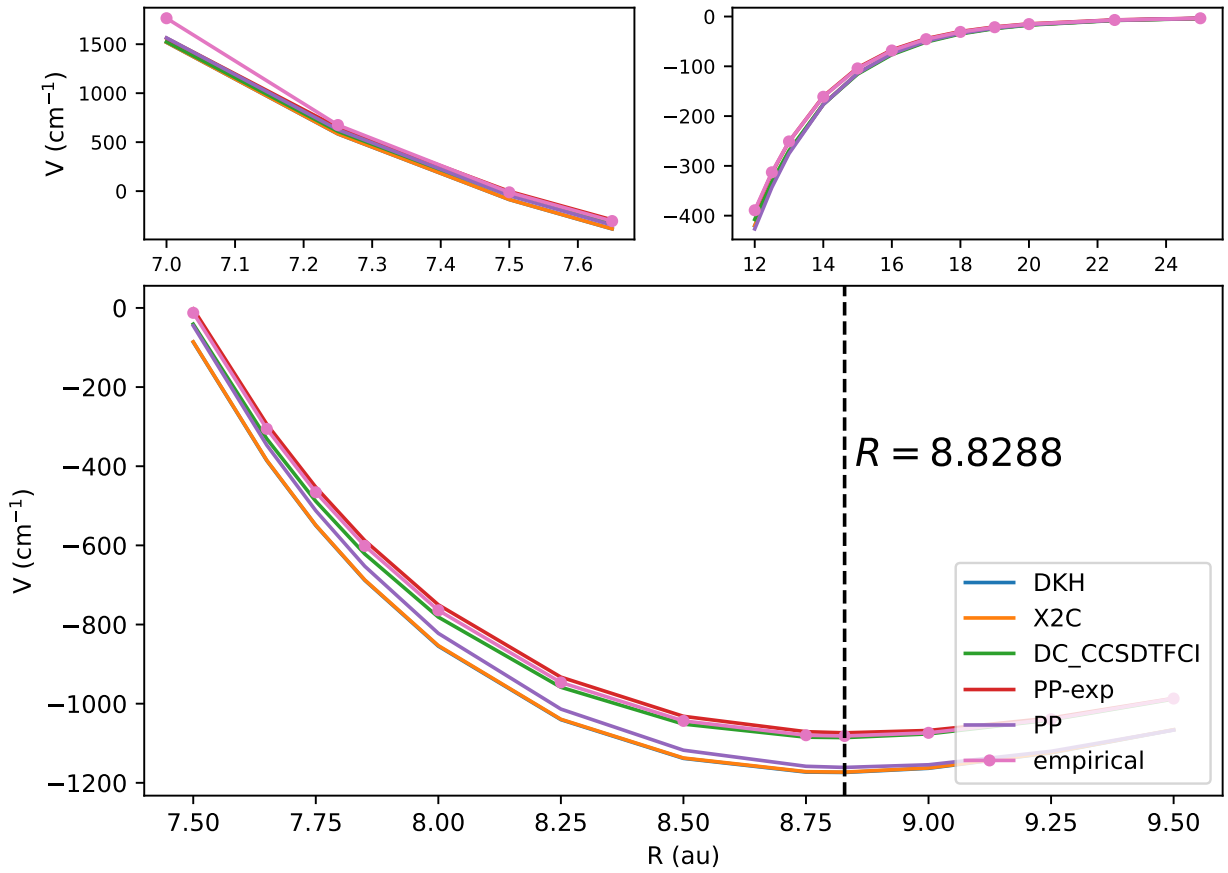

H_{rel}	repulsive	minimum	attractive
DKH	1518.651	−1173.820	−114.349
X2C	1519.383	−1172.893	−114.466
DC	1524.796	−1085.759	−115.771
PP	1564.725	−1161.064	−114.119
PP - exp CBS	1561.709	−1073.649	−102.932
empirical	1765.220	−1081.640	−104.214

Figure 5.5: Convergence of the relativistic potential with the choice of the relativistic Hamiltonian. (Top) Comparison of the full potential curves for each Hamiltonian. (Bottom) Results are presented for three representative distances, repulsive $R = 7$ bohr, minimum $R = 8.8288$ bohr, and attractive $R = 15$ bohr, computed with CCSD(T)+FCI(4e) extrapolated to the complete basis set.

Dirac-Coulomb potential basis set

Here we present results for the convergence of the relativistic Dirac-Coulomb potential with different choice of basis set (Fig. 5.6). We can increase the basis set to progressively more accurate values, at the cost of computational time. As we go to increased Z (ζ), we include more contracted basis functions ϕ per valence orbital. We can extrapolate to the complete basis set using the approximation:

$$E(n) \approx E_{CBS} + \frac{A}{n^3} \tag{5.34}$$

where $n = 2$ for $2Z$, $n = 3$ for $3Z$,...[267]. The correlation energy converges as n^{-3} with cardinal number n for correlation-consistent basis sets

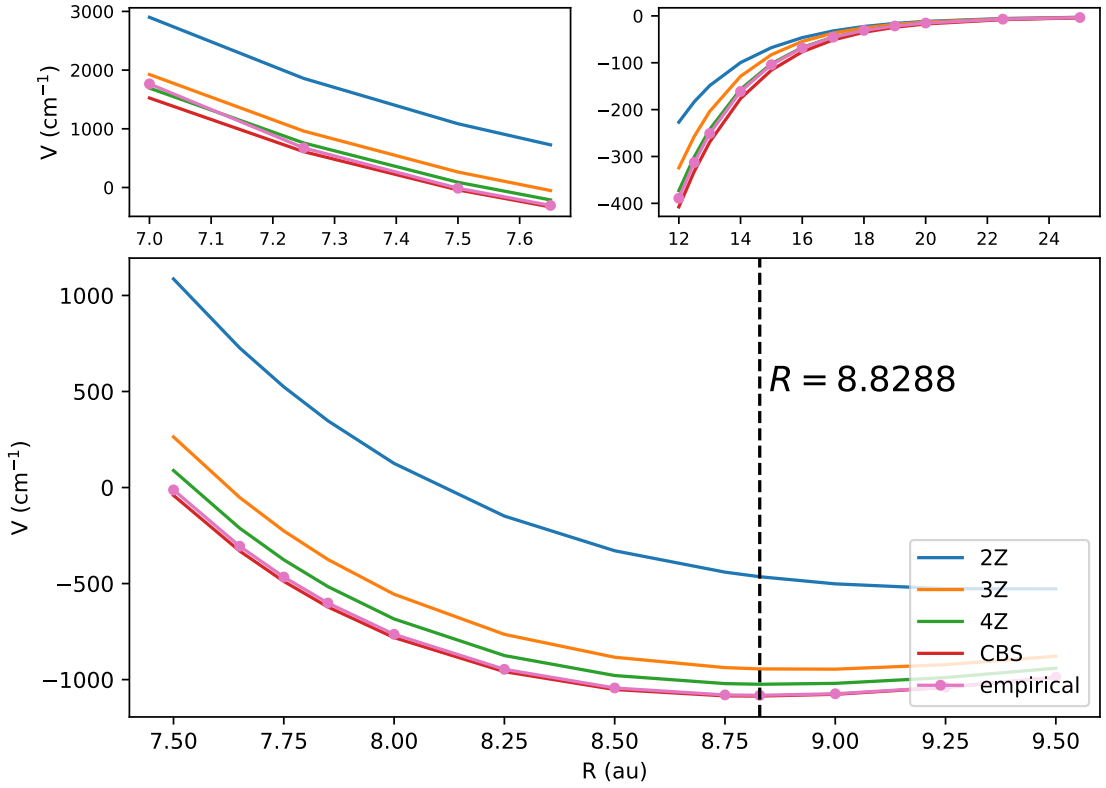

basis set	repulsive	minimum	attractive
2Z	2899.570	−464.348	−67.700
3Z	1925.083	−944.267	−82.744
4Z	1693.400	−1024.258	−101.966
CBS	1524.796	−1085.759	−115.771
empirical	1765.220	−1081.640	−104.214

Figure 5.6: Convergence of the relativistic Dirac-Coulomb potential with the choice of the basis set. (Top) Comparison of the full potential curves for each basis set. (Bottom) Results are presented for three representative distances, repulsive $R = 7$ bohr, minimum $R = 8.8288$ bohr, and attractive $R = 15$ bohr, computed with CCSD(T)+FCI(4e). The results extrapolated to the complete basis set are also shown.

Dirac-Coulomb potential electronic structure method

Here we present convergence of the relativistic Dirac-Coulomb potential with the choice of the electronic structure method (Fig. 5.7). We compare the CCSD calculated exactly, the perturbative CCSD(T), and the inclusion of the full configuration interaction (CI) for the 4 valence electrons. The full CI is used to correct CCSD(T) for missing higher-order excitations. In full CI, all possible Slater determinants consistent with the spin and spatial symmetry of the system are included in the expansion.

Alternatively, we can use the configuration interaction, where we express the wavefunction as a linear combination of many Slater determinants. Configuration interaction accounts for electron correlation by expanding the wavefunction as a linear combination of the Hartree-Fock determinant and determinants representing excitations of electrons from occupied to virtual orbitals.

$$|\mathbf{C}\rangle = \sum_i |i\rangle \tag{5.35}$$

$$E_{CI} = \min_{\mathbf{C}} \frac{\langle \mathbf{C}|\hat{H}|\mathbf{C}\rangle}{\langle \mathbf{C}|\mathbf{C}\rangle} \tag{5.36}$$

$$\mathbf{HC} = E_{CI}\mathbf{C} \tag{5.37}$$

$$|\mathrm{FCI}\rangle = \left(1 + \sum_{AI} \hat{X}_I^A + \sum_{A>B,I>J} \hat{X}_{IJ}^{AB} + \cdots\right)|\mathrm{HF}\rangle \tag{5.38}$$

where

$$\hat{X}_I^A|\mathrm{HF}\rangle = C_I^A a_A^\dagger a_I|\mathrm{HF}\rangle \tag{5.39}$$

$$\hat{X}_{IJ}^{AB}|\mathrm{HF}\rangle = C_{IJ}^{AB} a_A^\dagger a_B^\dagger a_I a_J|\mathrm{HF}\rangle \tag{5.40}$$

where C_{IJ}^{AB} are separately antisymmetric with respect to AB and IJ, and the same applies for C_{IJK}^{ABC}. CI amplitudes are distinct from their CC counterparts because they are variational, while CC amplitudes are not.

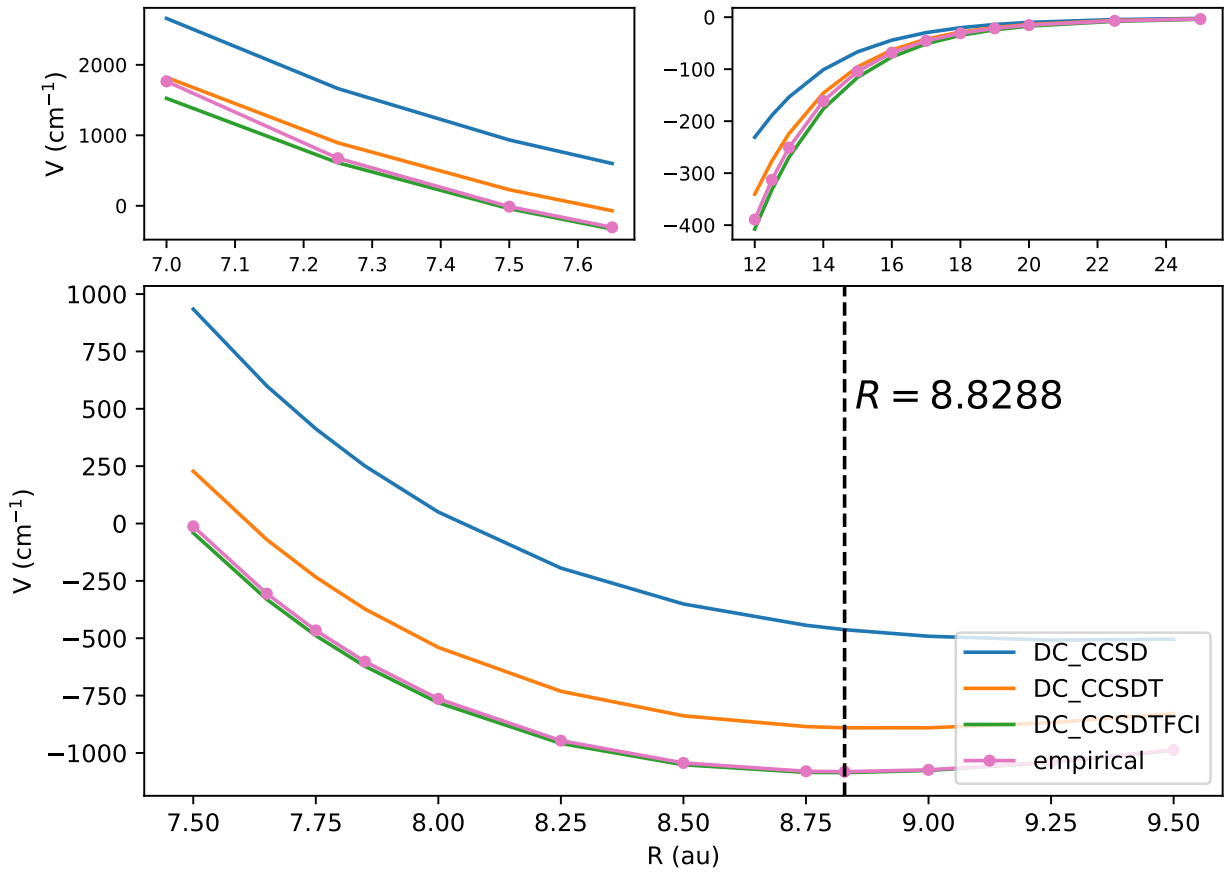

method	repulsive	minimum	attractive
CCSD	2658.601	−462.709	−66.600
CCSD(T)	1822.002	−890.405	−95.525
CCSD(T)+FCI(4e)	1524.796	−1085.759	−115.771
empirical	1765.220	−1081.640	−104.214

Figure 5.7: Convergence of the relativistic Dirac-Coulomb potential with the choice of the electronic structure method. (Top) Comparison of the full potential curves for CCSD, CCSD(T), and CCSD(T)+FCI(4e) extrapolated to the complete basis set limit. (Bottom) Results at three representative distances, repulsive R = 7 bohr, minimum R = 8.8288 bohr, and attractive R = 15 bohr.

5.2.3 NRQED expansion of the potential

Throughout this section, Hartree atomic units are used, i.e. $\hbar = e = m_e = 4\pi\varepsilon_0 = 1$.

Following Ref. [277], the potential energy can be expanded as a power series in fine structure constant α and reduced electron to nuclear mass ratio η as

$$E = E_{BO} + \alpha^2 \left[E_{Breit} + \eta E_{RMD}\right] + \alpha^3 \left[E_{QED} + \eta E_{QED,1}\right]. \tag{5.41}$$

The Dirac-Coulomb hamiltonian is relativistic, and this method is already infinite order in α. The one-electron terms multiplied by α^2 are already included in the BO potential. In our case, these are D1 and P4. Then we have the mass-dependent relativistic and QED terms. All of these terms were computed with the Dirac-Coulomb wavefunction. The orbit-orbit term is quadratic in α, and does not enter the Dirac-Coulomb Hamiltonian.

E_{BO} is the non-relativistic Born-Oppenheimer potential, terms in η are diagonal Born-Oppenheimer and higher adiabatic corrections, terms in α^2 are leading relativistic corrections, and terms in α^3 are leading QED corrections.

The relativistic correction E_{Breit} consists of two-electron Darwin $\langle D_2 \rangle$ and orbit-orbit $\langle OO \rangle$ terms. With the Dirac-Coulomb approach, the mass-velocity $\langle P_4 \rangle$, one-electron Darwin $\langle D_1 \rangle$ terms are included in the Born-Oppenheimer potential. These are defined as follows: the mass-velocity term $\langle P_4 \rangle$ is the leading relativistic correction to the electron's kinetic energy, arising from the relativistic dependence of mass on velocity. The one- and two-electron Darwin terms $\langle D_1 \rangle$ and $\langle D_2 \rangle$ are contact interactions that account for the "smearing out" (Zitterbewegung) of an electron's position, affecting electron-nucleus and electron-electron interactions respectively. The orbit-orbit term $\langle OO \rangle$ describes the magnetic interaction between the motions of the two electrons.

$$E_{Breit} = \langle D_2 \rangle + \langle OO \rangle. \tag{5.42}$$

The results are shown in figure 5.8, where $\langle D_1 \rangle$ and $\langle P_4 \rangle$ are set to zero. As shown in equation 5.41, E_{Breit} is multiplied by α^2. In this case, D2 and B already contain this factor.

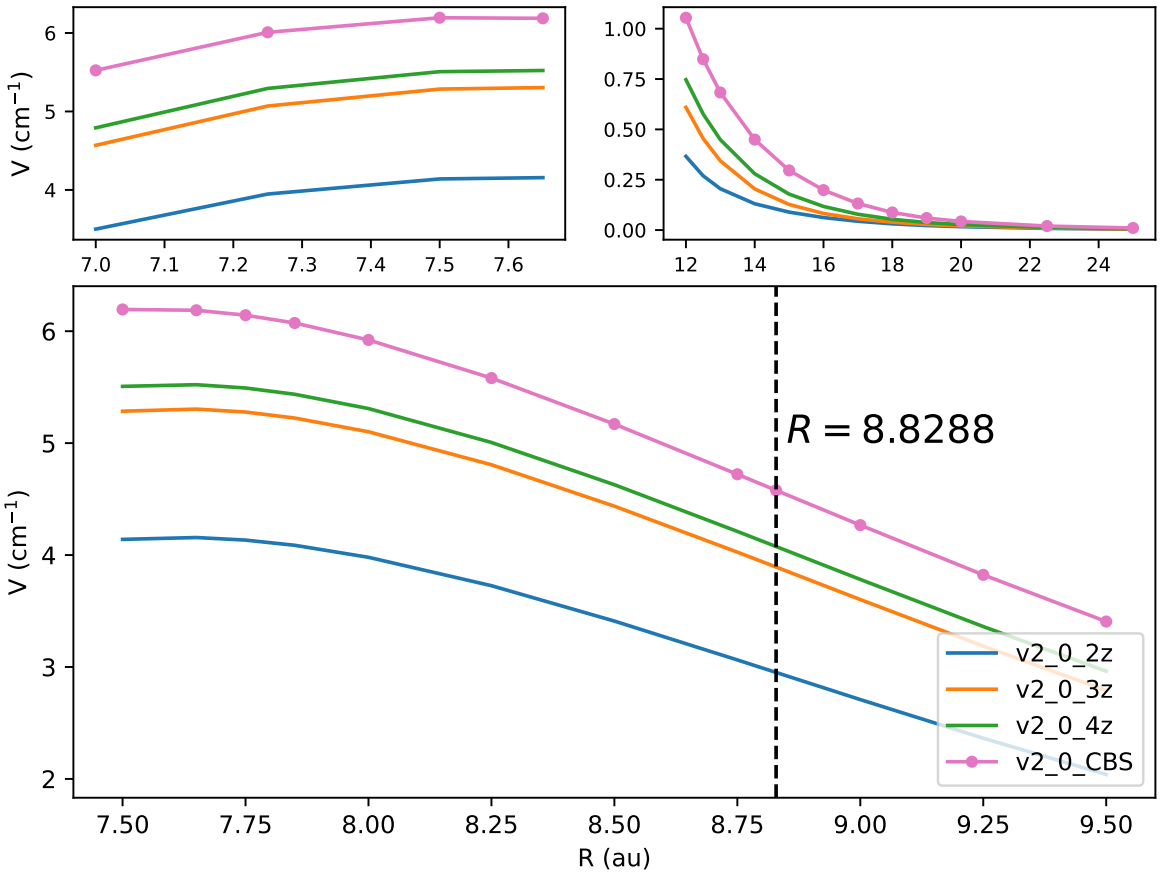

Figure 5.8: Convergence of the relativistic correction E_{Breit} with the choice of the basis set. Results are presented for three representative distances, repulsive, minimum, and attractive, computed with CCSD(T)+FCI(4e). The results extrapolated to the complete basis set are also shown.

The relativistic mass-dependent correction E_{RMD} is a combination of already discussed $\langle P_4 \rangle$, $\langle D_1 \rangle$, $\langle D_2 \rangle$, $\langle OO \rangle$ terms:

$$E_{RMD} = 4\langle P_4 \rangle + 3\left(\langle D_1 \rangle + \langle D_2 \rangle + \langle OO \rangle\right) \tag{5.43}$$

The results are shown for several internuclear distances in figure 5.9. As shown in equation 5.41, E_{RMD} is multiplied by $\eta \cdot \alpha^2$. In this case, D1, D2, P4 and B already contain α^2, so we just need to multiply by η.

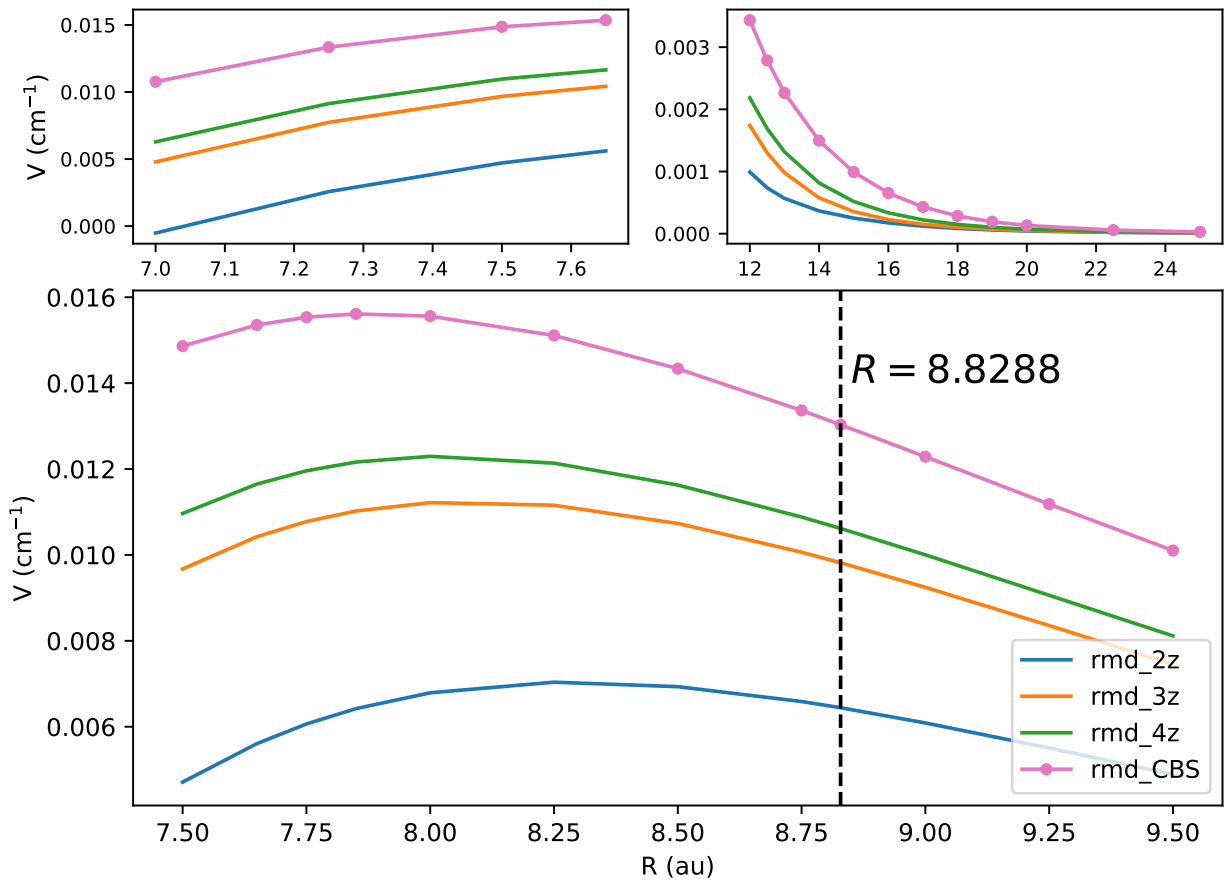

Figure 5.9: Convergence of the relativistic mass-dependent correction E_{RMD} with the choice of the basis set. Results are presented for three representative distances, repulsive, minimum, and attractive, computed with CCSD(T)+FCI(4e). The results extrapolated to the complete basis set are also shown.

The QED correction E_{QED} is given by

$$\frac{8}{3\pi}\left(\frac{19}{30} + \ln(\alpha^{-2}) - \ln(k_0)\right)\langle D_1\rangle + \frac{1}{\pi}\left(\frac{164}{15} + \frac{14}{3}\ln(\alpha)\right)\langle D_2\rangle, \tag{5.44}$$

where $\ln(k_0)$ is Bethe logarithm[278–280]. The results are shown in figure 5.10. As shown in equation 5.41, E_{QED} is multiplied by α^3. In this case, D1 and D2 already contain a factor of α^2, so we just need to multiply by α.

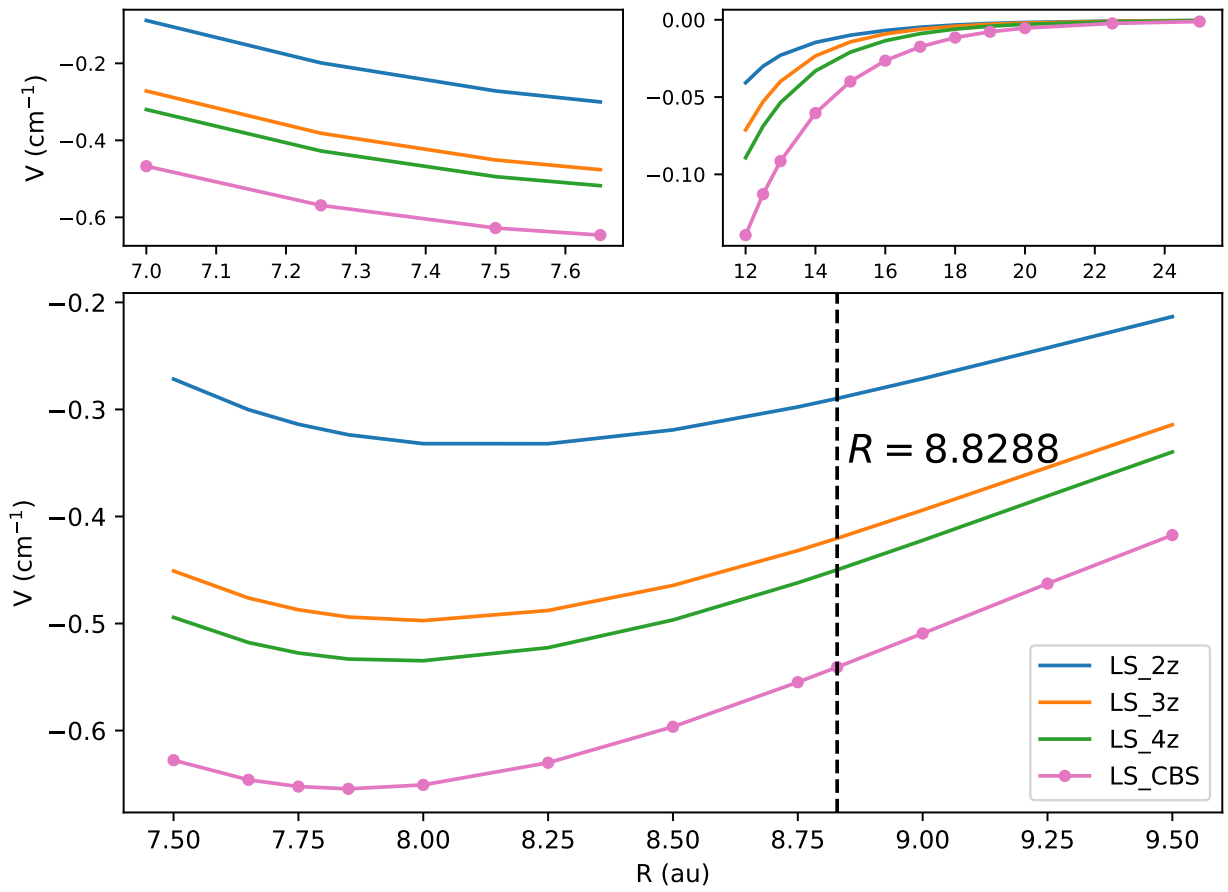

Figure 5.10: Convergence of the QED correction E_{QED} (Lamb shift or 'LS' with the choice of the basis set. Results are presented for three representative distances, repulsive, minimum, and attractive, computed with CCSD(T)+FCI(4e). The results extrapolated to the complete basis set are also shown.

Finally, the QED mass-dependent term $E_{QED,1}$ reads as

$$E_{QED,1} = 3E_{QED} - \frac{2}{3\pi}\langle D_1 \rangle + \frac{14}{3\pi}\langle D_2 \rangle \tag{5.45}$$

The results are shown in figure 5.11. As shown in equation 5.41, $E_{QED,1}$ is multiplied by $\eta \cdot \alpha^3$. In this case, D1 and D2 already contain a factor of α^2, so we just need to multiply by $\eta \cdot \alpha$.

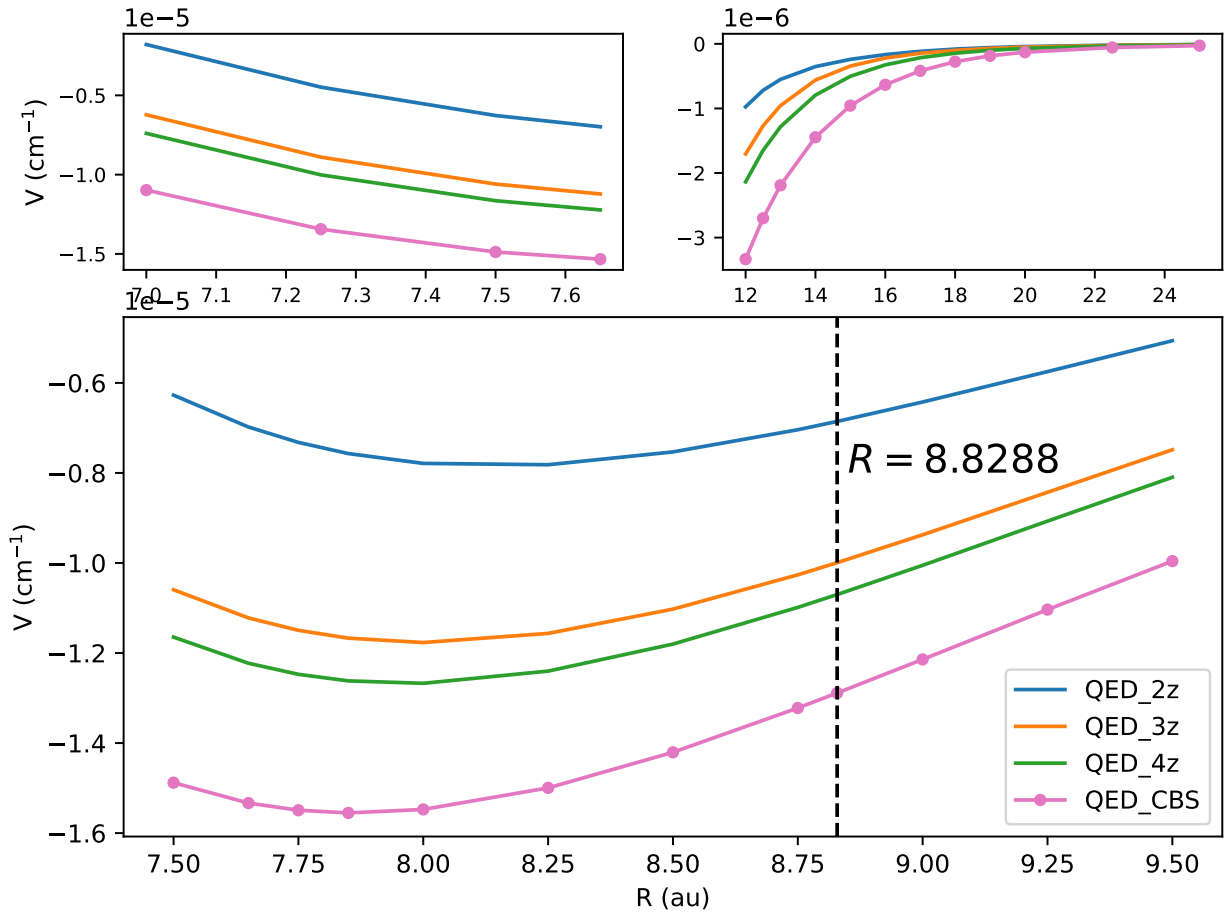

Figure 5.11: Convergence of the QED mass-dependent term $E_{QED,1}$ with the choice of the basis set. Results are presented for three representative distances, repulsive, minimum, and attractive, computed with CCSD(T)+FCI(4e). The results extrapolated to the complete basis set are also shown.

In summary, the full potential through order α^3 and the leading mass-dependent corrections is contructed from the following terms: The Born-Oppenheimer potential E_{BO}, the individual expectation values $\langle D_1 \rangle$, $\langle P_4 \rangle$, $\langle D_2 \rangle$, and $\langle OO \rangle$, the aggregate relativistic corrections E_{Breit} and E_{RMD}, and the QED corrections E_{QED} and $E_{QED,1}$.

Breit term basis set

Here we present convergence of the Breit term (orbit-orbit + D2) with the choice of the basis set (Fig. 5.12).

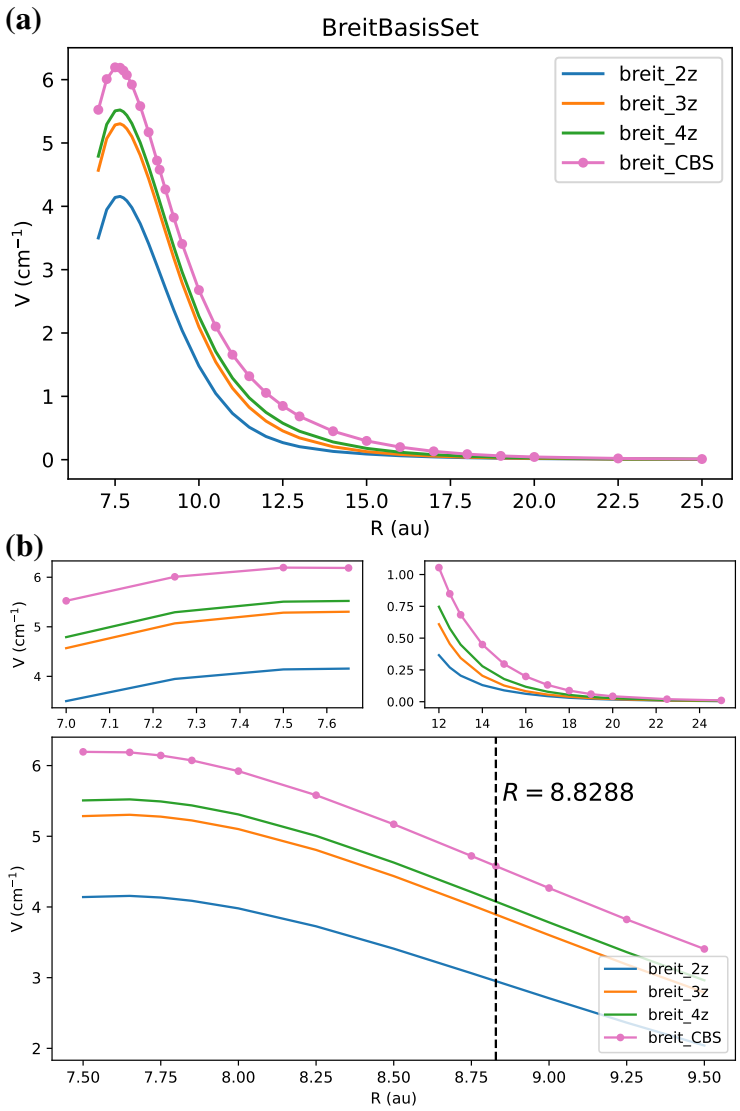

Figure 5.12: Convergence of the Breit term (orbit-orbit + D2) with the choice of the basis set. (a) Comparison of the full potential curves for each basis set. (b) Results are presented for three representative distances, repulsive, minimum, and attractive, computed with CCSD(T)+FCI(4e). The results extrapolated to the complete basis set are also shown.

5.3 Potential fitting

The extrapolated values of $V_{\mathrm{BO}}(R)$, $V_{\mathrm{rel}}(R)$, and $V_{\mathrm{QED}}(R)$ were fitted separately to the analytic functions of the form

$$\sum_{k=1}^{M} e^{-a_k R} \sum_{i=I_0}^{I_1} P_{ik} R^i - \sum_{n=N_0}^{N_1} f_n(\eta R) \frac{C_n}{R^n}, \tag{5.46}$$

where $f_n(x) = 1 - e^{-x}\left(\sum_{i=0}^{n} x^i/i!\right)$ is the Tang–Toennies damping function[281], a_k, P_{ik}, and η are adjustable parameters, and n is always even[282]. The short range portion accounts for the interatomic repulsion at short distances. The physical origin is Pauli repulsion and kinetic energy increase when the electron clouds of the two atoms overlap. The long range terms are determined from the atomic polarizability and they arise from correlated quantum fluctuations in the electron clouds[276]. Instantaneous dipoles on one atom induce fluctuating dipoles on the other, giving an attractive interaction. The damping function helps to smooth between the two regions. η controls the length scale at which the damping becomes important.

Coefficient	
C6	3174.10594229632 $E_h a_0^6$
C8	375462.905868706 $E_h a_0^8$
C10	44564269.5578994 $E_h a_0^{10}$
C12	6176678944.64812 $E_h a_0^{12}$

Table 5.3: Long-range coefficients for the Born-Oppenheimer potential

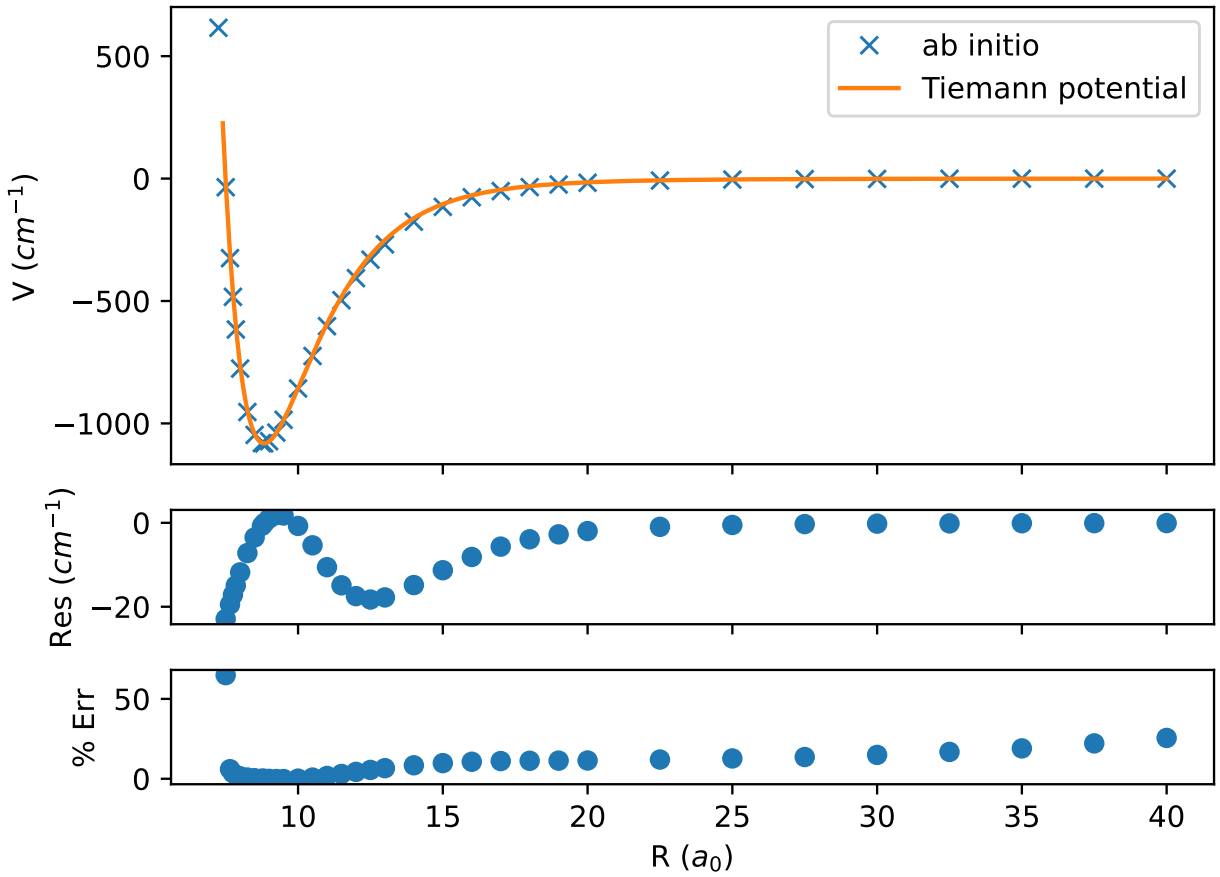

Figure 5.13: Comparison between *ab initio* calculation, including the Born-Oppenheimer potential and the relevant corrections, and a potential fit to Fourier transform spectroscopic data [283]. The residuals and percent error are shown below.

We can directly compare *ab initio* calculations to an empirical potential fit to Fourier transform spectroscopy [283]. We see some discrepancy in the long-range, up to ~ 25% error [Fig. 5.13]. This could indicate some missing physics in the *ab initio* calculation.

Figure 5.14 shows the fit to the full potential, including the BO and BBO terms as shown in equation 5.41. The long-range coefficients are the same as used for the BO potential fit from table 5.3. The summation limits $[M, I_0, I_1, N_0, N_1]$ are [3,-1,2,6,12]. For R > 15 bohr, the potential is replaced with the long-range form without the damping function:

$$-\sum_{n=N_0}^{N_1} \frac{C_n}{R^n}, \tag{5.47}$$

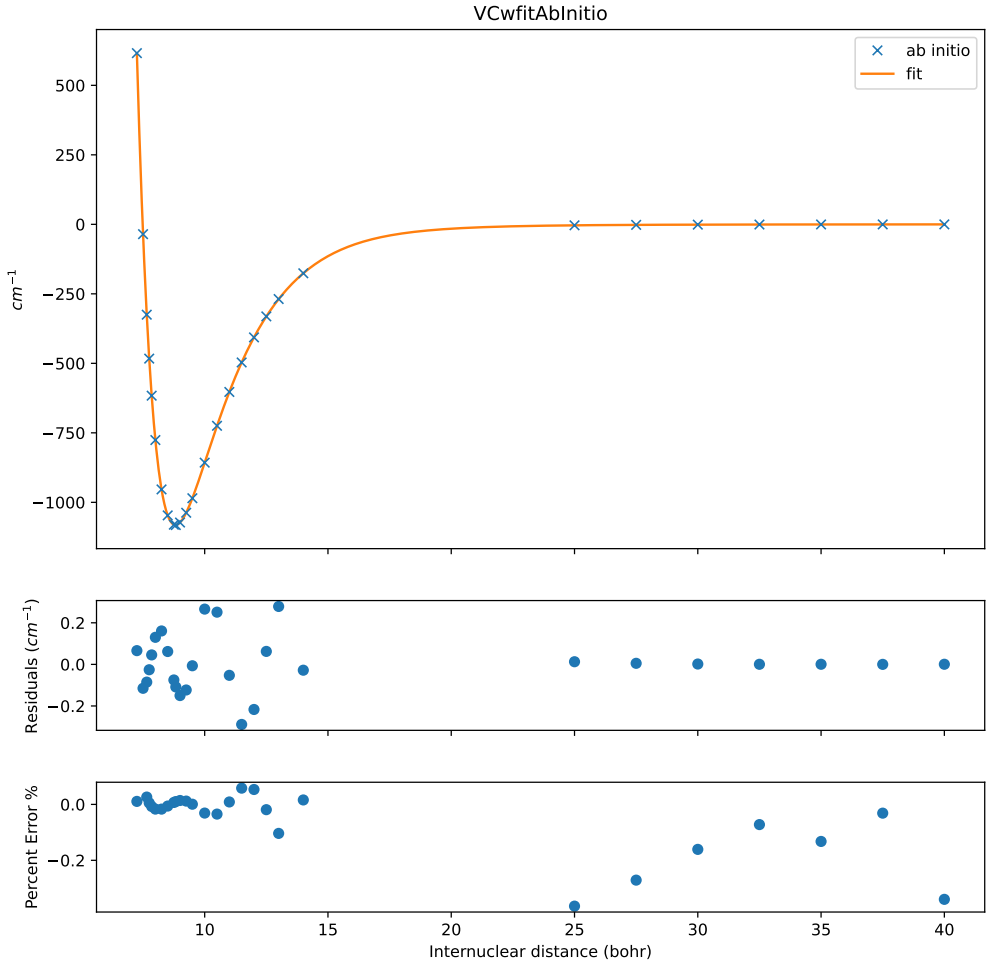

Figure 5.14: Plot of full relativistic potential, including the Born-Oppenheimer and BBO corrections. The fit from eq.5.46 is shown. Below are the residuals (σ_V) and percent error ($\frac{\sigma_V}{V}$).

5.4 Comparison to experimental data

5.4.1 Fitting a potential to binding energies

After fitting the potential to *ab initio* points, we now have an analytical form, and we can directly solve the nuclear portion of the Schrödinger equation and get bound states of the molecular potential. We can then directly compare these to the experimental values to evaluate the *ab initio* performance. The next step is to fit this analytical form to the experimental binding energies to find good agreement. In order to do this, we must have a numerical way of solving the Schrödinger equation.

Two common numerical approaches are available: the Numerov method [284] and the discrete variable representation (DVR) [285]. The Numerov method involves using the boundary conditions from the potential and iterating inwards from both ends, requiring that they match when they meet, in order to find the wavefunction. This is a way of solving a boundary value problem by converting it to an initial value problem. One eigenvalue is found at a time.

The DVR method involves discretizing the Hamiltonian on a grid and diagonalizing it in one shot. Nothing is explicitly propagated and all the eigenvalues are determined simultaneously. DVR constructs the full kinetic energy matrix analytically:

$$\begin{aligned} T_{ii} &= \frac{\hbar^2}{2\mu h^2}\frac{\pi^2}{3} \\ T_{ij} &= \frac{\hbar^2}{2\mu h^2}\frac{2(-1)^{i-j}}{(i-j)^2} \end{aligned} \tag{5.48}$$

The diagonal potential matrix $V_{ij} = V(r_i)\delta_{ij}$ is then constructed from the analytical potential, and after combining with the kinetic energy matrix and diagonalizing, the bound states are determined.

Using this method, and the analytic potential that we fit to *ab initio* points, we can directly solve for the bound states. We directly compare these to experimental spectroscopy of $^{88}Sr_2$ here [Fig.5.15]. We see good agreement in the deeply and weakly bound vibrational states, but some discrepancy in the intermediate portion of the potential.

As a next step, we can also fit to experimentally measured binding energies. Following Ref. [286], we iteratively change parameters, solve the Schrödinger equation, and minimize a cost function. In this case, the cost function is a chi-square:

$$\chi^2 = \sum_i \frac{(K_i - M_i)^2}{\sigma_i^2}, \tag{5.49}$$

Where K_i is the fit value, and M_i is the experimental value, and σ_i are the uncertainties of the measurements. We can take partial derivatives numerically using a centered finite-difference formula:

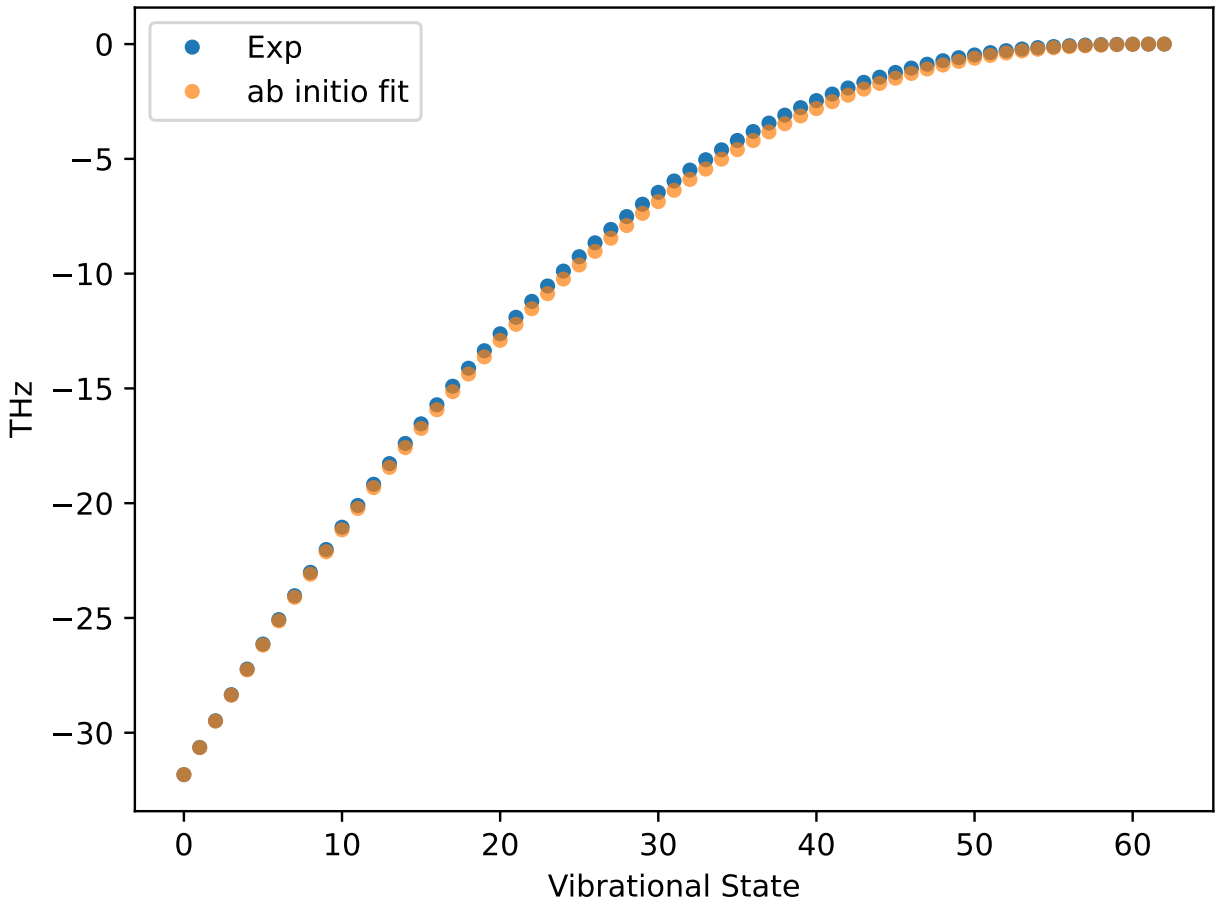

Figure 5.15: Comparison between binding energies calculated from analytic fit to *ab initio* points, and experimentally measured values.

$$\frac{\partial \chi^2}{\partial x_i^{(n)}} \approx \frac{\chi^2\left((1+\varepsilon)x_i^{(n)}\right) - \chi^2\left((1-\varepsilon)x_i^{(n)}\right)}{2\varepsilon x_i^{(n)}} \tag{5.50}$$

where x_i is a parameter, n is the step of the descent, and ε is a small step, typically on the order 10^{-6}. We stop fitting when $|\nabla\chi^2|$ is less than 10^{-3}.

We use a gradient descent algorithm. We assume that the direction of steepest descent of some function f is given by $-\nabla f(x)$. We can iteratively update x to converge to a value that minimizes f. We can vary the step size γ using the Barzilai-Borwein formula [287].

$$\gamma \to L_n = \frac{|(x_n - x_{n-1}) \cdot (\nabla f(x_n) - \nabla f(x_{n-1}))|}{||\nabla f(x_n) - \nabla f(x_{n-1})||^2} \tag{5.51}$$

This adaptive step size accelerates convergence: large steps are taken on shallow slopes, and small steps on steep ones. Near a minimum, the gradient ∇f changes direction between successive steps, reducing the numerator of the Barzilai-Borwein formula and naturally producing a smaller step size. Using this method, we can fit the parameters of a potential to bound states.

5.4.2 Casimir-Polder interaction

The long-range form of $X0_g^+$ potential including the retardation effects can be written as [237, 288–292]

$$E_{BO,\mathrm{LR}} = -\frac{C_6 f_6(R)}{R^6} - \frac{C_8 f_6(R)}{R^8} + \ldots \tag{5.52}$$

The lowest-order retardation function f_6 is given by

$$f_6(R) = \frac{1}{\pi C_6} \int_0^\infty d\omega\, e^{-2\alpha\omega R}\, P_{11}(\omega\alpha R)\, \alpha_1^2(i\omega), \tag{5.53}$$

where $P_{11}(x) = x^4 + 2x^3 + 5x^2 + 6x + 3$ and $\alpha_1(i\omega)$ is the electric dipole polarizability.

At small R, $V_{CP}(R)$ behaves as $-C_6R^{-6} + O(\alpha^2)$[293]. The retardation correction to the BO potential is

$$\delta V_{ret}^{BO}(R) = V_{CP}(R) + C_6 R^{-6}. \tag{5.54}$$

This is equivalent to the replacement of the $-C_6R^{-6}$ component of the nonrelativistic potential by $-g(R)C_6R^{-6}$, where $g(R)$ is the retardation factor [294, 295]

$$g(R) = -V_{CP}(R)\frac{R^6}{C_6} \tag{5.55}$$

For small R (but still larger than the sum of the atomic radii) the retardation function can be expanded as

$$f_6(R) \approx 1 - \frac{\alpha^2 R^2 W_4}{C_6} - \frac{\alpha^3 R^3 W_3}{C_6}. \tag{5.56}$$

The term including W_4, proportional to α^2 is the leading asymptotic term of E_{Breit}, or of $\langle OO \rangle$ since $\langle D_1 \rangle$, $\langle D_2 \rangle$ and $\langle P_4 \rangle$ all decay as R^{-6}. Similarly, W_3 is the leading order coefficient in the small R expansion of E_{QED}, or of Araki-Sucher correction.

For large R, the retardation function f_6 behaves as

$$f_6 \xrightarrow{R\to\infty} \frac{23}{4\pi\alpha R}\frac{\alpha_1^2(0)}{C_6}. \tag{5.57}$$

As a result, the potential decays with R^{-7}, as was derived by Casimir and Polder in Ref. [236].

To test whether Casimir-Polder retardation is essential for describing the halo state, we will fit the combined theoretical potential to the experimental binding energies under two scenarios: (i) excluding the halo-state binding energy from the fit, and (ii) including it. Comparing the quality of fit in each case, and the variation in the fitted molecular size, determines whether retardation is required to reproduce the halo-state energy. This analysis is in progress.

5.5 Summary

We have performed spectroscopy of the full $X^1\Sigma_g^+$ ground-state potential in $^{86}Sr_2$. Using the previously measured binding energies for the $^{88}Sr_2$ molecule, we can examine the isotope shift

of all 63 vibrational states. This is a novel exploration of the potential. Our collaborators have performed a cutting-edge *ab initio* calculation of the full molecular potential of Sr_2, including full Born-Oppenheimer potential and the smaller beyond-Born-Oppenheimer relativistic corrections. To enable direct comparison with experiment, we fit an analytical form to the discrete *ab initio* points and then solve the nuclear Schrödinger equation to obtain predicted bound-state energies. Comparison of these predictions with our measured binding energies allows us to evaluate the *ab initio* calculations and iteratively refine the potential parameters. We also explore the long-range portion of the potential, especially the dependence of the halo-state binding energy on the Casimir-Polder interaction, by fitting to the entire potential.

Outlook

Here, we combine optical lattice clock techniques with insights from molecular physics to develop a novel metrological tool and to refine our understanding of interatomic forces. As a metrological instrument, Sr_2 complements atomic clocks by using a vibrational resonator rather than an electronic one, placing its frequency in a regime distinct from existing microwave and optical atomic clocks. With our improved understanding of the BBR shift and ongoing experimental upgrades, there is a clear path towards improving clock precision by several orders of magnitude. As with many precision spectroscopy experiments, the central goal is to increase coherence time, in our case by extending the clock-state lifetimes. The molecular clock remains early in its development, and we expect rapid progress in the coming years.

Sr_2 also functions as a precise nm-scale interatomic force sensor, providing a valuable testbed for combining quantum chemistry theory with experiment. By comparing *ab initio* calculations that incorporate known interactions to experimental measurements, we can refine both our chemistry models and our understanding of the underlying physics. Any disagreement between the two could be a signature of new physics. The halo state in $^{86}Sr_2$, in particular, is a sensitive probe of long-range interatomic phenomena, including the retardation of the electromagnetic interaction.

References

[1] J. Jespersen and J. Fitz-Randolph, *From Sundials to Atomic Clocks* (Monograph 155). National Institute of Standards and Technology, 1999.

[2] F. Walls and J. Vig, "Fundamental limits on the frequency stabilities of crystal oscillators," *IEEE Transactions on Ultrasonics, Ferroelectrics, and Frequency Control*, vol. 42, no. 4, pp. 576–589, Jul. 1995.

[3] J. R. Vig, "Quartz crystal oscillators and resonators," Army Research Laboratory, Tech. Rep. SLCET-TR-88-1, 1999.

[4] D. Sullivan, "Time and frequency measurement at NIST: The first 100 years," in *Proceedings of the 2001 IEEE International Frequency Control Symposium and PDA Exhibition*, 2001.

[5] A. D. Ludlow, M. M. Boyd, J. Ye, E. Peik, and P. O. Schmidt, "Optical atomic clocks," *Reviews of Modern Physics*, vol. 87, no. 2, pp. 637–701, Jun. 2015.

[6] I. I. Rabi, S. Millman, P. Kusch, and J. R. Zacharias, "The molecular beam resonance method for measuring nuclear magnetic moments," *Phys. Rev.*, vol. 55, pp. 526–535, 1939.

[7] N. F. Ramsey, "A new molecular beam resonance method," *Phys. Rev.*, vol. 78, pp. 695–696, 1950.

[8] L. Essen and J. V. L. Parry, "An atomic standard of frequency and time interval," *Nature*, vol. 176, pp. 280–282, 1955.

[9] T. Udem, J. Reichert, R. Holzwarth, and T. W. Hänsch, "Absolute optical frequency measurement of the cesium D1 line with a mode-locked laser," *Phys. Rev. Lett.*, vol. 82, pp. 3568–3571, 1999.

[10] S. A. Diddams et al., "Direct link between microwave and optical frequencies with a 300 THz femtosecond laser comb," *Phys. Rev. Lett.*, vol. 84, pp. 5102–5105, 2000.

[11] J. Stenger, H. Schnatz, C. Tamm, and H. R. Telle, "Ultraprecise measurement of optical frequency ratios," *Phys. Rev. Lett.*, vol. 88, p. 073 601, 2002.

[12] S. T. Cundiff and J. Ye, "Colloquium: Femtosecond optical frequency combs," *Rev. Mod. Phys.*, vol. 75, pp. 325–342, 2003.

[13] L. Hollberg, S. Diddams, A. Bartels, T. Fortier, and K. Kim, "The measurement of optical frequencies," *Metrologia*, vol. 42, S105–S124, 2005.

[14] J. Ye and S. T. Cundiff, Eds., *Femtosecond Optical Frequency Comb: Principle, Operation, and Applications*. Boston, MA: Springer, 2005.

[15] J. L. Hall, "Nobel lecture: Defining and measuring optical frequencies," *Rev. Mod. Phys.*, vol. 78, pp. 1279–1295, 2006.

[16] T. W. Hänsch, "Nobel lecture: Passion for precision," *Rev. Mod. Phys.*, vol. 78, pp. 1297–1309, 2006.

[17] G. Grosche, B. Lipphardt, and H. Schnatz, "Optical frequency synthesis and measurement using fibre-based femtosecond lasers," *Eur. Phys. J. D*, vol. 48, pp. 27–33, 2008.

[18] T. R. Schibli et al., "Optical frequency comb with submillihertz linewidth and more than 10 w average power," *Nat. Photonics*, vol. 2, pp. 355–359, 2008.

[19] H. Katori, "Spectroscopy of strontium atoms in the lamb-dicke confinement," in *Proceedings of the 6th Symposium on Frequency Standards and Metrology*, P. Gill, Ed., Singapore: World Scientific, 2002, pp. 323–330.

[20] H. Katori, M. Takamoto, V. G. Pal'chikov, and V. D. Ovsiannikov, "Ultrastable optical clock with neutral atoms in an engineered light shift trap," *Phys. Rev. Lett.*, vol. 91, p. 173 005, 2003.

[21] M. Takamoto, F.-L. Hong, R. Higashi, and H. Katori, "An optical lattice clock," *Nature*, vol. 435, no. 7040, pp. 321–324, 2005.

[22] M. Takamoto and H. Katori, "Spectroscopy of the $^1S_0$–$^3P_0$ clock transition of ^{87}Sr in an optical lattice," *Phys. Rev. Lett.*, vol. 91, p. 223 001, 2003.

[23] A. D. Ludlow et al., "Systematic study of the ^{87}Sr clock transition in an optical lattice," *Phys. Rev. Lett.*, vol. 96, p. 033 003, 3 2006.

[24] R. Le Targat et al., "Accurate optical lattice clock with ^{87}Sr atoms," *Phys. Rev. Lett.*, vol. 97, p. 130 801, 2006.

[25] A. Derevianko and H. Katori, "Colloquium: Physics of optical lattice clocks," *Rev. Mod. Phys.*, vol. 83, pp. 331–347, 2011.

[26] J. Levine, "Introduction to time and frequency metrology," *Review of Scientific Instruments*, vol. 70, no. 6, pp. 2567–2596, Jun. 1999.

[27] F. G. Major, *The Quantum Beat: Principles and Applications of Atomic Clocks*. New York: Springer, 2007.

[28] M. S. Grewal, A. P. Andrews, and C. G. Bartone, *Global Navigation Satellite Systems, Inertial Navigation, and Integration*. New York: John Wiley & Sons, 2013.

[29] E. Kaplan and C. Hegarty, *Understanding GPS: Principles and Applications*. Norwood, MA: Artech House Publishers, 2006.

[30] G. S. Rao, *Global Navigation Satellite Systems*. New Delhi: Tata McGraw-Hill Education, 2010.

[31] T. Bothwell et al., "Resolving the gravitational redshift across a millimetre-scale atomic sample," *Nature*, vol. 602, no. 7897, pp. 420–424, Feb. 2022.

[32] W. F. McGrew et al., "Atomic clock performance enabling geodesy below the centimetre level," *Nature*, vol. 564, no. 7734, pp. 87–90, Dec. 2018.

[33] M. S. Safronova, D. Budker, D. DeMille, D. F. J. Kimball, A. Derevianko, and C. W. Clark, "Search for New Physics with Atoms and Molecules," 2017.

[34] S. Kolkowitz, I. Pikovski, N. Langellier, M. D. Lukin, R. L. Walsworth, and J. Ye, "Gravitational wave detection with optical lattice atomic clocks," *Phys. Rev. D*, vol. 94, p. 124 043, 2016.

[35] Y. V. Stadnik and V. V. Flambaum, "Improved limits on interactions of low-mass spin-0 dark matter from atomic clock spectroscopy," *Phys. Rev. A*, vol. 94, p. 022 111, 2016.

[36] A. Derevianko and M. Pospelov, "Hunting for topological dark matter with atomic clocks," *Nature Physics*, vol. 10, no. 12, pp. 933–936, 2014.

[37] A. Arvanitaki, J. Huang, and K. Van Tilburg, "Searching for dilaton dark matter with atomic clocks," *Physical Review D*, vol. 91, no. 1, p. 015 015, 2015.

[38] P. Wcisło et al., "New bounds on dark matter coupling from a global network of optical atomic clocks," *Science Advances*, vol. 4, no. 12, eaau4869, 2018.

[39] C. J. Kennedy et al., "Precision metrology meets cosmology: Improved constraints on ultralight dark matter from atom-cavity frequency comparisons," *Phys. Rev. Lett.*, vol. 125, p. 201 302, 2020.

[40] M. J. Martin et al., "A Quantum Many-Body Spin System in an Optical Lattice Clock," *Science*, vol. 341, pp. 632–636, 2013.

[41] A. Rey et al., "Probing many-body interactions in an optical lattice clock," *Annals of Physics*, vol. 340, pp. 311–351, 2014.

[42] A. V. Gorshkov et al., "Two-orbital SU(N) magnetism with ultracold alkaline-earth atoms," *Nat. Phys.*, vol. 6, pp. 289–295, 2010.

[43] G. Cappellini et al., "Direct observation of coherent interorbital spin-exchange dynamics," *Physical Review Letters*, vol. 113, no. 12, pp. 1–5, 2014.

[44] F. Scazza, C. Hofrichter, M. Höfer, P. C. De Groot, I. Bloch, and S. Fölling, "Observation of two-orbital spin-exchange interactions with ultracold SU(N)-symmetric fermions," *Nat. Phys.*, vol. 10, pp. 779–784, 2014.

[45] X Zhang et al., "Spectroscopic observation of SU(N)-symmetric interactions in Sr orbital magnetism," *Science*, vol. 345, no. 6203, pp. 1467–1473, 2014.

[46] W. R. Milner et al., *Coherent evolution of superexchange interaction in seconds long optical clock spectroscopy*, Feb. 2024. arXiv: 2402.13398 [cond-mat, physics:physics].

[47] A. Aeppli et al., "Hamiltonian engineering of spin-orbit coupled fermions in a Wannier-Stark optical lattice clock," *arXiv:2201.05909 [cond-mat, physics:physics]*, Jan. 2022. arXiv: 2201.05909 [cond-mat, physics:physics].

[48] C. Sanner, L. Sonderhouse, R. B. Hutson, L. Yan, W. R. Milner, and J. Ye, "Pauli blocking of atom-light scattering,"

[49] L. Sonderhouse et al., "Thermodynamics of a deeply degenerate SU(N)-symmetric Fermi gas," *Nature Physics*, vol. 16, no. 12, pp. 1216–1221, Dec. 2020.

[50] A. Goban et al., "Emergence of multi-body interactions in a fermionic lattice clock," *Nature*, vol. 563, no. 7731, pp. 369–373, Nov. 2018.

[51] J. M. Robinson et al., *Direct comparison of two spin squeezed optical clocks below the quantum projection noise limit*, Nov. 2022. arXiv: 2211.08621 [physics, physics:quant-ph].

[52] W. J. Eckner et al., *Realizing spin squeezing with Rydberg interactions in a programmable optical clock*, Mar. 2023. arXiv: 2303.08078 [cond-mat, physics:physics, physics:quant-ph].

[53] P. He et al., "Engineering spin squeezing in a 3D optical lattice with interacting spin-orbit-coupled fermions," *Physical Review Research*, vol. 1, no. 3, p. 033 075, Nov. 2019.

[54] M. S. Safronova, D. Budker, D. DeMille, D. F. J. Kimball, A. Derevianko, and C. W. Clark, "Search for new physics with atoms and molecules," *Reviews of Modern Physics*, vol. 90, no. 2, p. 025 008, Jun. 2018.

[55] R. M. Godun et al., "Frequency Ratio of Two Optical Clock Transitions in Yb + 171 and Constraints on the Time Variation of Fundamental Constants," *Physical Review Letters*, vol. 113, no. 21, p. 210 801, Nov. 2014.

[56] N. Leefer, C. T. M. Weber, A. Cingöz, J. R. Torgerson, and D. Budker, "New Limits on Variation of the Fine-Structure Constant Using Atomic Dysprosium," *Physical Review Letters*, vol. 111, no. 6, p. 060 801, Aug. 2013.

[57] T. Rosenband et al., "Frequency Ratio of Al^+ and Hg^+ Single-Ion Optical Clocks; Metrology at the 17th Decimal Place," *Science*, vol. 319, no. 5871, pp. 1808–1812, Mar. 2008.

[58] J. Guéna et al., "Improved Tests of Local Position Invariance Using Rb 87 and Cs 133 Fountains," *Physical Review Letters*, vol. 109, no. 8, p. 080 801, Aug. 2012.

[59] V. V. Flambaum and V. A. Dzuba, "Search for variation of the fundamental constants in atomic, molecular, and nuclear spectra," *Canadian Journal of Physics*, vol. 87, no. 1, pp. 25–33, Jan. 2009.

[60] D. Meiser, J. Ye, D. R. Carlson, and M. J. Holland, "Prospects for a millihertz-linewidth laser," *Physical Review Letters*, vol. 102, no. 16, pp. 1–4, 2009.

[61] J. G. Bohnet, Z. Chen, J. M. Weiner, D. Meiser, M. J. Holland, and J. K. Thompson, "A steady-state superradiant laser with less than one intracavity photon," *Nature*, vol. 484, no. 7392, pp. 78–81, 2012.

[62] M. A. Norcia, M. N. Winchester, J. R. K. Cline, and J. K. Thompson, "Superradiance on the milliHertz linewidth strontium clock transition," *ArXiv*, vol. arXiv:1603, pp. 37–40, 2016.

[63] M. A. Norcia and J. K. Thompson, "Cold-strontium laser in the superradiant crossover regime," *Phys. Rev. X*, vol. 6, p. 011 025, 2016.

[64] H. Liu et al., "The development of active optical clocks," *AAPPS Bull.*, vol. 33, p. 10, 2023.

[65] L. von der Wense et al., "Direct detection of the ^{229}Th nuclear clock transition," *Nature*, vol. 533, pp. 47–51, 2016.

[66] B. Seiferle et al., "Energy of the ^{229}Th nuclear clock transition," *Nature*, vol. 573, pp. 243–246, 2019.

[67] S. Kraemer et al., "Observation of the radiative decay of the ^{229}Th nuclear clock isomer," *Nature*, vol. 617, pp. 706–710, 2023.

[68] J. Tiedau et al., "Laser excitation of the Th-229 nucleus," *Phys. Rev. Lett.*, vol. 132, p. 182 501, 2024.

[69] R. Elwell et al., "Laser excitation of the ^{229}Th nuclear isomeric transition in a solid-state host," *Phys. Rev. Lett.*, vol. 133, p. 013 201, 2024.

[70] C. Zhang et al., "Frequency ratio of the ^{229m}Th nuclear isomeric transition and the ^{87}Sr atomic clock," *Nature*, vol. 633, pp. 63–70, 2024.

[71] K. Beeks, T. Sikorsky, T. Schumm, J. Thielking, M. V. Okhapkin, and E. Peik, "The thorium-229 low-energy isomer and the nuclear clock," *Nat. Rev. Phys.*, vol. 3, pp. 238–248, 2021.

[72] J. F. Barry, D. J. McCarron, E. B. Norrgard, M. H. Steinecker, and D. DeMille, "Magneto-optical trapping of a diatomic molecule," *Nature*, vol. 512, no. 7514, pp. 286–289, Aug. 2014.

[73] N. B. Vilas et al., "Magneto-optical trapping and sub-Doppler cooling of a polyatomic molecule," *Nature*, vol. 606, no. 7912, pp. 70–74, Jun. 2022.

[74] S. Truppe et al., "Molecules cooled below the Doppler limit," *Nature Physics*, vol. 13, no. 12, pp. 1173–1176, Dec. 2017.

[75] J. Dai, B. Riley, Q. Sun, D. Mitra, and T. Zelevinsky, *Magneto-Optical Trapping of a Metal Hydride Molecule*, Dec. 2025. arXiv: 2512.22350 [physics].

[76] L. Anderegg et al., "Radio Frequency Magneto-Optical Trapping of CaF with High Density," *Physical Review Letters*, vol. 119, no. 10, p. 103 201, Sep. 2017.

[77] A. L. Collopy et al., "3D Magneto-Optical Trap of Yttrium Monoxide," *Physical Review Letters*, vol. 121, no. 21, p. 213 201, Nov. 2018.

[78] Z. Zeng, S. Deng, S. Yang, and B. Yan, *Three-dimensional Magneto-optical Trapping of Barium Monofluoride*, May 2024. arXiv: 2405.17883 [physics].

[79] Z. D. Lasner et al., "Magneto-Optical Trapping of a Heavy Polyatomic Molecule for Precision Measurement," *Physical Review Letters*, vol. 134, no. 8, p. 083 401, Feb. 2025.

[80] J. E. Padilla-Castillo et al., "Magneto-Optical Trapping of Aluminum Monofluoride," *Physical Review Letters*, vol. 135, no. 24, p. 243 401, Dec. 2025.

[81] C. Chin, R. Grimm, P. Julienne, and E. Tiesinga, "Feshbach resonances in ultracold gases," *Reviews of Modern Physics*, vol. 82, no. 2, pp. 1225–1286, Apr. 2010.

[82] T. Köhler, K. Góral, and P. S. Julienne, "Production of cold molecules via magnetically tunable Feshbach resonances," *Reviews of Modern Physics*, vol. 78, no. 4, pp. 1311–1361, Dec. 2006.

[83] S. Inouye, M. R. Andrews, J. Stenger, H.-J. Miesner, D. M. Stamper-Kurn, and W. Ketterle, "Observation of Feshbach resonances in a Bose–Einstein condensate," *Nature*, vol. 392, no. 6672, pp. 151–154, Mar. 1998.

[84] K. M. Jones, E. Tiesinga, P. D. Lett, and P. S. Julienne, "Ultracold photoassociation spectroscopy: Long-range molecules and atomic scattering," *Reviews of Modern Physics*, vol. 78, no. 2, pp. 483–535, May 2006.

[85] G. Reinaudi, C. B. Osborn, M. McDonald, S. Kotochigova, and T. Zelevinsky, "Optical Production of Stable Ultracold Sr 2 88 Molecules," *Physical Review Letters*, vol. 109, no. 11, p. 115 303, Sep. 2012.

[86] T Zelevinsky et al., "Narrow Line Photoassociation in an Optical Lattice," *Physical Review Letters*, vol. 96, no. 20, p. 203 201, 2006.

[87] H. R. Thorsheim, J. Weiner, and P. S. Julienne, "Laser-induced photoassociation of ultracold sodium atoms," *Physical Review Letters*, vol. 58, no. 23, pp. 2420–2423, Jun. 1987.

[88] J. D. Miller, R. A. Cline, and D. J. Heinzen, "Photoassociation spectrum of ultracold Rb atoms," *Physical Review Letters*, vol. 71, no. 14, pp. 2204–2207, Oct. 1993.

[89] P. D. Lett, K. Helmerson, W. D. Phillips, L. P. Ratliff, S. L. Rolston, and M. E. Wagshul, "Spectroscopy of Na 2 by photoassociation of laser-cooled Na," *Physical Review Letters*, vol. 71, no. 14, pp. 2200–2203, Oct. 1993.

[90] D. K. Ruttley et al., *Formation of ultracold molecules by merging optical tweezers*, Feb. 2023. arXiv: 2302.07296 [physics].

[91] R. C. Bird and J. M. Hutson, "Making molecules by mergoassociation: The role of center-of-mass motion," *Physical Review Research*, vol. 7, no. 3, p. 033 022, Jul. 2025.

[92] R. Stock, I. H. Deutsch, and E. L. Bolda, "Quantum State Control via Trap-Induced Shape Resonance in Ultracold Atomic Collisions," *Physical Review Letters*, vol. 91, no. 18, p. 183 201, Oct. 2003.

[93] M. Krych and Z. Idziaszek, "Controlled collisions of two ultracold atoms in separate harmonic traps," *Physical Review A*, vol. 80, no. 2, p. 022 710, Aug. 2009.

[94] D. Capecchi et al., "Observation of Confinement-Induced Resonances in a 3D Lattice," *Physical Review Letters*, vol. 131, no. 21, p. 213 002, Nov. 2023.

[95] S. Sala and A. Saenz, "Theory of inelastic confinement-induced resonances due to the coupling of center-of-mass and relative motion," *Physical Review A*, vol. 94, no. 2, p. 022 713, Aug. 2016.

[96] H. Moritz, T. Stöferle, K. Günter, M. Köhl, and T. Esslinger, "Confinement Induced Molecules in a 1D Fermi Gas," *Physical Review Letters*, vol. 94, no. 21, p. 210 401, Jun. 2005.

[97] L. Oghittu et al., "Confinement-induced resonances for the creation of quasi-one-dimensional ultracold gases of alkali–alkaline-earth dimers," *Physical Review A*, vol. 112, no. 4, p. 043 313, Oct. 2025.

[98] E. Haller et al., "Realization of an Excited, Strongly Correlated Quantum Gas Phase," *Science*, vol. 325, no. 5945, pp. 1224–1227, Sep. 2009.

[99] P. J. Dagdigian and L. Wharton, "Molecular Beam Electric Deflection and Resonance Spectroscopy of the Heteronuclear Alkali Dimers: 39K7Li, Rb7Li, 39K23Na, Rb23Na, and 133Cs23Na," *The Journal of Chemical Physics*, vol. 57, no. 4, pp. 1487–1496, Aug. 1972.

[100] M. Aymar and O. Dulieu, "Calculation of accurate permanent dipole moments of the lowest Σ+1,3 states of heteronuclear alkali dimers using extended basis sets," *The Journal of Chemical Physics*, vol. 122, no. 20, p. 204 302, May 2005.

[101] G. Igel-Mann, U. Wedig, P. Fuentealba, and H. Stoll, "Ground-state properties of alkali dimers XY (X, Y=Li to Cs)," *The Journal of Chemical Physics*, vol. 84, no. 9, pp. 5007–5012, May 1986.

[102] S. Zhang et al., "Observation of self-bound droplets of ultracold dipolar molecules," *Nature*, vol. 651, no. 8106, pp. 601–606, Mar. 2026.

[103] M. Ciardi, K. R. Pedersen, T. Langen, and T. Pohl, "Self-Bound Superfluid Membranes and Monolayer Crystals of Ultracold Polar Molecules," *Physical Review Letters*, vol. 135, no. 15, p. 153 401, Oct. 2025.

[104] G. Pupillo, A. Griessner, A. Micheli, M. Ortner, D.-W. Wang, and P. Zoller, "Cold Atoms and Molecules in Self-Assembled Dipolar Lattices," *Physical Review Letters*, vol. 100, no. 5, p. 050 402, Feb. 2008.

[105] M. A. Baranov, M. Dalmonte, G. Pupillo, and P. Zoller, "Condensed Matter Theory of Dipolar Quantum Gases," *Chemical Reviews*, vol. 112, no. 9, pp. 5012–5061, Sep. 2012.

[106] T Lahaye, C Menotti, L Santos, M Lewenstein, and T Pfau, "The physics of dipolar bosonic quantum gases," *Reports on Progress in Physics*, vol. 72, no. 12, p. 126 401, Dec. 2009.

[107] N. Bigagli et al., "Observation of Bose–Einstein condensation of dipolar molecules," *Nature*, vol. 631, no. 8020, pp. 289–293, Jul. 2024.

[108] J. J. Hudson, B. E. Sauer, M. R. Tarbutt, and E. A. Hinds, "Measurement of the Electron Electric Dipole Moment Using YbF Molecules," *Physical Review Letters*, vol. 89, no. 2, p. 023 003, Jun. 2002.

[109] A. Micheli, G. K. Brennen, and P. Zoller, "A toolbox for lattice-spin models with polar molecules," *Nature Physics*, vol. 2, no. 5, pp. 341–347, May 2006.

[110] S. L. Cornish, M. R. Tarbutt, and K. R. A. Hazzard, "Quantum computation and quantum simulation with ultracold molecules," *Nature Physics*, vol. 20, no. 5, pp. 730–740, May 2024.

[111] D. DeMille, "Quantum Computation with Trapped Polar Molecules," *Physical Review Letters*, vol. 88, no. 6, p. 067 901, Jan. 2002.

[112] S. F. Yelin, K. Kirby, and R. Côté, "Schemes for robust quantum computation with polar molecules," *Physical Review A*, vol. 74, no. 5, p. 050 301, Nov. 2006.

[113] L. R. B. Picard et al., "Entanglement and iSWAP gate between molecular qubits," *Nature*, vol. 637, no. 8047, pp. 821–826, Jan. 2025.

[114] C. M. Holland, Y. Lu, and L. W. Cheuk, *On-Demand Entanglement of Molecules in a Reconfigurable Optical Tweezer Array*, Oct. 2022. arXiv: 2210.06309 [cond-mat, physics:physics, physics:quant-ph].

[115] Q. Wei, S. Kais, B. Friedrich, and D. Herschbach, "Entanglement of polar symmetric top molecules as candidate qubits," *The Journal of Chemical Physics*, vol. 135, no. 15, p. 154 102, Oct. 2011.

[116] P. Yu, L. W. Cheuk, I. Kozyryev, and J. M. Doyle, "A scalable quantum computing platform using symmetric-top molecules," *New Journal of Physics*, vol. 21, no. 9, p. 093 049, Sep. 2019.

[117] M. L. Wall, K Maeda, and L. D. Carr, "Realizing unconventional quantum magnetism with symmetric top molecules," *New Journal of Physics*, vol. 17, no. 2, p. 025 001, Feb. 2015.

[118] M. L. Wall, K. Maeda, and L. D. Carr, "Simulating quantum magnets with symmetric top molecules," *Annalen der Physik*, vol. 525, no. 10-11, pp. 845–865, Nov. 2013.

[119] I. Kozyryev, Z. Lasner, and J. M. Doyle, "Enhanced Sensitivity to Ultralight Bosonic Dark Matter in the Spectra of the Linear Radical SrOH," *Physical Review A*, vol. 103, no. 4, p. 043 313, Apr. 2021, arXiv:1805.08185 [physics].

[120] L. Anderegg et al., "Quantum control of trapped polyatomic molecules for eedm searches," *Science*, vol. 382, no. 6671, pp. 665–668, 2023. eprint: `https://www.science.org/doi/pdf/10.1126/science.adg8155`.

[121] I. Kozyryev and N. R. Hutzler, "Precision Measurement of Time-Reversal Symmetry Violation with Laser-Cooled Polyatomic Molecules," *Physical Review Letters*, vol. 119, no. 13, p. 133 002, Sep. 2017.

[122] Y. Hao et al., "Nuclear spin-dependent parity-violating effects in light polyatomic molecules," *Physical Review A*, vol. 102, no. 5, p. 052 828, Nov. 2020.

[123] E. B. Norrgard, D. S. Barker, S. Eckel, J. A. Fedchak, N. N. Klimov, and J. Scherschligt, "Nuclear-spin dependent parity violation in optically trapped polyatomic molecules," *Communications Physics*, vol. 2, no. 1, p. 77, Jul. 2019.

[124] N. R. Hutzler, "Polyatomic molecules as quantum sensors for fundamental physics," *Quantum Science and Technology*, vol. 5, no. 4, p. 044 011, Oct. 2020.

[125] S. S. Dhillon et al., "The 2017 terahertz science and technology roadmap," *Journal of Physics D: Applied Physics*, vol. 50, no. 4, p. 043 001, Feb. 2017.

[126] C. Sirtori, "Bridge for the terahertz gap," *Nature*, vol. 417, no. 6885, pp. 132–133, May 2002.

[127] B. Iritani, E. Tiberi, W. Skomorowski, R. Moszynski, M. Borkowski, and T. Zelevinsky, "Accurate Determination of Blackbody Radiation Shifts in a Strontium Molecular Lattice Clock," *Physical Review Letters*, vol. 131, no. 26, p. 263 201, Dec. 2023.

[128] K. H. Leung et al., "Transition Strength Measurements to Guide Magic Wavelength Selection in Optically Trapped Molecules," *Physical Review Letters*, vol. 125, no. 15, p. 153 001, Oct. 2020.

[129] M. McDonald et al., "Photodissociation of ultracold diatomic strontium molecules with quantum state control," *Nature*, vol. 535, no. 7610, pp. 122–126, Jul. 2016.

[130] I. Majewska et al., "Experimental and theoretical investigation of the crossover from the ultracold to the quasiclassical regime of photodissociation," *Physical Review A*, vol. 98, no. 4, p. 043 404, Oct. 2018.

[131] S. S. Kondov et al., "Crossover from the Ultracold to the Quasiclassical Regime in State-Selected Photodissociation," *Physical Review Letters*, vol. 121, no. 14, p. 143 401, Oct. 2018.

[132] S. S. Kondov et al., "Molecular lattice clock with long vibrational coherence," *Nature Physics*, vol. 15, no. 11, pp. 1118–1122, 2019.

[133] P. Fayet, "New interactions and the standard models," *Classical and Quantum Gravity*, vol. 13, no. 11A, A19–A31, 1996.

[134] E. Adelberger, B. Heckel, and A. Nelson, "Tests of the Gravitational Inverse-Square Law," *Annual Review of Nuclear and Particle Science*, vol. 53, no. 1, pp. 77–121, 2003.

[135] E. G. Adelberger, J. H. Gundlach, B. R. Heckel, S Hoedl, and S Schlamminger, "Torsion balance experiments: A low-energy frontier of particle physics," *Progress in Particle and Nuclear Physics*, vol. 62, pp. 102–134, 2009.

[136] S. Knapen, T. Lin, and K. M. Zurek, "Light dark matter: Models and constraints," *Physical Review D*, vol. 96, no. 11, p. 115 021, 2017.

[137] Y. Kamiya, K. Itagaki, M. Tani, G. N. Kim, and S. Komamiya, "Constraints on new gravity-like forces in the nanometer range," *Physical Review Letters*, vol. 114, no. 16, p. 161 101, 2015.

[138] R. D. Newman, E. C. Berg, and P. E. Boynton, "Tests of the gravitational inverse square law at short ranges," *Space Sci. Rev.*, vol. 148, no. 1, pp. 175–190, 2009.

[139] E. Fischbach and C. L. Talmadge, *The search for non-Newtonian gravity*. Springer Science & Business Media, 2012.

[140] H. Desmond, P. G. Ferreira, G. Lavaux, and J. Jasche, "The fifth force in the local cosmic web," *Mon. Not. R. Astron. Soc.*, vol. 483, no. 1, pp. L64–L68, Nov. 2018.

[141] E. Hardy and R. Lasenby, "Stellar cooling bounds on new light particles: Plasma mixing effects," *Journal of High Energy Physics*, vol. 2017, no. 2, p. 33, Feb. 2017.

[142] B. Schwarzschild, "Reanalysis of Old Eötvös Data Suggests 5th Force... To Some," *Phys. Today*, vol. 39, no. 10, pp. 17–20, Oct. 1986.

[143] G. L. Klimchitskaya and V. M. Mostepanenko, "Dark matter axions, non-Newtonian gravity and constraints on them from recent measurements of the Casimir force in the micrometer separation range," *Universe*, vol. 7, no. 9, p. 343, Sep. 2021.

[144] J. K. Hoskins, R. D. Newman, R. Spero, and J. Schultz, "Experimental tests of the gravitational inverse-square law for mass separations from 2 to 105 cm," *Phys. Rev. D*, vol. 32, pp. 3084–3095, 12 1985.

[145] J. G. Lee, E. G. Adelberger, T. S. Cook, S. M. Fleischer, and B. R. Heckel, "New Test of the Gravitational 1 / r 2 Law at Separations down to 52 μ m," *Physical Review Letters*, vol. 124, no. 10, p. 101 101, Mar. 2020.

[146] C. C. Haddock et al., "Search for deviations from the inverse square law of gravity at nm range using a pulsed neutron beam," *Physical Review D*, vol. 97, no. 6, p. 062 002, 2018.

[147] V. V. Nesvizhevsky, G Pignol, and K. V. Protasov, "Neutron scattering and extra-short-range interactions," *Physical Review D*, vol. 77, no. 3, p. 034 020, 2008.

[148] B. Heacock et al., "Pendellösung interferometry probes the neutron charge radius, lattice dynamics, and fifth forces," *Science*, vol. 373, no. 6560, pp. 1239–1243, Sep. 2021.

[149] W. Ubachs, J. Koelemeij, K. Eikema, and E. Salumbides, "Physics beyond the Standard Model from hydrogen spectroscopy," *J. Mol. Spectrosc.*, vol. 320, pp. 1–12, 2016.

[150] M. Germann et al., "Three-body QED test and fifth-force constraint from vibrations and rotations of HD^+," *Phys. Rev. Research*, vol. 3, p. L022028, 2 2021.

[151] M. Borkowski et al., "Weakly bound molecules as sensors of new gravitylike forces," *Scientific Reports*, vol. 9, no. 1, p. 14 807, 2019.

[152] Y. N. Pokotilovski, "Constraints on new interactions from neutron scattering experiments," *Physics of Atomic Nuclei*, vol. 69, no. 6, pp. 924–931, 2006.

[153] U. Mohideen and A. Roy, "Precision measurement of the Casimir force from 0.1 to 0.9 μm," *Phys. Rev. Lett.*, vol. 81, pp. 4549–4552, 21 1998.

[154] K. H. Leung et al., "Terahertz vibrational molecular clock with systematic uncertainty at the 10^{-14} level," *Phys. Rev. X*, vol. 13, p. 011 047, 1 2023.

[155] G. Reinaudi, C. B. Osborn, K. Bega, and T. Zelevinsky, "Dynamically configurable and optimizable Zeeman slower using permanent magnets and servomotors," *Journal of the Optical Society of America B*, vol. 29, no. 4, p. 729, Apr. 2012.

[156] C. B. Osborn, "The Physics of Ultracold Sr2 Molecules: Optical Production and Precision Measurement,"

[157] J. M. Brown and A. Carrington, *Rotational Spectroscopy of Diatomic Molecules*. Cambridge: Cambridge University Press, 2003, ISBN: 9780511814808.

[158] K. H. Leung, "The strontium molecular lattice clock: Vibrational spectroscopy with hertz-level accuracy,"

[159] M. McDonald, B. H. McGuyer, G. Z. Iwata, and T. Zelevinsky, "Thermometry via Light Shifts in Optical Lattices," *Physical Review Letters*, vol. 114, no. 2, p. 023 001, Jan. 2015.

[160] M. McDonald et al., "Control of Ultracold Photodissociation with Magnetic Fields," *Physical Review Letters*, vol. 120, no. 3, p. 033 201, Jan. 2018.

[161] S. S. Kondov et al., "Molecular lattice clock with long vibrational coherence," *Nature Physics*, vol. 15, no. 11, pp. 1118–1122, Nov. 2019.

[162] K. H. Leung, E. Tiberi, B. Iritani, I. Majewska, R. Moszynski, and T. Zelevinsky, "Ultracold $^{88}\rm{Sr}_2$ molecules in the absolute ground state," *arXiv:2108.05996 [physics, physics:quant-ph]*, Aug. 2021. arXiv: 2108.05996 [physics, physics:quant-ph].

[163] K. H. Leung et al., "Transition strength measurements to guide magic wavelength selection in optically trapped molecules," *Phys. Rev. Lett.*, vol. 125, p. 153 001, 15 2020.

[164] K. H. Leung, "The strontium molecular lattice clock: Vibrational spectroscopy with hertz-level accuracy," Ph.D. dissertation, Columbia University, 2023.

[165] K. Bergmann, H. Theuer, and B. W. Shore, "Coherent population transfer among quantum states of atoms and molecules," *Reviews of Modern Physics*, vol. 70, no. 3, pp. 1003–1025, 1998.

[166] K. Aikawa et al., "Coherent Transfer of Photoassociated Molecules into the Rovibrational Ground State," *Physical Review Letters*, vol. 105, no. 20, p. 203 001, Nov. 2010.

[167] T. Takekoshi et al., "Ultracold Dense Samples of Dipolar RbCs Molecules in the Rovibrational and Hyperfine Ground State," *Physical Review Letters*, vol. 113, no. 20, p. 205 301, Nov. 2014.

[168] P. K. Molony et al., "Creation of Ultracold Rb 87 Cs 133 Molecules in the Rovibrational Ground State," *Physical Review Letters*, vol. 113, no. 25, p. 255 301, Dec. 2014.

[169] J. W. Park, S. A. Will, and M. W. Zwierlein, "Ultracold Dipolar Gas of Fermionic Na 23 K 40 Molecules in Their Absolute Ground State," *Physical Review Letters*, vol. 114, no. 20, p. 205 302, May 2015.

[170] M. Guo et al., "Creation of an Ultracold Gas of Ground-State Dipolar Na 23 Rb 87 Molecules," *Physical Review Letters*, vol. 116, no. 20, p. 205 303, May 2016.

[171] T. M. Rvachov et al., "Long-Lived Ultracold Molecules with Electric and Magnetic Dipole Moments," *Physical Review Letters*, vol. 119, no. 14, p. 143 001, Oct. 2017.

[172] F. Seeßelberg et al., "Modeling the adiabatic creation of ultracold polar 23 Na 40 K molecules," *Physical Review A*, vol. 97, no. 1, p. 013 405, Jan. 2018.

[173] L. Liu et al., "Observation of Interference between Resonant and Detuned stirap in the Adiabatic Creation of Na 23 K 40 Molecules," *Physical Review Letters*, vol. 122, no. 25, p. 253 201, Jun. 2019.

[174] J. G. Danzl et al., "Quantum Gas of Deeply Bound Ground State Molecules," *Science*, vol. 321, no. 5892, pp. 1062–1066, Aug. 2008.

[175] K.-K. Ni et al., "A High Phase-Space-Density Gas of Polar Molecules," *Science*, vol. 322, no. 5899, pp. 231–235, Oct. 2008.

[176] J. G. Danzl et al., "An ultracold high-density sample of rovibronic ground-state molecules in an optical lattice," *Nature Physics*, vol. 6, no. 4, pp. 265–270, Apr. 2010.

[177] Z. Idziaszek and P. S. Julienne, "Universal Rate Constants for Reactive Collisions of Ultracold Molecules," *Physical Review Letters*, vol. 104, no. 11, p. 113 202, Mar. 2010.

[178] J Reichert, R Holzwarth, T. Udem, and T. W. Hksch, "Measuring the frequency of light with mode-locked lasers ',"

[179] S. A. Diddams et al., "Direct Link between Microwave and Optical Frequencies with a 300 THz Femtosecond Laser Comb," *Physical Review Letters*, vol. 84, no. 22, pp. 5102–5105, May 2000.

[180] D. J. Jones et al., "Carrier-Envelope Phase Control of Femtosecond Mode-Locked Lasers and Direct Optical Frequency Synthesis," *Science*, vol. 288, no. 5466, pp. 635–639, Apr. 2000.

[181] T. Udem, R Holzwarth, and T. W. Hänsch, "Optical frequency metrology," 2002.

[182] T. M. Fortier, D. J. Jones, and S. T. Cundiff, "Phase stabilization of an octave-spanning Ti:sapphire laser," *Optics Letters*, vol. 28, no. 22, p. 2198, Nov. 2003.

[183] R. W. Drever et al., "Laser phase and frequency stabilization using an optical resonator," *Applied Physics B*, vol. 31, pp. 97–105, 1983.

[184] R. C. Brown et al., "Hyperpolarizability and Operational Magic Wavelength in an Optical Lattice Clock," *Physical Review Letters*, vol. 119, no. 25, p. 253 001, Dec. 2017.

[185] D. Allan, "Statistics of atomic frequency standards," *Proceedings of the IEEE*, vol. 54, no. 2, pp. 221–230, Feb. 1966.

[186] F. Riehle, *Frequency Standards: Basics and Applications*. Weinheim: Wiley-VCH, 2004.

[187] W. J. Riley, "Handbook of frequency stability analysis," National Institute of Standards and Technology, Boulder, NIST Special Publication 1065, 2008.

[188] R. Le Targat et al., "Experimental realization of an optical second with strontium lattice clocks," *Nature Communications*, vol. 4, no. 1, p. 2109, 2013.

[189] S. Falke et al., "A strontium lattice clock with 3×10^{-17} inaccuracy and its frequency," *New Journal of Physics*, vol. 16, no. 7, p. 073 023, 2014.

[190] T. Nicholson et al., "Systematic evaluation of an atomic clock at 2×10^{-18} total uncertainty," *Nature Communications*, vol. 6, no. 1, p. 6896, 2015.

[191] S. B. Koller et al., "Transportable optical lattice clock with 7×10^{-17} uncertainty," *Phys. Rev. Lett.*, vol. 118, p. 073 601, 7 2017.

[192] W. F. McGrew et al., "Atomic clock performance enabling geodesy below the centimetre level," *Nature*, vol. 564, no. 7734, pp. 87–90, 2018.

[193] T. Bothwell et al., "JILA SrI optical lattice clock with uncertainty of 2×10^{-18}," *Metrologia*, vol. 56, no. 6, p. 065 004, 2019.

[194] Y. Hisai et al., "Improved frequency ratio measurement with ^{87}Sr and ^{171}Yb optical lattice clocks at NMIJ," *Metrologia*, vol. 58, no. 1, p. 015 008, 2021.

[195] N. Ohmae et al., "Transportable Strontium Optical Lattice Clocks Operated Outside Laboratory at the Level of 10^{-18} Uncertainty," *Advanced Quantum Technologies*, vol. 4, no. 8, p. 2 100 015, 2021.

[196] I. Ushijima, M. Takamoto, M. Das, T. Ohkubo, and H. Katori, "Cryogenic optical lattice clocks," *Nature Photonics*, vol. 9, no. 3, pp. 185–189, 2015.

[197] P. Ablewski, M. Bober, and M. Zawada, "Emissivities of vacuum compatible materials: Towards minimising blackbody radiation shift uncertainty in optical atomic clocks at room temperatures," *Metrologia*, vol. 57, no. 3, p. 035 004, 2020.

[198] V. I. Yudin et al., "Combined atomic clock with blackbody-radiation-shift-induced instability below 10^{-19} under natural environment conditions," *New Journal of Physics*, vol. 23, no. 2, p. 023 032, 2021.

[199] M. S. Safronova, private communication, 2023.

[200] K. D. Bonin and V. V. Kresin, *Electric-dipole polarizabilities of atoms, molecules, and clusters*. World Scientific, 1997.

[201] L. Landau and E. Lifshitz, *Statistical Physics*. Pergamon Press, 1958.

[202] K. D. Nanda and A. I. Krylov, "Static polarizabilities for excited states within the spin-conserving and spin-flipping equation-of-motion coupled-cluster singles and doubles formalism: Theory, implementation, and benchmarks," *The Journal of Chemical Physics*, vol. 145, no. 20, p. 204 116, Nov. 2016.

[203] E. Epifanovsky et al., "Software for the frontiers of quantum chemistry: An overview of developments in the Q-Chem 5 package," *The Journal of Chemical Physics*, vol. 155, no. 8, p. 084 801, Aug. 2021.

[204] I. S. Lim, H. Stoll, and P. Schwerdtfeger, "Relativistic small-core energy-consistent pseudopotentials for the alkaline-earth elements from Ca to Ra," *The Journal of Chemical Physics*, vol. 124, no. 3, p. 034 107, Jan. 2006.

[205] A. Dalgarno, A. L. Ford, and J. C. Browne, "Direct Sum-of-States Calculations of the Frequency-Dependent Polarizability of H_2," *Physical Review Letters*, vol. 27, pp. 1033–1036, 16 Oct. 1971.

[206] T. G. A. Heijmen, R. Moszynski, P. E. S. Wormer, and A. van der Avoird, "Symmetry-adapted perturbation theory applied to interaction-induced properties of collisional complexes," *Molecular Physics*, vol. 89, no. 1, pp. 81–110, 1996.

[207] D. T. Colbert and W. H. Miller, "A novel discrete variable representation for quantum mechanical reactive scattering via the S-matrix Kohn method," *J. Chem. Phys.*, vol. 96, no. February, p. 1982, 1992.

[208] E. Tiesinga, C. J. Williams, and P. S. Julienne, "Photoassociative spectroscopy of highly excited vibrational levels of alkali-metal dimers: Green-function approach for eigenvalue solvers," *Phys. Rev. A*, vol. 57, no. 6, pp. 4257–4267, 1998.

[209] A Stein, H Knöckel, and E Tiemann, "$^1S+^1S$ asymptote of Sr_2 studied by Fourier-transform spectroscopy," *Eur. Phys. J. D*, vol. 57, pp. 171–177, 2010.

[210] E. Tiesinga, P. J. Mohr, D. B. Newell, and B. N. Taylor, "Codata recommended values of the fundamental physical constants: 2018," *Rev. Mod. Phys.*, vol. 93, p. 025 010, 2 2021.

[211] B. H. McGuyer et al., "High-precision spectroscopy of ultracold molecules in an optical lattice," *New J. Phys*, vol. 17, p. 055 004, 2015.

[212] M. S. Safronova, S. G. Porsev, U. I. Safronova, M. G. Kozlov, and C. W. Clark, "Blackbody-radiation shift in the Sr optical atomic clock," *Physical Review A*, vol. 87, p. 012 509, 1 Jan. 2013.

[213] R. J. Le Roy, N. S. Dattani, J. A. Coxon, A. J. Ross, P. Crozet, and C. Linton, "Accurate analytic potentials for $Li_2(X\ ^1\Sigma_g)$ and $Li_2(A\ X\ ^1\Sigma_u^+)$ from 2 to 90 Å, and the radiative lifetime of Li(2p)," *The Journal of Chemical Physics*, vol. 131, no. 20, p. 204 309, 2009.

[214] P. A. Fraser, "A method of determining the electronic transition moment for diatomic molecules," *Canadian Journal of Physics*, vol. 32, no. 8, pp. 515–521, 1954.

[215] R. J. Le Roy and R. B. Bernstein, "Dissociation Energy and Long-Range Potential of Diatomic Molecules from Vibrational Spacings of Higher Levels," *The Journal of Chemical Physics*, vol. 52, no. 8, p. 3869, 1970.

[216] R. J. Le Roy, *Energy Levels of a Diatomic near Dissociation*. The Chemical Society, London, 1973, pp. 113–171.

[217] E Clementi, D. L. Raimondi, and W. P. Reinhardt, "Atomic Screening Constants from SCF Functions. II. Atoms with 37 to 86 Electrons," *J. Chem. Phys.*, vol. 471, no. 4, pp. 1300–2686, 1967.

[218] K. M. Jones, E. Tiesinga, P. D. Lett, and P. S. Julienne, "Ultracold photoassociation spectroscopy: Long-range molecules and atomic scattering," *Reviews of Modern Physics*, vol. 78, no. 2, pp. 483–535, 2006.

[219] B. N. Taylor and C. E. Kuyatt, *NIST Technical Note 1297. Guidelines for evaluating and expressing the uncertainty of NIST measurement results*. US Department of Commerce, Technology Administration, National Institute of Standards and Technology, 1994.

[220] J. W. Farley and W. H. Wing, "Accurate calculation of dynamic stark shifts and depopulation rates of Rydberg energy levels induced by blackbody radiation. Hydrogen, helium, and alkali-metal atoms," *Phys. Rev. A*, vol. 23, pp. 2397–2424, 5 1981.

[221] S. G. Porsev and A. Derevianko, "Multipolar theory of blackbody radiation shift of atomic energy levels and its implications for optical lattice clocks," *Phys. Rev. A*, vol. 74, p. 020 502, 2 2006.

[222] T. Middelmann, S. Falke, C. Lisdat, and U. Sterr, "High accuracy correction of blackbody radiation shift in an optical lattice clock," *Phys. Rev. Lett.*, vol. 109, p. 263 004, 26 2012.

[223] J. Mitroy, M. S. Safronova, and C. W. Clark, "Theory and applications of atomic and ionic polarizabilities," *Journal of Physics B: Atomic, Molecular and Optical Physics*, vol. 43, no. 20, p. 202 001, 2010.

[224] C. Lisdat, S. Dörscher, I. Nosske, and U. Sterr, "Blackbody radiation shift in strontium lattice clocks revisited," *Phys. Rev. Res.*, vol. 3, p. L042036, 4 2021.

[225] T. Bothwell, "A Wannier-Stark Optical Lattice Clock With Extended Coherence Times,"

[226] J. L. Siegel et al., "Excited-Band Coherent Delocalization for Improved Optical Lattice Clock Performance," *Physical Review Letters*, vol. 132, no. 13, p. 133 201, Mar. 2024.

[227] J. A. DeYoung, F. Vannicola, and A. D. McKinley, "A comparison of the highest precision commonly available time transfer methods: TWSTT and GPS CV," in *28th Annual Precise Time and Time Interval (PTTI) Applications and Planning Meetings*, vol. 28, Reston, Virginia, USA, 1997, pp. 349–356.

[228] J.-D. Deschênes and J. Genest, "Chirped pulse heterodyne for optimal beat note detection between a frequency comb and a continuous wave laser," *Optics Express*, vol. 23, no. 7, p. 9295, Apr. 2015.

[229] S. Jackson and A. C. Vutha, "Magic polarization for cancellation of light shifts in two-photon optical clocks," *Physical Review A*, vol. 99, no. 6, p. 063 422, Jun. 2019.

[230] F. Le Kien, P. Schneeweiss, and A. Rauschenbeutel, "Dynamical polarizability of atoms in arbitrary light fields: General theory and application to cesium," *The European Physical Journal D*, vol. 67, no. 5, p. 92, May 2013.

[231] B. Chomet et al., "Highly coherent phase-lock of an 8.1 μ m quantum cascade laser to a turn-key mid-IR frequency comb," *Applied Physics Letters*, vol. 122, no. 23, p. 231 102, Jun. 2023.

[232] E. Tiberi, M. Borkowski, B. Iritani, R. Moszynski, and T. Zelevinsky, *Searching for New Fundamental Interactions via Isotopic Shifts in Molecular Lattice Clocks*, Mar. 2024. arXiv: 2403.07097 [gr-qc, physics:hep-ph, physics:physics].

[233] A. S. Jensen, K. Riisager, D. V. Fedorov, and E. Garrido, "Structure and reactions of quantum halos," *Reviews of Modern Physics*, vol. 76, no. 1, pp. 215–261, Feb. 2004.

[234] P. G. Mickelson et al., "Spectroscopic Determination of the s -Wave Scattering Lengths of Sr 86 and Sr 88," *Physical Review Letters*, vol. 95, no. 22, p. 223 002, Nov. 2005.

[235] J. A. Aman, J. C. Hill, R. Ding, K. R. A. Hazzard, T. C. Killian, and W. Y. Kon, "Photoassociative spectroscopy of a halo molecule in Sr 86," *Physical Review A*, vol. 98, no. 5, p. 053 441, Nov. 2018.

[236] H. B. G. Casimir and D. Polder, "The Influence of Retardation on the London-van der Waals Forces," *Physical Review*, vol. 73, no. 4, pp. 360–372, Feb. 1948.

[237] M. Przybytek, B. Jeziorski, W. Cencek, J. Komasa, J. B. Mehl, and K. Szalewicz, "Onset of Casimir-Polder retardation in a long-range molecular quantum state," *Phys. Rev. Lett.*, vol. 108, p. 183 201, 2012.

[238] E. Braaten and H.-W. Hammer, "Efimov physics in cold atoms," *Annals of Physics*, vol. 322, no. 1, pp. 120–163, Jan. 2007.

[239] P. Naidon and S. Endo, "Efimov physics: A review," *Reports on Progress in Physics*, vol. 80, no. 5, p. 056 001, May 2017.

[240] D. M. Bauer, M. Lettner, C. Vo, G. Rempe, and S. Dürr, "Control of a magnetic Feshbach resonance with laser light," *Nature Physics*, vol. 5, no. 5, pp. 339–342, May 2009.

[241] L. W. Clark, L.-C. Ha, C.-Y. Xu, and C. Chin, "Quantum Dynamics with Spatiotemporal Control of Interactions in a Stable Bose-Einstein Condensate," *Physical Review Letters*, vol. 115, no. 15, p. 155 301, Oct. 2015.

[242] E. Pachomow, V. P. Dahlke, E. Tiemann, F. Riehle, and U. Sterr, "Ground-state properties of Ca 2 from narrow-line two-color photoassociation," *Physical Review A*, vol. 95, no. 4, p. 043 422, Apr. 2017.

[243] T. Köhler, K. Góral, and P. S. Julienne, "Production of cold molecules via magnetically tunable Feshbach resonances," *Reviews of Modern Physics*, vol. 78, no. 4, pp. 1311–1361, Dec. 2006.

[244] W. Schöllkopf and J. P. Toennies, "Nondestructive Mass Selection of Small van der Waals Clusters," *Science*, vol. 266, no. 5189, pp. 1345–1348, Nov. 1994.

[245] F. Luo, G. C. McBane, G. Kim, C. F. Giese, and W. R. Gentry, "The weakest bond: Experimental observation of helium dimer," *The Journal of Chemical Physics*, vol. 98, no. 4, pp. 3564–3567, Feb. 1993.

[246] G. F. Gribakin and V. V. Flambaum, "Calculation of the scattering length in atomic collisions using the semiclassical approximation," *Physical Review A*, vol. 48, no. 1, pp. 546–553, Jul. 1993.

[247] S. Stellmer, B. Pasquiou, R. Grimm, and F. Schreck, "Creation of Ultracold Sr 2 Molecules in the Electronic Ground State," *Physical Review Letters*, vol. 109, no. 11, p. 115 302, Sep. 2012.

[248] S. Stellmer, F. Schreck, and T. C. Killian, "Degenerate quantum gases of strontium," in vol. 2, May 2014, pp. 1–80. arXiv: 1307.0601 [cond-mat].

[249] H. Miyake, N. C. Pisenti, P. K. Elgee, A. Sitaram, and G. K. Campbell, "Isotope-shift spectroscopy of the S 0 1 → P 1 3 and S 0 1 → P 0 3 transitions in strontium," *Physical Review Research*, vol. 1, no. 3, p. 033 113, Nov. 2019.

[250] M. McDonald, *High Precision Optical Spectroscopy and Quantum State Selected Photodissociation of Ultracold 88Sr2 Molecules in an Optical Lattice* (Springer Theses). Cham: Springer International Publishing, 2018, ISBN: 978-3-319-68734-6 978-3-319-68735-3.

[251] I. Majewska, "Theoretical description of ultracold strontium molecules in an optical lattice: Control of photodissociation and interpretation of molecular clock experiments,"

[252] B. Iritani, J. Huang, W. Xu, G. Sim, R. Moszynski, and T. Zelevinsky, *Creation and precise spectroscopy of ^{86}Sr$_2$ halo molecules*, Jan. 2026. arXiv: 2601.06319 [physics].

[253] M. Born and R. Oppenheimer, "Zur Quantentheorie der Molekeln," *Annalen der Physik*, vol. 389, no. 20, pp. 457–484, Jan. 1927.

[254] T. Helgaker, P. Jørgensen, and J. Olsen, *Molecular Electronic-Structure Theory*. Chichester: John Wiley & Sons, 2000, ISBN: 0-471-96755-6.

[255] J. C. Slater, "The Theory of Complex Spectra," *Physical Review*, vol. 34, no. 10, pp. 1293–1322, Nov. 1929.

[256] J. C. Slater, "Note on Hartree's Method," *Physical Review*, vol. 35, no. 2, pp. 210–211, Jan. 1930.

[257] G. D. Purvis and R. J. Bartlett, "A full coupled-cluster singles and doubles model: The inclusion of disconnected triples," *The Journal of Chemical Physics*, vol. 76, no. 4, pp. 1910–1918, Feb. 1982.

[258] K. Raghavachari, G. W. Trucks, J. A. Pople, and M. Head-Gordon, "A fifth-order perturbation comparison of electron correlation theories," *Chemical Physics Letters*, vol. 157, no. 6, pp. 479–483, May 1989.

[259] B. Jeziorski and R. Moszynski, "Explicitly connected expansion for the average value of an observable in the coupled-cluster theory," *International Journal of Quantum Chemistry*, vol. 48, no. 3, pp. 161–183, Nov. 1993.

[260] K. Raghavachari, G. W. Trucks, J. A. Pople, and M. Head-Gordon, "A fifth-order perturbation comparison of electron correlation theories," *Chemical Physics Letters*, vol. 157, no. 6, pp. 479–483, May 1989.

[261] T. H. Dunning, "Gaussian basis sets for use in correlated molecular calculations. I. The atoms boron through neon and hydrogen," *Journal of Chemical Physics*, vol. 90, p. 1007, 1989.

[262] R. A. Kendall, T. H. Dunning, and R. J. Harrison, "Electron affinities of the first-row atoms revisited. Systematic basis sets and wave functions," *Journal of Chemical Physics*, vol. 96, p. 6796, 1992.

[263] J. C. Slater, "Atomic Shielding Constants," *Physical Review*, vol. 36, no. 1, pp. 57–64, Jul. 1930.

[264] J. C. Slater, "Analytic Atomic Wave Functions," *Physical Review*, vol. 42, no. 1, pp. 33–43, Oct. 1932.

[265] M. W. Schmidt and K. Ruedenberg, "Effective convergence to complete orbital bases and to the atomic Hartree-Fock limit through systematic sequences of Gaussian primitives," *Journal of Chemical Physics*, vol. 71, p. 3951, 1979.

[266] K. Raghavachari, G. W. Trucks, J. A. Pople, and M. Head-Gordon, "A fifth-order perturbation comparison of electron correlation theories," *Chemical Physics Letters*, vol. 157, p. 479, 1989.

[267] T. Helgaker, W. Klopper, H. Koch, and J. Noga, "Basis-set convergence of correlated calculations on water," *Journal of Chemical Physics*, vol. 106, p. 9639, 1997.

[268] A. Halkier, T. Helgaker, P. Jørgensen, W. Klopper, and J. Olsen, "Basis-set convergence of the energy in molecular Hartree–Fock calculations," *Chemical Physics Letters*, vol. 302, no. 5-6, pp. 437–446, Mar. 1999.

[269] M. Douglas and N. M. Kroll, "Quantum electrodynamical corrections to the fine structure of helium," *Annals of Physics*, vol. 82, p. 89, 1974.

[270] B. A. Hess, "Relativistic electronic-structure calculations employing a two-component no-pair formalism with external-field projection operators," *Physical Review A*, vol. 33, p. 3742, 1986.

[271] P. Czachorowski, M. Przybytek, M. Lesiuk, M. Puchalski, and B. Jeziorski, "Second virial coefficients for He 4 and He 3 from an accurate relativistic interaction potential," *Physical Review A*, vol. 102, no. 4, p. 042 810, Oct. 2020.

[272] K. T. Tang and J. P. Toennies, "An improved simple model for the van der Waals potential based on universal damping functions for the dispersion coefficients," *Journal of Chemical Physics*, vol. 80, p. 3726, 1984.

[273] L. M. C. Janssen, A. van der Avoird, and G. C. Groenenboom, "Reactive scattering of ultracold NH radicals," *European Physical Journal D*, vol. 65, p. 177, 2013.

[274] M. Iliáš and T. Saue, "An infinite-order two-component relativistic Hamiltonian by a simple one-step transformation," *Journal of Chemical Physics*, vol. 126, p. 064 102, 2007.

[275] T. Saue et al., "The DIRAC code for relativistic molecular calculations," *The Journal of Chemical Physics*, vol. 152, no. 20, p. 204 104, May 2020.

[276] R. Moszynski, P. S. Żuchowski, and B. Jeziorski, "Time-Independent Coupled-Cluster Theory of the Polarization Propagator," *Collection of Czechoslovak Chemical Communications*, vol. 70, no. 8, pp. 1109–1132, 2005.

[277] M. Puchalski, D. Kędziera, and K. Pachucki, "Ionization potential for excited S states of the lithium atom," *Physical Review A*, vol. 82, no. 6, p. 062 509, Dec. 2010.

[278] H. Araki, "Quantum-Electrodynamical Corrections to Energy-Levels of Helium," *Progress of Theoretical Physics*, vol. 17, no. 5, pp. 619–642, May 1957.

[279] J. Sucher, "Energy Levels of the Two-Electron Atom to Order α 3 ry; Ionization Energy of Helium," *Physical Review*, vol. 109, no. 3, pp. 1010–1011, Feb. 1958.

[280] J. G. Balcerzak, M. Lesiuk, and R. Moszynski, "Calculation of Araki-Sucher correction for many-electron systems," *Physical Review A*, vol. 96, no. 5, p. 052 510, Nov. 2017.

[281] K. T. Tang and J. P. Toennies, "An improved simple model for the van der Waals potential based on universal damping functions for the dispersion coefficients," *The Journal of Chemical Physics*, vol. 80, no. 8, pp. 3726–3741, Apr. 1984.

[282] P. Czachorowski, M. Przybytek, M. Lesiuk, M. Puchalski, and B. Jeziorski, "Second virial coefficients for He 4 and He 3 from an accurate relativistic interaction potential," *Physical Review A*, vol. 102, no. 4, p. 042 810, Oct. 2020.

[283] H. Knöckel, S. Rühmann, and E. Tiemann, "The \X^{1}\Sigma ^{+}_\{g}\X1Σg+ ground state of Mg2 studied by Fourier-transform spectroscopy," *The Journal of Chemical Physics*, vol. 138, no. 9, p. 094 303, Mar. 2013.

[284] B. Numerov, "A method of extrapolation of perturbations," *Monthly Notices of the Royal Astronomical Society*, vol. 84, p. 592, 1924.

[285] D. T. Colbert and W. H. Miller, "A novel discrete variable representation for quantum mechanical reactive scattering via the *S* -matrix Kohn method," *The Journal of Chemical Physics*, vol. 96, no. 3, pp. 1982–1991, Feb. 1992.

[286] W. Huie, "Refinement of the strontium molecular potential by numerical computation of bound states,"

[287] J. Barzilai and J. M. Borwein, "Two-point step size gradient methods," *IMA Journal of Numerical Analysis*, vol. 8, pp. 141–148, 1988.

[288] P. Zhang and A. Dalgarno, "Long-range interactions of ytterbium atoms," *Molecular Physics*, vol. 106, no. 12, pp. 1525–1529, 2008.

[289] J. O. Hirschfelder, Ed., *Intermolecular Forces* (Advances in Chemical Physics). New York: Interscience Publishers, 1967, vol. 12.

[290] M. Marinescu, J. F. Babb, and A. Dalgarno, "Long-range potentials, including retardation, for the interaction of two alkali-metal atoms," *Physical Review A*, vol. 50, no. 4, pp. 3096–3104, Oct. 1994.

[291] R. Moszynski, G. Łach, M. Jaszuński, and B. Bussery-Honvault, "Long-range relativistic interactions in the Cowan-Griffin approximation and their QED retardation: Application to helium, calcium, and cadmium dimers," *Physical Review A - Atomic, Molecular, and Optical Physics*, vol. 68, no. 5, p. 11, 2003.

[292] K. M Jones, P. S Julienne, P. D Lett, W. D Phillips, E Tiesinga, and C. J Williams, "Measurement of the atomic Na(3 P) lifetime and of retardation in the interaction between two atoms bound in a molecule," *Europhysics Letters (EPL)*, vol. 35, no. 2, pp. 85–90, Jul. 1996.

[293] M. Przybytek, B. Jeziorski, W. Cencek, J. Komasa, J. B. Mehl, and K. Szalewicz, "Onset of Casimir-Polder Retardation in a Long-Range Molecular Quantum State," *Physical Review Letters*, vol. 108, no. 18, p. 183 201, May 2012.

[294] M. Przybytek, W. Cencek, J. Komasa, G. Łach, B. Jeziorski, and K. Szalewicz, "Relativistic and Quantum Electrodynamics Effects in the Helium Pair Potential," *Physical Review Letters*, vol. 104, no. 18, p. 183 003, May 2010.

[295] M. J. Jamieson, G. W. F. Drake, and A. Dalgarno, "Retarded dipole-dipole dispersion interaction potential for helium," *Physical Review A*, vol. 51, no. 4, pp. 3358–3361, Apr. 1995.